

ABSTRACT

Title of dissertation: MORPHOLOGY, STAR FORMATION,
AND KINEMATICS OF NUCLEAR RINGS

Lisa M. Mazzuca, Doctor of Philosophy, 2006

Dissertation directed by: Professor Sylvain Veilleux
Department of Astronomy

This thesis presents a detailed optical study with the goal of better understanding the elusive physical nature of nuclear rings. We first image the central kilo-parsec region of a large sample of spiral galaxies known for intense star formation via the $H\alpha\lambda 6563$ line and the optical broad bands B and I . The distribution of massive young stars in the nuclear and circumnuclear environments verifies that nuclear rings occur primarily in spiral types Sa-Sbc. Late-type galaxies have a patchy and more diffuse circumnuclear appearance in $H\alpha$. We identify three previously unknown nuclear rings, and confirm that nuclear rings are preferentially found in barred galaxies. From the parent sample, we identify 22 nuclear rings and analyze the H II regions that comprise them. Comparing the $H\alpha$ equivalent widths of these regions with population synthesis models, we derive the ages throughout each nuclear ring, and find that the stellar content within the rings is consistently very young, with ages ranging from 1 Myr to 10 Myrs. Approximately half of the rings contain azimuthal age gradients that encompass at least 25% of the ring, although there is no apparent relationship between the presence or absence of age gradients

and the morphology of the rings or their host galaxies. Two-thirds of the galaxies containing a nuclear ring and a bar show a link between the youngest H II region(s) and the location along the ring where the bar dust lanes merge. We show that regions of enhanced star formation, as seen in nuclear rings, correspond to regions with (1) the strongest H α emission, (2) high luminosities of order 10^{40}erg s^{-1} - 10^{42}erg s^{-1} , (3) low residual velocities of order 10 km s^{-1} , and (4) low velocity dispersions ranging from 20 km s^{-1} - 50 km s^{-1} . Thus, within the rings, the relatively cool and calm gas allows star formation to trigger. The lack of strong non-circular motions in the rings, coupled with a direct relationship between the position angles and ellipticities of the rings and those of their host galaxies, indicate the rings are in the same plane as the disk and are circular. Along the exterior edge of the rings, we find a correlation between the largest velocity deviations from circular motion and the location of the bar minor axis, where the dominant family of stellar orbits transitions from the x_1 family, which supports the bar, to the x_2 family, which is associated with the location of nuclear rings. Lastly, for the first time we apply two-dimensional line ratio diagnostics to separate the physical environments of a nuclear ring and an AGN. Diagnostic diagrams of NGC 7742 indicate very low gas densities in the nuclear ring, and show the transition from star formation in the ring to excitation by high-velocity shocks or by a central AGN towards the center. Comparison to starburst population models reveals that the H II regions comprising the ring are of roughly solar metallicity.

MORPHOLOGY, STAR FORMATION, AND KINEMATICS
OF NUCLEAR RINGS

by

Lisa M. Mazzuca

Dissertation submitted to the Faculty of the Graduate School of the
University of Maryland, College Park in partial fulfillment
of the requirements for the degree of
Doctor of Philosophy
2006

Advisory Committee:
Professor Sylvain Veilleux, Advisor
Professor Stacy McGaugh
Professor Stuart Vogel
Professor Douglas C. Hamilton
Dr. Michael Regan

© Copyright by
Lisa M. Mazzuca
2006

PREFACE

The work described in this dissertation was carried out between September 2001 and June 2006. Analysis is based on two large data sets, one imaging and one spectroscopic, with much of the results either published or in the submission process to various journals. This dissertation combines these works into a coherent detailed study on the physical environment of the phenomenon of *nuclear rings*.

Chapter 2 is based on early work done in collaboration with Dr. Johan Knapen, as the original data is from his (and others) observations. This chapter is published in *Astronomy & Astrophysics* as “Massive Star Formation in the Central Regions of Spiral Galaxies” (Knapen et al. 2006). Although second author on this paper, my role was significant in the data reduction and analysis sections. This introductory paper builds the foundation and adds context to the thesis, which is why it is included. Chapter 3 is submitted to the *Astrophysical Journal* as “A Connection between Star Formation in Nuclear Rings and their Host Galaxies” (Mazzuca et al. 2006a). Chapter 5 is a result of collaboration with Dr. Marc Sarzi, as it was necessary to combine our mutually exclusive spectral data sets to perform a complete line-ratio analysis for one galaxy in the sample. This chapter is being submitted as a letter to the *Astrophysical Journal* as “The Physical Conditions of the Ionized Gas in the Central KiloParsec of NGC 7742 ” (Mazzuca et al. 2006b).

ACKNOWLEDGMENTS

This thesis has taken seven long years during which many things have happened in my life that now serve as landmarks. It's been quite a journey academically, with highs and lows, that have strengthened me much like all challenges that I decide to take on in life. This one was particularly complicated as I've not only been a graduate student, but also a full time NASA employee throughout the entire process. But without their support and belief in me, this degree would never have come to fruition. So I first want to thank the folks at Goddard Space Flight Center, especially the Hubble Space Telescope Program, who allowed me to work on my thesis, who took on extra duties when I was not there, who listened to me when I was frustrated, and who saw this opportunity as an investment versus a hinderance.

I am also grateful to my advisors, Dr. Sylvain Veilleux (UMD) and Dr. Johan Knapen (University of Hertfordshire, England), who guided me along the way. I can't say I was a typical graduate student by any means, so I am appreciative that they were flexible enough to allow me to collaborate with other scientists at NASA, Space Telescope Science Institute, and the University of Hertfordshire. The ties I've formed with so many scientists at this early stage will no doubt be invaluable in the future as I transition from engineer to astronomer.

I want to also call out Dr. Rob Swaters, who I consider to be my third advisor. Although he had no idea what he was getting himself into, he became a continual

source of support, both scientifically and emotionally, during the second half of my thesis. His responsiveness, in-depth replies to my questions, and general support are key factors on which I base the completion of this thesis.

Lastly, I must thank my family who are always my biggest cheerleaders. My driven personality is a direct result of their belief in me. I'm sure they are as proud of me for my accomplishments as I am of them for their unyielding support and love.

TABLE OF CONTENTS

List of Tables	vii
List of Figures	ix
1 Introduction	1
1.1 Spiral Galaxies	1
1.2 Barred Spiral Galaxies	2
1.3 Nuclear Rings	5
1.3.1 Photometry	6
1.3.2 Kinematics	8
1.4 Nuclear Rings as Starbursts	9
1.5 Nuclear Ring Models & Theories	12
1.6 Outline of Thesis	16
2 Morphology of Massive Star Formation in the Central Regions of Spiral Galaxies	21
2.1 Overview	21
2.2 Sample selection and parameters	23
2.3 Observations and data reduction	27
2.4 H α morphology: Methodology and limitations	29
2.4.1 Nuclear H α emission	29
2.4.2 Circumnuclear H α morphology	38
2.5 H α morphology and host galaxy parameters	39
2.5.1 Overall results	39
2.5.2 Morphological type of the host galaxy	41
2.5.3 Starburst and AGN activity	45
2.5.4 Nuclear rings and their dynamical origin	48
2.6 Conclusions	51
3 A Connection between Star Formation in Nuclear Rings and their Host Galaxies	53
3.1 Overview	53
3.2 Observations and Data Reduction	56
3.3 Ring Morphology	58
3.4 Equivalent Widths of HII Regions in Nuclear Rings	62
3.4.1 Identification of HII Regions	62
3.4.2 Equivalent Widths	68
3.5 Age Dating	74
3.6 Discussion	76
3.6.1 Age Distribution	76
3.6.2 Inflow and Star Formation Rates	84
3.6.3 Nuclear Ring and Stellar Bar Dynamics	90
3.7 Conclusions	94

4	Gas Kinematics in Nuclear Rings	96
4.1	Overview	96
4.2	Sample and Observations	98
4.3	Data Reduction	101
4.4	Results	103
4.4.1	Rotation Curve	103
4.4.2	Non-circular Motions	115
4.4.3	Velocity Dispersion	129
4.5	Discussion	132
4.5.1	Non-circular Motions and Kinematics within Nuclear Rings . .	132
4.5.2	Non-circular Motions vs. Luminosity, Dispersion, and Star Formation	135
4.5.3	Non-circular Motions, The Bar, and x_2 Orbits	138
4.6	Summary	140
5	The Physical Conditions of the Ionized Gas in the Central KiloParsec of NGC 7742	142
5.1	Overview	142
5.2	Observations and Data Reduction	144
5.3	Results	146
5.3.1	Gas Density	148
5.3.2	Excitation Mechanisms	149
5.4	Discussion and Conclusions	152
6	Summary & Conclusions	155
7	Future Considerations	162
A	Individual H II Region Parameters for the Galaxies	164
B	Discussion of Rings with No Gradient	184
B.1	NGC 613	184
B.2	NGC 1300	184
B.3	NGC 4303	184
B.4	NGC 5248	185
B.5	NGC 5905	185
B.6	NGC 5945	185
B.7	NGC 5953	185
B.8	NGC 6503	186
B.9	NGC 7716	186
B.10	NGC 7742	186

LIST OF TABLES

2.1	Global parameters of the AuxPort sample	25
2.1	(Continued)	26
2.1	(Continued)	27
2.2	Distribution of H α morphology classes	40
2.3	Morphological and bar type distribution of circumnuclear H α emission	42
2.4	Nuclear and circumnuclear H α emission for different categories of nuclear activity	46
3.1	Morphological characteristics of the nuclear rings in the AuxPort sample	57
3.2	Contact point vs. location of youngest H II regions	78
3.3	Age distribution and H II region times	83
4.1	Morphological and photometric parameters of DensePak sample . . .	100
4.2	Kinematic parameters for the observed sample	109
A.1	EW, flux, and luminosity for NGC 278 H II regions	165
A.2	EW, flux, and luminosity for NGC 473 H II regions	166
A.3	EW, flux, and luminosity for NGC 613 H II regions	167
A.4	EW, flux, and luminosity for NGC 1300 H II regions	167
A.5	EW, flux, and luminosity for NGC 1343 H II regions	168
A.6	EW, flux, and luminosity for NGC 1530 H II regions	169
A.7	EW, flux, and luminosity for NGC 4303 H II regions	169
A.8	EW, flux, and luminosity for NGC 4314 H II regions	170
A.9	EW, flux, and luminosity for NGC 5248 H II regions	170
A.10	EW, flux, and luminosity for NGC 5728 H II regions	171
A.11	EW, flux, and luminosity for NGC 5905 H II regions	172

A.12 EW, flux, and luminosity for NGC 5945 H II regions	172
A.13 EW, flux, and luminosity for NGC 5953 H II regions	173
A.14 EW, flux, and luminosity for NGC 6503 H II regions	174
A.17 NGC 6503 - continued.	175
A.17 NGC 6503 - continued.	176
A.18 EW, flux, and luminosity for NGC 6951 H II regions	177
A.19 EW, flux, and luminosity for NGC 7217 H II regions	178
A.20 EW, flux, and luminosity for IC 1438 H II regions	179
A.21 EW, flux, and luminosity for NGC 7570 H II regions	180
A.22 EW, flux, and luminosity for NGC 7716 H II regions	181
A.23 EW, flux, and luminosity for NGC 7742 H II regions	182
A.23 NGC 7742 continued.	183

LIST OF FIGURES

1.1	M51 (Whirlpool Galaxy)	2
1.2	NGC 1300	3
1.3	x_1 and x_2 orbits	4
1.4	NGC 7742	7
2.1	<i>I</i> -band & continuum-subtracted H α images	30
2.1	(Continued)	31
2.1	(Continued)	32
2.1	(Continued)	33
2.1	(Continued)	34
2.1	(Continued)	35
2.1	(Continued)	36
2.1	(Continued)	37
2.2	Histogram of distribution of circumnuclear H α emission morphology with host galaxy type	42
2.3	Histogram of the distribution of nuclear H α emission morphology	43
3.1	Nuclear ring ellipse fits	60
3.1	(Continued)	61
3.2	PA and ellipticity of disk and nuclear ring	63
3.3	H II region fits of nuclear rings using SExtractor	64
3.3	(Continued)	65
3.4	SExtractor ring morphology variations	67
3.5	Nuclear ring age distribution	70
3.5	(Continued)	71

3.5	(Continued)	72
3.6	H α EW vs. time for an instantaneous and a continuous burst of star formation	75
3.7	H α EW vs. time for varying IMF slopes, upper limit masses, and metallicities	76
3.8	Histograms of the integrated SFR of the nuclear rings	89
3.9	Histogram of the distribution of angular offsets between the bar major axis PA and the locations of the youngest HII regions	91
3.10	Comparison of travel times from the bar major axis PA to the contact points versus times to the youngest H II regions	93
4.1	H α velocity fields	104
4.1	(Contiued)	105
4.1	(Contiued)	106
4.1	(Contiued)	107
4.1	(Contiued)	108
4.2	Rotation curve & tilted rings	110
4.2	(Contiued)	111
4.2	(Contiued)	112
4.2	(Contiued)	113
4.2	(Contiued)	114
4.3	Non-circular velocities	116
4.3	(Contiued)	117
4.3	(Contiued)	118
4.3	(Contiued)	119
4.3	(Contiued)	120
4.3	(Contiued)	121

4.3	(Contiued)	122
4.4	Dispersion maps	131
4.5	Position angle plots	133
4.6	H α Emission in Nuclear Rings	136
4.7	Dispersion vs. Luminosity	137
5.1	SAURON and DensePak maps	147
5.2	Radial variation of the [S II] $\lambda\lambda 6716, 6731$ line ratio	148
5.3	Diagnostic line-ratio diagrams	150

Chapter 1

Introduction

1.1 Spiral Galaxies

The morphological classification of "spiral" represents those galaxies that comprise a flattened disk of stars and gas, often with a luminous spherical bulge, and believed to be surrounded by a spherical halo, mostly comprised of dark matter. The stars are concentrated in the bulge and in the spiral arms, which radiate out from the center. Following Hubble (1936), spiral galaxies are classified into three basic subtypes - *Sa*, *Sb*, and *Sc* - according to three criteria: (1) the degree of openness of the spiral arm structure from close together and tightly wound to well separated and elongated, respectively; (2) the prominence of the bulge (i.e., mass and luminosity distributions), where the mass of the galaxy is most concentrated in the bulge in the *Sa* types, and most concentrated in the disk in the *Sc* types; and (3) the degree to which the spiral arms are resolved into stars and individual emission nebulae (H II regions), where the degree of resolution increases from *Sa* to *Sc*. Figure 1.1 shows an image of the spiral galaxy M51, otherwise known as the Whirlpool Galaxy (classification type SAbc).



Figure 1.1: HST image of M51 (Whirlpool Galaxy). The two spiral arms are clearly defined, which contain young hot stars. The nucleus is comprised of older stars, as exemplified by the yellowish color. credit: The Hubble Heritage Team (AURA/STScI/NASA)

1.2 Barred Spiral Galaxies

The majority ($\sim 70\%$) of nearby spiral galaxies are barred spirals (de Vaucouleurs 1963, Knapen et al. 2000, Eskridge et al. 2002), which are identified by the Hubble nomenclature SBa , SBb , or SBc , and parallel the spiral arm morphological classifications in normal galaxies. The bar radially emerges from the nuclear region with the spiral arms generally emanating from the ends of the bar rather than from the central bulge. Figure 1.2 is an example of a strongly barred galaxy, namely NGC 1300. The creation of the bar is generally thought to be the result of the superposition of leading and trailing waves. This effect builds over time via swing amplification, which creates a self-perpetuating bar structure (Binney & Tremaine 1987).



Figure 1.2: HST image of the barred galaxy NGC 1300. The arms of the galaxy are connected to the ends of the bar. credit: The Hubble Heritage Team (AURA/STScI/NASA)

Bars are rectangular in shape, with varying lengths, ellipticities, and strengths. Within the bars gas, dust, and high-energy particles can compress and induce large-scale shocks. These shocks are usually associated with the dust lanes, which are located on each side of the bar (Athanasoula 1992). The dust lanes can usually be seen extending from the nucleus to the spiral arms. They exist on the leading side of the bar (assuming the spiral arms are trailing), and are offset from the bar major axis. The shocks are accompanied by very strong shears, which could explain the absence of star formation in the dust lanes themselves, despite the high concentration of gas.

The gas flow that results from such nonaxisymmetric potentials (i.e., shocks and shears) is channeled to the central regions as it loses angular momentum (e.g., Schwarz 1981, Combes & Gerin 1985, Shlosman et al. 1990, Friedli & Benz 1993). The flow in and around a bar can follow simple periodic orbits, as pioneered by de

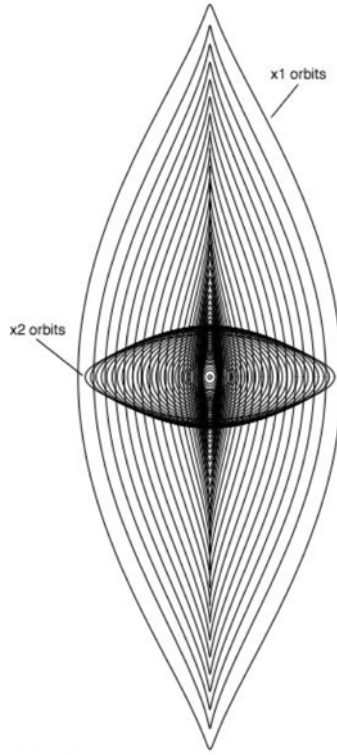


Figure 1.3: Numerical simulation of the morphology of x_1 and x_2 orbits from Regan & Teuben 2003.

Vaucouleurs & Freeman (1972) and Contopoulos & Papyannopoulos (1980). In the outermost parts of the bar, the flow lines are consistent with the elongated elliptical x_1 orbits. These non-intersecting orbits are aligned with the bar major axis, and provide the primary support for the bar. As the flow progresses inwards, the x_1 orbits gradually give way to x_2 orbits, which are perpendicular to the major axis. Figure 1.3 illustrates a hydrodynamically based representation of these two orbit families from Regan & Teuben (2003).

Theoretical analysis and observational data have confirmed that bars cause mass and angular momentum redistribution, which in turn strongly affect their host galaxies by influencing secular evolution of galaxies (e.g., Shlosman et al. 1989,

Friedli & Benz 1993, Kormendy & Kennicutt 2004, Sheth et al. 2005, Jogee et al. 2005). It is more difficult to observationally determine the time scales of bars in order to gauge if they have enough staying power to alter the morphology of their host galaxy. Several studies exist on the lifetimes of bars. Athanassoula (2002) and Shen & Sellwood (2004) support the idea that large-scale stellar bars live on the order of at least 2 Gyr. Jogee et al. (2005) refined that estimate with a large *Hubble Space Telescope (HST)* survey on the properties of stellar bars. They find that strong bars remain common from the present day out to look-back times of 8 Gyr ($z \sim 1$), and infer that bars are long-lived phenomenon with a lifetime well above 2 Gyr.

1.3 Nuclear Rings

A stable bar over time can cause secondary dynamically-based phenomenon to form, such as nuclear rings. The majority (\sim two-thirds; Buta & Combes 1996, Heller & Shlosman 1996) of nearby barred galaxies host various types of rings, classified as the SB(r)-variety. Kormendy (1979) categorized rings as nuclear, inner, or outer according to the ratio of the ring's radius to the length of the bar major axis. Inner rings, which lie between the bulge and the spiral arms, touch the ends of the bar, while outer and nuclear rings are larger and smaller than the bar, respectively. This thesis focuses on nuclear rings.

Some of the first examples of nuclear rings were identified by Morgan (1958), where he described four such objects as being made up of multiple “hotspots”.

Other authors have described nuclear rings as “a central knot surrounded by a chain of condensations forming a spiral arm” (Sersic 1958), and “a segmented annulus consisting of bright areas and probably dust” (Burbidge & Burbidge 1960), and more explicitly, “a ring of H II regions” (Peterson et al. 1976).

Nuclear rings are believed to form through radial gas flows associated with the gravitational torques of the bar (e.g., Athanassoula 1992, Piner et al. 1995). The bar creates dynamical non-axisymmetric forces, which in turn provide essential fuel for the formation and evolution of the nuclear ring by channeling the gas to the nuclear regions (e.g., Knapen et al. 1995a, Buta & Combes 1996, Regan et al. 1997). The efficient inflow of gas is due to the departure from axial symmetry (via shocks and shears within the dust lanes). This facilitates angular momentum transfer from the bar to the nuclear regions, slows down the gas inflow, and triggers star formation.

1.3.1 Photometry

Nuclear rings consist of distinct compact areas of young massive stars near the centers of spiral galaxies, and can sometimes dominate the overall star formation (SF) in early Hubble type barred spiral galaxies (Ho et al. 1997, Benedict et al. 2002, and Sheth et al. 2005). Figure 1.4 shows an example of such a ring in NGC 7742. This is evidenced by *UBVRI* surface brightness profiles and color index profiles (such as $B - I$ maps) for many ringed galaxies, which show blue young stars (e.g., Buta 1986, Hummel et al. 1987, Buta et al. 1987, Benedict et al. 1992, and Byrd et al. 1994). Barth et al. (1995) and Phillips et al. (1996) use *HST* imagery to



Figure 1.4: *HST* image of NGC 7742, which hosts a prominent nuclear ring around the active nucleus. The ring contains numerous resolved stellar clusters of young stars. Tightly wound spiral arms are faintly visible. credit: The Hubble Heritage Team (AURA/STScI/NASA)

show that nuclear rings contain very luminous, blue, compact star clusters whose star formation in the ring can represent $\sim 50\%$ to 80% of a galaxy's overall star formation.

Buta & Combes (1996) correlated the morphological type of nuclear rings to that of their host galaxies. In their survey, the distribution peaks at type *Sbc*, with no rings seen in types later than *Scd*, and very few in earlier types. A separate statistically-based survey of nuclear rings (Knapen 2005) noted a similar trend in morphological classification where nuclear rings are dominant in barred galaxies (*SAB* and *SB*), which supply the nuclear regions with ample gas to support such star formation. In Chapter 2, we will add further evidence that this is indeed the case. We classify the morphology of the nuclear and circumnuclear $H\alpha$ emission

for 74 galaxies, and confirm that late-type galaxies have a patchy circumnuclear appearance in $H\alpha$, and that nuclear rings occur primarily in spiral types Sa-Sbc.

1.3.2 Kinematics

Kinematic observations can help reveal significant clues on the dynamical processes of the bar, the nuclear ring, and on the interplay between the two structures. Kinematic studies of nuclear rings began in mid 1970's with the use of long slit spectroscopy. Rubin et al. (1975) and Peterson et al. (1976) obtained emission line velocities for the bar, inner ring, and nuclear ring of NGC 3351 and derived rotation curves and a velocity-position angle diagrams. They estimated the rotational velocity at $r = 0.3\text{kpc}$ (the location of the nuclear ring) to be $126 \pm 16 \text{ km s}^{-1}$, with a constant angular velocity of $80 \pm 20 \text{ km s}^{-1} \text{ kpc}^{-1}$ for the stars in the bar. Van der Kruit (1974) also used velocity-position angle diagrams to explore ring properties. He looked for asymmetries in the diagrams and connected such occurrences with possible noncircular motions in the case of NGC 4736.

The diagnostic tools currently used for kinematic studies are similar to those of the early works, but with much improved instrumentation such as two-dimensional integral field spectrometers, which can capture the entire ring in a single observation. Recent studies of nuclear rings in barred galaxies (e.g., Buta et al. 1998, Reynaud & Downes, Schommer et al. 1988, Wong & Blitz 2000, Jogee et al. 2002, Zurita et al. 2004) use radial velocity and residual maps to confirm large-scale deviations from simple circular motions of the ionized gas in the nuclear region. Observations of

NGC 5248 from Schommer et al. (1988) and Jogee et al. (2002) support a scenario where the nuclear ring is the result of gas inflow arising from the nonaxisymmetric bar potential. Reynaud & Downes (1998) find that, for NGC 1530, strong velocity changes are inversely correlated with star formation. Strong velocity changes indicate shocks and shears, which create an environment too turbulent to allow gas to form concentrated zones that may condense to form stars. Zurita et al. (2004) analyze the kinematic nuclear residual velocity pattern for NGC 1530 to reveal a spiraling inflow pattern into the nuclear ring. They also measure the velocity gradients perpendicular (i.e., along the minor axis) and parallel (i.e., along the major axis) to the bar and show that the radial velocities are much stronger in the perpendicular direction. Zurita et al. further find a relationship between the steep velocity gradients along the direction of the gas flow and the sites of intense star formation. The steep gradients, which are indicative of shocks, tend to be within a few hundred parsecs of the regions of strongest star formation. They conclude that possibly the compression along the line of flow is causing major gas condensation and, thus, star formation. In Chapter 4, we will expand the sample of such cases, by analyzing the rotational, residual, dispersion, and harmonic velocities for 10 nuclear rings.

1.4 Nuclear Rings as Starbursts

Nuclear rings are categorized as a type of ‘starburst’. Weedman et al. (1981) first used the term for a specific class of galactic nuclei with strong star formation, as evident by the $H\alpha$, $H\beta$, and $[O\text{III}]$ optical emission lines, in a small vol-

ume. They studied the nucleus of NGC 7714 and found that the $H\beta$ flux is 1.9×10^{-12} ergs cm^{-2} s^{-1} with a luminosity, $L(H\beta)$, of 3.5×10^{41} ergs s^{-1} , and $L(H\alpha)$ on the order of 10^{42} ergs s^{-1} . The lifetimes of starbursts are on the order of 10 to 100 Myrs. The massive bursts may be galaxy-wide, but are usually confined to a small region about the nucleus (few kiloparsec scales), and can dramatically alter the structure of the host galaxy with respect to morphology, gas and dust content, metallicity, and stellar population (Kormendy & Kennicutt 2004).

Kennicutt et al. (2005) summarize the wide-ranging definitions of a starburst, based on the past 25 years of literature, in terms of (1) its absolute star formation rate (SFR), where the SFR significantly exceeds the average found among normal galaxies, (2) its SFR surface density or intensity (i.e., the SFR per unit area), and (3) its SFR over a given period of time, where the current value exceeds the average past value by a fixed amount (usually characterized in terms of the birthrate parameter b). Kennicutt et al. plot the distribution of star formation properties of nearby galaxies from several surveys in terms of these three defining parameters to look for commonalities. They find that a starburst can be categorized as having an absolute SFR limit of $10 M_{\odot} \text{ yr}^{-1}$, a SFR intensity, Σ_{SFR} , limit of $0.1 M_{\odot} \text{ yr}^{-1} \text{ kpc}^{-2}$, and the ratio of present to past SFR (b) limit of $b \sim 2$ (a value that is 4 times higher than the mean ratio of 0.5 among non-bursting galaxies).

OB stars in Giant H II regions may dominate the light from these galaxies. H II regions are zones of hot ionized Hydrogen gas ($T \sim 10,000\text{K}$) around young massive star clusters that still contain OB stars. These stars are hot enough to produce a significant flux in ionizing radiation, shortward of the Lyman limit (Osterbrock

1989). Observationally H II regions are easily found by narrow-band imaging in, for example, the H α line, which is the strongest optical recombination line (if internal extinction is not too large). Diagnostic tools exist to help interpret the spectral properties of such massive star forming regions and act as a guide for classifying various photoionization environments such as galactic nuclei and H II regions. Veilleux & Osterbrock (1987) used emission line ratio analysis to better understand the physical characteristics of ionized regions and ultimately distinguish between starburst and AGN galaxies. In Chapter 5 we will use this method to dissect the circumnuclear environment of a galaxy known to contain both an AGN and a circumnuclear starburst ring.

Starbursts require a supply of gas at the rate ranging from a few $M_{\odot} \text{ yr}^{-1}$ to hundreds $M_{\odot} \text{ yr}^{-1}$ (as in the case of Ultraluminous Infrared Galaxies - ULIRGs; e.g., Flores et al. 2004). Galaxies that host nuclear starbursts must have both enough gas to fuel the activity and a mechanism to bring the gas supply towards the central region. Bars are one such mechanism. Many surveys corroborate this connection by statistically showing that nuclear starbursts occur preferentially in barred spiral galaxies (e.g., Dressel 1988, Arsenault 1989, Martinet & Friedli 1997, and review by Knapen 2005a). For example, Martinet & Friedli studied the properties of 32 well-known late-type barred galaxies and found that all of the galaxies displaying the highest current star forming activity have bars that are strong (i.e., an axis ratio less than 0.6) and long, where a greater fraction of the gas in the bar can be swept up and driven towards the center.

1.5 Nuclear Ring Models & Theories

The origin and dynamics of nuclear rings are rather difficult to study and interpret because of their small size (typically 1 kpc) and their proximity to the, sometimes very, bright nucleus. Although it is widely accepted that gravitational instabilities in dense molecular clouds lead to star formation in general (e.g., Evans & Lada 1991 and references therein), the number of models present indicate that formation and propagation mechanisms of nuclear rings are complex, with many factors involved (Schwarz 1981, Combes & Gerin 1985, Byrd et al. 1994, Knapen 1995b, Heller & Shlosman 1996, Regan & Teuben 2003). The most conventional process is that the nuclear ring is defined by the position of the ILR(s) (Simkin et al. 1980, Shlosman et al. 1989, Friedli & Benz 1993, Heller & Shlosman 1994, Buta & Combes 1996), which is typically at ~ 1 kpc from the galaxy center (e.g., Buta & Crocker 1993). In a barred potential, the nuclear ring forms at the ILR where the molecular gas accumulates and initiates star formation. The ring can be formed inside a spiral structure if the bar pattern speed, Ω_b , is around the inner Lindblad precession frequency ($\Omega - \kappa/2$), where Ω is angular velocity and κ is the radial epicyclic frequency. Other models corroborate the necessity of an ILR to drive nuclear ring formation, but have varying interpretations of the simulations. Athanassoula (1992) simulates the flow pattern between the ILR and corotation (i.e., where the pattern speed equals the circular angular velocity in the disk) and concludes that at least one ILR is necessary to produce shocks, which force the gas to flow radially towards the ILR along the bar dust lanes. Shocks become more

circular across the ILR and result in a azimuthal flow of star formation.

Heller & Shlosman (1996) analyze the properties of a growing nuclear ring in a barred galaxy to look for perturbations in the galactic potential. They find that the major periodic orbits within the corotation radius are significantly affected by the perturbation of the ring. Regardless of the shape of the ring, the phase space allowed to the x_2 orbits was substantially increased as the ring grew. In the case of an inner and an outer ILR (IILR and OILR, respectively) being present, the growth of the ring radially and vertically pushed out the location of the OILR, whereas the IILR moved inward only slightly. As the ring increases radially, the inner x_1 orbits become more rounded.

Knapen et al. (1995b) combine NIR imaging of NGC 4321 with modeling techniques to find a connection between the presence of two ILRs and location of the nuclear ring, which lie between the IILR and OILR. The existence of elongated isophotal twists in the K -band both outside and inside the ring can be viewed as direct tracers of the locations of the the ILRs and the x_2 orbits, which exist between the ILRs. They find that star formation within the resonance region is most intense close to its inner boundary at the IILR, whereas the OILR should be located outside of band of star formation.

Regan & Teuben (2003) offer a variation on the ‘traditional’ ILR connection with ring formation, where they show that the existence of nuclear rings is directly related to the interactions between the x_1 and x_2 orbit families, and not necessarily associated with the ILR(s). Even without the presence of an ILR, Regan & Teuben show that gas follows the x_1 family of orbits, which are aligned with the bar major

axis, and forms a nuclear ring when a threshold amount of the phase space is occupied by the x_2 orbits. In this scenario, Regan & Teuben conjecture that the radial extent of the x_2 orbits has no association with the location of the ILRs. They also simulated the kinematics of the gas and stars in nuclear rings by plotting radial and tangential velocities along the major and minor axes of the bar. They find that, although there exist no strong velocity transitions near the outer edge of the nuclear ring along the major axis of the bar, the ring is strongly influenced by the kinematics along the bar minor axis. Radial velocities changed from 40 to -70 km s^{-1} from the inner to the outer edge of the ring, transitions even stronger from the outer edge of the ring to radii larger than the ring (from 170 to 370 km s^{-1}). We will show that our findings are consistent with these results, although to a lesser extent.

The patchy appearance of the rings has also been modeled. In general, the gas in nuclear rings is subject to gravitational instabilities, which then trigger star formation and fragmentation. Ostriker, Stone, & Gammie (2001) and Semelin & Combes (2000) use hydrodynamical simulations to show that these dense concentrations of gas around the ILR are compressed and cooled to the point of sparking such star formation. Knapen et al. (1995a) model this phenomenon and added that the ring shapes, orientation, and star formation distribution should depend on the gas inflow rate. Low inflow rates result in round rings and smoother azimuthal distributions, while larger rates will force a more oval appearance with the ring's major axis leading the bar by 50° to 80° degrees. Regan et al. (1999) use numerical simulations to predict that the ring major axis is offset by 90° from the bar major axis. This orientation corresponds with the orientation of the stable x_2 family of

orbits, which are perpendicular to the bar major axis. In Chapter 3 we will see that the observational evidence for the Knapen et al. model is not overwhelming, but that the models from Regan et al. are very consistent with the H α images of many nuclear rings.

There is also a growing debate as to whether propagation mechanisms exist that could result in an age-dependent gradient around the ring. Elmegreen (1997) states that stellar winds from the massive young stars or supernova remnants could cause sequential turbulent triggering of the existing enriched H II environment. This “chain reaction” in the local environment could lead to the appearance of isolated age gradients over parts of the ring. A more global and dynamical process, as proposed by Regan et al. (1999) and others leads to the idea that the interaction with the bar directly creates smooth gradient distributions from one intersection point of the bar dust lane with the ring (i.e., contact point) to the other. With the main source of fuel emanating from the bar, gas piles up at the contact points, which creates a favorable environment for star formation. The stellar clusters would naturally propagate azimuthally and cause an age gradient until interactions from the second contact would dominate the star formation process and result in the same behavior. Observationally evidence is still lacking in this area. Ryder et al. (1999) and Allard et al. (2006) both find a bipolar age gradient in the nuclear ring of M100, with similar results from Sharp et al. (2004) for M83. No other literature sources were found. In Chapter 3, we will observationally show that, for 11 nuclear rings, a patterned azimuthal age distribution does exist, although, most are partial gradients.

1.6 Outline of Thesis

Although nuclear rings are known to exist in barred spiral galaxies, the details of their formation, evolution, and interaction with other host structures remain ambiguous. This interesting puzzle is a complex one due to the influence of perturbing components such as the bar, nuclear activity, local resonances, and gravitational instabilities around such active areas with large amounts of ionized gas. This thesis compiles both $H\alpha$ photometric and kinematic data of an unprecedented sample of nuclear rings to provide a more comprehensive view of the physical conditions of star formation within the ring, and across the inner and outer boundaries that define the ring. In particular, this thesis is designed to answer the following specific key astrophysical questions, which are topically arranged:

- What is the distribution of massive young stars in the nuclear and circumnuclear regions? How do the photometric morphologies of nuclear and circumnuclear $H\alpha$ distribution compare to the Hubble type and presence or absence of a bar in the host galaxy? Are our results consistent with previous observations that nuclear rings preferentially appear in barred spiral galaxies? Is there a possible link between nuclear rings and the presence of starburst galaxies and active galactic nuclei?
- What are the statistics for size, morphology, and luminosity of nuclear rings and the individual star-forming clusters that define the HII regions within the rings? How do these properties relate to the morphology of their hosts? Is there a relationship between the position angles and ellipticities of the rings

and those of their host galaxies? What are the dynamical time scales of nuclear rings? Is there an age gradient between the H II regions defining the ring, and if so, how do the distributions relate to the location of the bar and its dust lanes that intersect with the ring, as well as the morphology of the ring or its host galaxy?

- Are noncircular motions present within the nuclear rings? Is there a relation between the enhanced star formation seen in nuclear rings and the level of velocity residuals and dispersions within the rings? Are the velocity transitions across the ring and the ring boundaries stronger in the presence of a bar? If so, how do they relate to the location of the bar major and minor axes? Do the photometrically-determined nuclear ring parameters differ from those of the kinematic data? If so, what are the possible causes?
- Can we distinguish between different environments in a circumnuclear region that is known to be a composite of an AGN/LINER and a nuclear ring? How is the environment inside the nuclear ring characterized? Can the optical lines constrain the local gas density and metallicity within the ring? What are the ionization sources inside and outside of the ring?

In Chapter 2 we present optical imaging of the central regions of a sample of 73 spiral galaxies in the H α line and in optical broad bands, with the aim of studying the distribution of massive young stars in the nuclear and circumnuclear regions. We outline the observing and data reduction procedures, list basic properties, and present the *I*-band and continuum-subtracted H α images. We classify

the morphology of the nuclear and circumnuclear $H\alpha$ emission and explore trends with host galaxy parameters, which confirm that late-type galaxies have a patchy circumnuclear appearance in $H\alpha$, and that nuclear rings occur primarily in spiral types Sa-Sbc. We identify a number of previously unknown nuclear rings, and confirm that nuclear rings are predominantly hosted by barred galaxies.

In Chapter 3 we present results for a sub-sample of the galaxies presented in Chapter 2. The $H\alpha$ and continuum images reveal that the rings are comprised of several distinct star-forming H II regions within approximately one kiloparsec of the galaxy nucleus. We present morphological parameters of the rings and compare those to both bar and disk parameters. We find a clear relationship between the position angles and ellipticities of the rings and those of their host galaxies, which indicates the rings are in the same plane as the disk and are circular. We also compute the equivalent width of each $H\alpha$ -emitting (H II) region forming the nuclear ring, and use population synthesis models to estimate ages, which range from 1 Myr to 10 Myrs throughout the rings. We find that approximately half of the rings contain azimuthal age gradients that encompass at least 25% of the ring, although there is no apparent relationship between the presence or absence of age gradients and the morphology of the rings or their host galaxies. NGC 1343, NGC 1530, and NGC 4321 show clear bipolar age gradients, where the youngest H II regions are located near the two contact points of the bar and ring. We speculate in these cases that the gradients are related to an increased mass inflow rate and/or an overall higher gas density in the ring, which would allow for massive star formation to occur on short timescales, after which the galactic rotation would transport the H II

regions around the ring as they age. Two-thirds of the galaxies that host a bar show a correlation between the locations of the youngest H II region(s) in the ring and the location of the contact points, which is consistent with predictions from numerical modeling.

In Chapter 4, we utilize the DensePak fiber-optic array on the KPNO WIYN telescope to construct two-dimensional H α velocity fields of ten nuclear rings. We show that regions of enhanced star formation in the nuclear rings correspond to regions with (1) the strongest H α emission, (2) high luminosities of order 10^{40} erg s $^{-1}$ - 10^{42} erg s $^{-1}$, (3) low residual velocities of order 10 km s $^{-1}$, and (4) low velocity dispersions ranging from 20 km s $^{-1}$ - 50 km s $^{-1}$. Within the rings, star formation takes place in regions where the shear is minimal/small, and the gas is cool enough to allow molecular condensation. The lack of strong non-circular motions, coupled with a direct relationship between the position angles and ellipticities of the rings and those of their host galaxies, indicate the rings are in the same plane as the disk and are circular. Outside of the ring, we find a correlation between the largest velocity deviations from circular motion, seen near the ring outer edge, and the location of the bar minor axis, where the dominant family of orbits transitions from x_1 to x_2 . The few cases that exhibit significant kinematic and photometric PA offsets are attributed to complex bar interactions and/or galaxy mergers.

In Chapter 5, we present an emission-line diagnostic analysis of integral-field spectroscopic observations that cover the central kiloparsec of NGC 7742. This Sa galaxy hosts a spectacular circumnuclear ring and nuclear regions characterized by low-ionization emission. The gas in the ring rotates in the opposite sense to the stars

in the galaxy, suggesting a recent merging or acquisition event. The combination of integral-field measurements for the $H\alpha + [\text{N II}]$ emission lines from **DensePak** and the $H\beta$ and $[\text{O III}]$ emission from **SAURON** allow the construction of diagnostic diagrams that highlight the transition from star formation in the circumnuclear ring to excitation by high-velocity shocks or by a central AGN towards the center. **DensePak** measurements for the $[\text{S II}]$ line ratio reveal very low gas densities in the circumnuclear ring, $N_e = 20 \text{ cm}^{-3}$, characteristic of massive H II regions but not of typical nuclear starbursts. Comparison with MAPPINGS III models for starbursts with low gas densities show that the ring H II regions is of roughly solar metallicity. This suggests that the gas in the nuclear ring originated in a stellar system capable of substantially enriching the gas metallicity through sustained star formation. Past interaction with NGC 7743, a nearby barred spiral galaxy, could have provided such metal rich material, but the pristine conditions of both NGC 7742 and NGC 7743 rule out such an event. Instead, we suggest that NGC 7742 cannibalised a smaller galaxy rich in metal-poor gas, and that once the gas was funneled in the ring star formation may have proceeded long enough for the metallicity of the starburst to increase to its present value.

Chapter 6 and Chapter 7 provide a summary of this thesis and discuss future considerations, respectively.

Chapter 2

Morphology of Massive Star Formation in the Central Regions of Spiral Galaxies

(published in Astronomy & Astrophysics, Vol 448, p.489, 2006)

2.1 Overview

Enhanced nuclear activity in disk galaxies, whether in starburst or AGN form, appears to be an integral part of their evolution. Both forms of activity have been observed to co-exist (e.g., Heckman et al. 1997) and are a clear manifestation of the symbiotic evolution of galactic centres and their host galaxies. The observed tight correlation between the masses of the central black holes and the velocity dispersions in the surrounding bulges (e.g., review by Ferrarese & Ford 2005) provides the most direct evidence for this evolution and yields important clues on the dynamics, structure, and evolution of galaxies.

To initiate and to maintain the AGN or nuclear starburst activity, gas inflow must be stimulated from the disk to the central regions — a process which must be accompanied by a substantial loss of angular momentum in the gas. Theoretically, this leads to the suggestion that gravitational torques acting through galactic bars or galaxy interactions are involved. Due to the asymmetric nature of their mass distribution, they can facilitate the loss of angular momentum in inflowing material

(e.g., Shlosman, Begelman & Frank 1990; Athanassoula 1994; Combes 2001). Observationally, statistical links between bars and interactions on the one hand and the occurrence of starburst and AGN activity on the other are clear in certain circumstances (e.g., extreme starbursts and interactions), barely significant in others (e.g., low- L AGN and bars; low- L starbursts and interactions), and absent in the case of low- L AGN and interactions (e.g., review by Knapen 2004).

Massive SF can be convincingly traced by the accompanying $H\alpha$ emission and is very easily observed with standard telescopes and cameras (Kennicutt 1998). $H\alpha$ is mainly produced in the H II regions surrounding massive B and O stars, although shocks and non-stellar activity can also lead to $H\alpha$ emission. In the images of the 73 galaxies analysed here, we study the morphology of the $H\alpha$ emission in the circumnuclear, two kpc radius regions, as well as from the nucleus *per se*. The circumnuclear area as chosen is large enough to incorporate most nuclear rings. This kind of circumnuclear, low- L starbursts are found in around one fifth of spiral galaxies (Knapen 2005, hereafter K05), and characterise the dynamics of the host galaxy and its stellar bar (e.g., Buta & Combes 1996; K05).

We present our galaxy sample in Section 2.2, and describe the observations and data reduction procedures in Section 2.3. The nuclear and circumnuclear $H\alpha$ morphology is analysed in Sections 2.4 and 2.5, and relations to host galaxy properties, such as the presence of bars and nuclear activity and the morphological type, are discussed in Section 2.6. Section 2.7 lists our main conclusions from this chapter.

2.2 Sample selection and parameters

For this study, we selected galaxies with some prior evidence for $H\alpha$ structure in their central regions, either from the literature or from our own unpublished work. Since one of the aims of the current study is to identify nuclear rings, we have included a number of galaxies with known nuclear or inner rings, some of which have also been described in the works by Pogge (1989a, b), Buta & Crocker (1993), or K05. The observed sample is therefore not complete and any results must be interpreted with the appropriate care. For instance, the sample selection procedure will not allow a determination of the fraction of, say, nuclear rings in spiral galaxies.

The final sample, as observed by us with the William Herschel Telescope (WHT), consists of 73 galaxies spanning a range in many basic parameters, for which we obtained $H\alpha$, B and I imaging (see next Section for details). The galaxy sample is presented in Table 2.1, which also lists a number of important observational parameters as obtained from the literature. From the RC3 (de Vaucouleurs et al. 1991) we obtained the morphological type (col. 2), and the inclination and major axis position angle (in degrees, col. 4 and 5). From the NASA/IPAC extragalactic database (NED) we obtained a descriptor of the nuclear activity of the galaxy, for which we will distinguish between the four main categories Seyfert, LINER, starburst or HII, and none (col. 3). The recession velocity (in km s^{-1} , col. 6) was obtained from the RC3 for most galaxies, but from the NED for those where the RC3 does not list a value. The distance D to a galaxy (in Mpc, col. 7) was taken from the Nearby Galaxies Catalog (Tully 1988) whenever a value was given there; if not, we derived

it from the recession velocity assuming a Hubble constant of $H_0 = 75 \text{ km s}^{-1} \text{ Mpc}^{-1}$. The absolute blue magnitude (M_B , col. 9) was taken from Tully (1988), or derived from the distance where a galaxy is not included in the Tully catalogue.

NGC	Type	Activity (NED)	i ($^\circ$)	PA ($^\circ$)	v (km s^{-1})	D (Mpc)	Ref (D)	M_B (9)	Morph. N CN	
(1)	(2)	(3)	(4)	(5)	(6)	(7)	(8)	(9)	(10)	(11)
128	.L...P/		72	1	4241	56.6	1	-20.99	N	P
157	.SXT4..		50	40	1668	20.9	2	-20.06	W	P
210	.SXS3..		49	160	1634	20.3	2	-20.06	N	P
255	.SXT4..		34	15	1600	20.0	2	-19.26	N	P
278	.SXT3..		17		641	11.8	2	-19.62	N	R
470	.SAT3..	HII	52	155	2374	30.5	2	-20.05	N	P
473	.SXR0*.		51	153	2133	29.8	2	-19.77	W	R
488	.SAR3..		42	15	2269	29.3	2	-21.36	S	N
613	.SBT4..	Sy	41	120	1475	17.5	2	-20.53	S	R
628	.SAS5..		24	25	656	9.7	2	-20.32	W	P
772	.SAS3..		54	130	2458	32.6	2	-21.80	S	P
788	.SAS0*.	Sy2	41	75	4078	54.4	1	-20.68	S	N
864	.SXT5..		41	20	1560	20.0	2	-20.20	S	P
922	.SBS6P.		36		3092	41.2	1	-20.63	N	P
925	.SXS7..	HII	56	102	553	9.4	2	-19.66	N	P
1042	.SXT6..		39	15	1373	16.7	2	-19.91	W	P
1068	RSAT3..	Sy1 Sy2	32	70	1137	14.4	2	-21.39	S	P
1073	.SBT5..		24	15	1211	15.2	2	-19.44	N	P
1079	RSXT0P.		52	87	1447	16.9	2	-18.83	S	P
1084	.SAS5..		56	115	1406	17.1	2	-20.26	S	P
1087	.SXT5..		53	5	1519	19.0	2	-20.21	S	P
1140	.IB.9P*	HII Sy2	57	6	1509	18.2	2	-18.77	S	P

Table 2.1: Global parameters of the galaxies in the observed sample, obtained from the RC3 unless otherwise indicated. Galaxies are listed in order of increasing RA. Tabulated are the identification number of the sample galaxies (all are NGC numbers except IC 1438 (col. 1); the morphological type (col. 2); nuclear activity class (from NED; col. 3); inclination i as derived from the ratio of the major to the minor isophotal diameter (col. 4); position angle PA of the disk (col. 5); mean heliocentric radial velocity v , in a few cases obtained from NED (col. 6); distance D in Mpc (col. 7); reference for D , where 1 is v from col. 7 and assuming a Hubble constant of $H_0 = 75\text{km s}^{-1}\text{Mpc}^{-1}$, 2 is the Nearby Galaxies Catalog (Tully 1988; col. 8); absolute blue magnitude, taken from Tully (1988) whenever possible, otherwise derived from m_B (from the RC3) and the distance; morphological classification of the nuclear (col. 10; where 'N' means no emission, 'W' weak, 'S' strong, and 'P' position) and circumnuclear H α emission (col. 11; 'D' means diffuse, 'P' patchy, 'N' none, 'R' ring).

NGC	Type	Activity (NED)	i ($^{\circ}$)	PA ($^{\circ}$)	v (km s^{-1})	D (Mpc)	Ref (D)	M_B	Morph.	
(1)	(2)	(3)	(4)	(5)	(6)	(7)	(8)	(9)	(10)	(11)
1232	.SXT5..		29	108	1682	20.0	2	-21.11	N	N
1241	.SBT3..	Sy2	53	145	4030	26.6	2	-19.83	S	P
1300	.SBT4..		49	106	1568	18.8	2	-20.42	W	R
1302	RSBR0..		17		1703	20.0	2	-20.11	S	N
1343	.SXS3*P		51	80	2215	29.5	1	-18.85	W	R
1398	PSBR2..	Sy	41	100	1407	16.1	2	-20.57	S	N
1530	.SBT3..		58		2461	36.6	2	-21.32	N	R
1637	.SXT5..		36	15	717	8.9	2	-18.33	S	P
3982	.SXR3*		29		1109	17.0	2	-18.65	S	P
4303	.SXT4..	HII Sy2	27		1569	15.2	2	-20.71	S	R
4314	.SBT1..	LINER	27		963	9.7	2	-18.65	S	R
4321	.SXS4..	LINER HII	32	30	1586	16.8	2	-21.13	S	R
5248	.SXT4..	Sy2 HII	44	110	1153	22.7	2	-21.07	S	R
5383	PSBT3*P	Sbrst	32	85	2250	37.8	2	-20.96	N	P
5430	.SBS3..	HII Sbrst	58	0	2961	39.5	1	-20.11	N	P
5457	.SXT6..		21		241	5.4	2	-20.45	N	P
5701	RSBT0..	LINER	17		1506	26.1	2	-20.35	S	N
5728	.SXR1*	Sy2	55	0	2788	42.2	2	-21.67	S	R
5730	.I.9*		78	88	2533	33.8	1	-18.01	N	P
5850	.SBR3..		29	140	2556	28.5	2	-20.69	S	P
5905	.SBR3..	Sy1	49	135	3390	45.2	1	-20.69	N	R
5921	.SBR4..	LINER	36	130	1480	25.2	2	-20.67	S	P
5945	.SBT2..		21	105	5516	73.6	1	-20.63	S	R
5953	.SA.1*P	LINER Sy2	34	169	1965	33.0	2	-19.59	S	R
5970	.SBR5..	LINER HII	47	88	1963	31.6	2	-20.55	N	P
5982	.E.3...		41	110	3017	40.2	1	-20.98	S	N
6217	RSBT4..	Sy2	34		1362	23.9	2	-20.19	S	P
6384	.SXR4..	LINER	49	30	1663	26.6	2	-21.31	S	N
6412	.SAS5..		29		1324	23.5	2	-19.69	N	P
6503	.SAS6..	LINER HII	70	123	44	6.1	2	-18.64	W	R
6574	.SXT4*	Sy	39	160	2282	35.0	2	-20.76	W	P
6814	.SXT4..	Sy1.5	21		1563	22.8	2	-20.41	S	P
6907	.SBS4..		36	46	3161	42.2	1	-21.22	S	P
6946	.SXT6..	HII	32		52	5.5	2	-20.78	S	P
6951	.SXT4..	LINER Sy2	34	170	1426	24.1	2	-20.73	S	R
7130	.S..1P.	LINER Sy2	24		4842	64.6	1	-21.13	S	P
7217	RSAR2..	LINER Sy	34	95	946	16.0	2	-20.38	S	R
IC 1438	PSXT1*		32		2616	33.8	2	-20.08	W	R

Table 2.1: (Continued)

NGC	Type	Activity (NED)	i ($^{\circ}$)	PA ($^{\circ}$)	v (km s^{-1})	D (Mpc)	Ref (D)	M_B (9)	Morph. N CN	
(1)	(2)	(3)	(4)	(5)	(6)	(7)	(8)	(9)	(10)	(11)
7331	.SAS3..	LINER	69	171	821	14.3	2	-21.10	S	P
7469	PSXT1..	Sy1.2	44	125	4916	65.6	1	-21.08	S	R
7479	.SBS5..	LINER Sy2	41	25	2378	32.4	2	-21.11	S	P
7550	.LA.-..	AGN	29		5072	67.6	1	-20.99	W	N
7570	.SB.1..		54	30	4698	62.6	1	-20.09	N	R
7606	.SAS3..		67	145	2233	28.9	2	-21.28	S	D
7672	.S..3..	Sy2	41		4010	53.5	1	-18.94	S	P
7716	.SXR3*.		34	35	2571	33.7	2	-19.84	S	R
7723	.SBR3..		47	35	1875	23.7	2	-20.29	S	P
7727	.SXS1P.		41	35	1814	23.3	2	-20.38	S	D
7741	.SBS6..		47	170	755	12.3	2	-18.76	P	P
7742	.SAR3..	LINER HII	0		1653	22.2	2	-19.65	S	R
7769	RSAT3..	LINER HII	17		4214	56.2	1	-20.93	S	P

Table 2.1: (Continued)

2.3 Observations and data reduction

All the imaging presented in this paper has been obtained using the Auxiliary Port (Aux Port) camera on the 4.2m WHT, operated by the Isaac Newton Group in La Palma. The bulk of the imaging was obtained during a total of four observing nights granted by the UK time allocation panel (1999 September 16 and 17, and 2000 July 25 and 26), with additional imaging obtained in service mode during a number of nights in 1999 and 2000. We also used images of a few galaxies (e.g., NGC 4314 and NGC 4321) obtained during earlier observing runs with the WHT. The images of NGC 4321 have been published before by Knapen et al. (1995a, b).

The Aux Port camera is a small optical camera without any re-imaging optics located at a dedicated folded cassegrain focus of the WHT. Its small pixel scale (0.11 arcsec/pixel) combined with a 1024×1024 pixel TEK CCD and round filters yields a circular field of view (FOV) of about 1.8 arcmin in diameter. We used Harris

B and *I* filters, and one of the narrow-band filters 6570/55, 6594/44, 6607/50, 6626/44 or 6656/44, depending on the systemic velocity of the galaxy, where the numbers denote $\lambda/\Delta\lambda$, or the central wavelength of transmission and the width of the transmission curve, both in Å. We used typical exposure times of 1, 3, and 10 minutes in *I* and *B*, and $H\alpha$, respectively. Atmospheric conditions were good in general, and the resulting spatial resolution as measured from the reduced images is around 0.8 arcsec in the $H\alpha$ and *I*-band images, and around 1.0 arcsec in *B*.

The data reduction process followed basic procedures for bias subtraction and flat fielding using twilight sky flat fields. Image registration was done by measuring the positions of foreground stars where available, and the centre of the galaxy in all cases. For the subtraction of the continuum from the $H\alpha$ images we used the *I*-band images. We determined the scaling factor by applying the procedure described by Böker et al. (1999) to all individual sets of $H\alpha + I$ images. This method uses the fact that most pixels in any set of two registered images of a galaxy will show continuum emission, whereas only a minority show continuum plus line emission. When plotting all individual pixels, those tracing the continuum will scatter along a narrow, well-defined band, the slope of which denotes the scaling factor to be used for the continuum subtraction. Pixels containing $H\alpha$ emission will end up above this band (assuming that $H\alpha$ intensity is plotted as the ordinate). We refer the reader to the papers by Böker et al. (1999) and Knapen et al. (2004a) for a more detailed description. Knapen et al. (2004a) discuss the uncertainties introduced by using *I*-band imaging for continuum subtraction, and conclude that the resulting errors in the luminosities of HII regions are smaller than some 5%, and that the resulting

H α morphology is reliable.

The *I*-band and continuum-subtracted H α images of all sample galaxies are shown in Figure 2.1 . The *B*-band images (not shown here) generally outline a morphology similar to that shown in H α , though less pronounced in showing the star forming regions.

2.4 H α morphology: Methodology and limitations

2.4.1 Nuclear H α emission

We have chosen to limit the classification of the nuclear H α morphology to three categories: strong, weak, and none. This is mainly because of the uncertainties in the continuum subtraction using *I*-band images in the very centres of our galaxies, where differential dust extinction can play a more prominent role than in the disk (Knapen et al. 2004a). These classifications apply to the central point source — in practise the nuclear region of one seeing element in size. The exact position of the nucleus in a galaxy was determined from the *I*-band image. To qualify as a strong H α source, a nuclear point source must be more luminous than any other H α -emitting region in the galaxy. To qualify as weak, a nuclear H α peak must be present but stronger peaks are found outside the nucleus. Obviously, our category “none” describes those cases where no believable H α emission can be observed from the nucleus. In one case (that of NGC 7741) we could not pinpoint the location of the nucleus (not even using the near-IR image from Knapen et al. 2003), and this galaxy is thus not included in the following discussion.

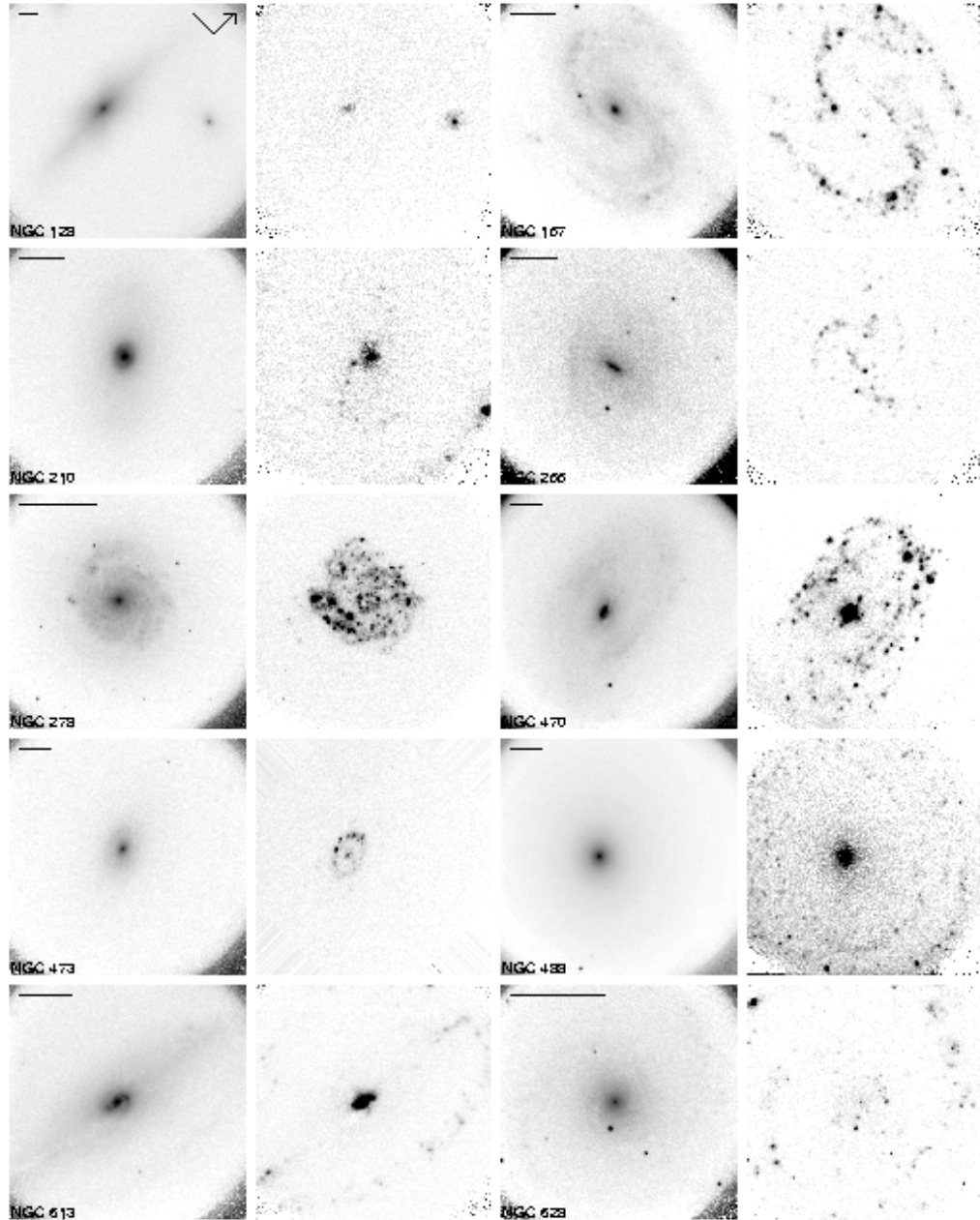


Figure 2.1: Grey-scale representation of the *I*-band and continuum-subtracted $H\alpha$ images of all sample galaxies, with the former shown on the left in each pair. The orientation is North up and East to the left, except for those cases where East and North are indicated in the upper right corner of the *I*-band image, and where the arrow points North. The scale is indicated for each galaxy by the length of the black line in the top left corner of the *I*-band image, which corresponds to 2 kpc.

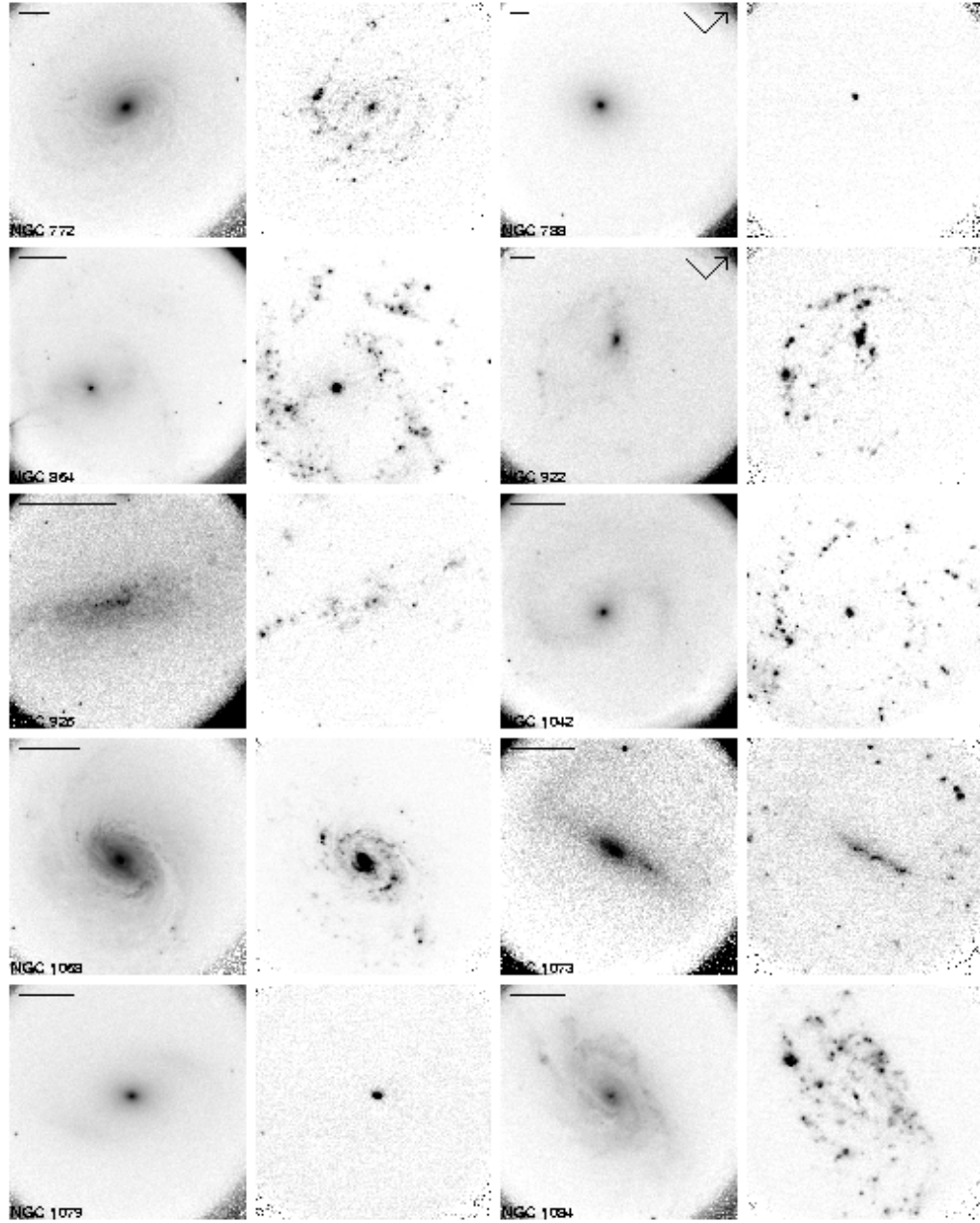


Figure 2.1: (Continued)

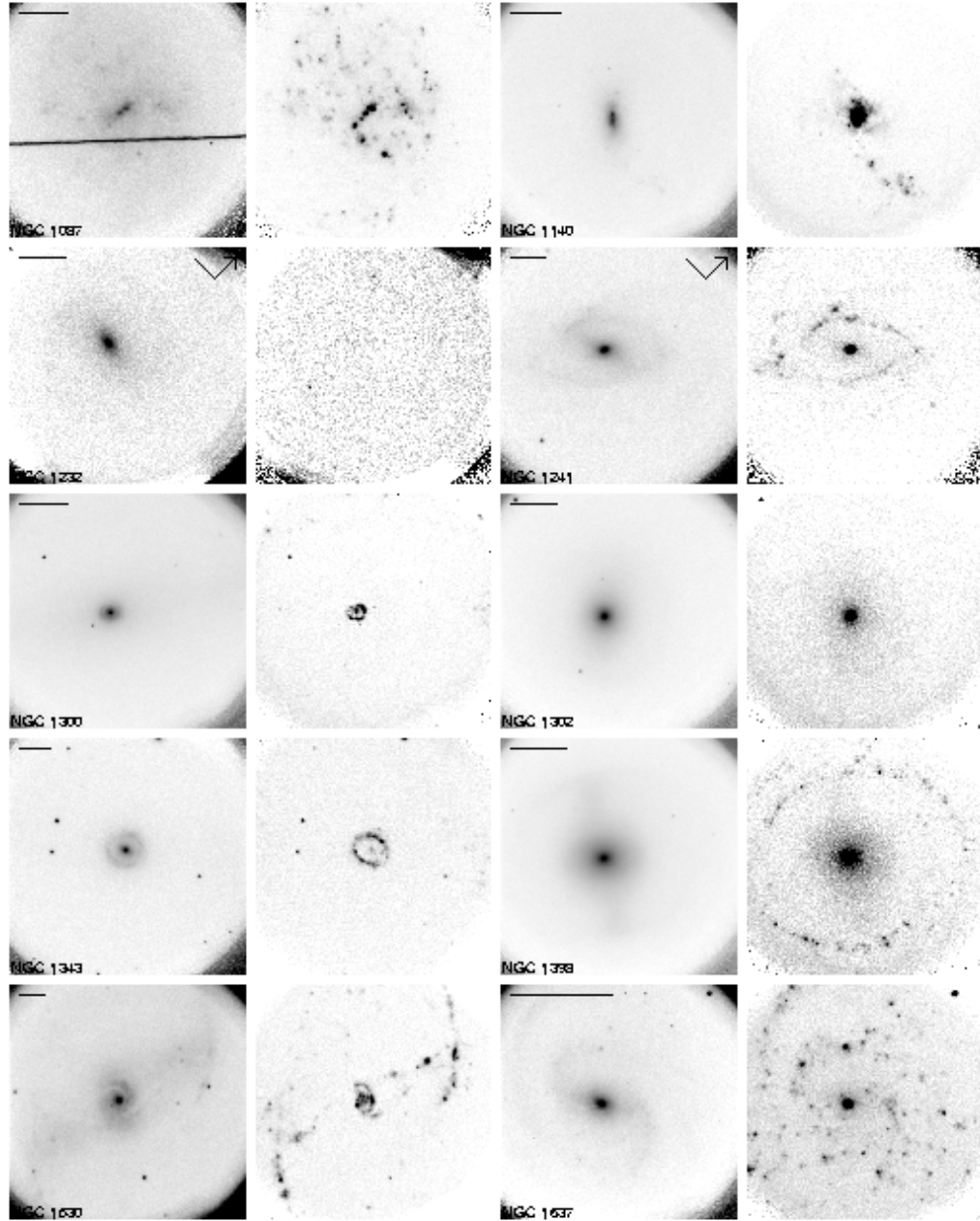


Figure 2.1: (Continued)

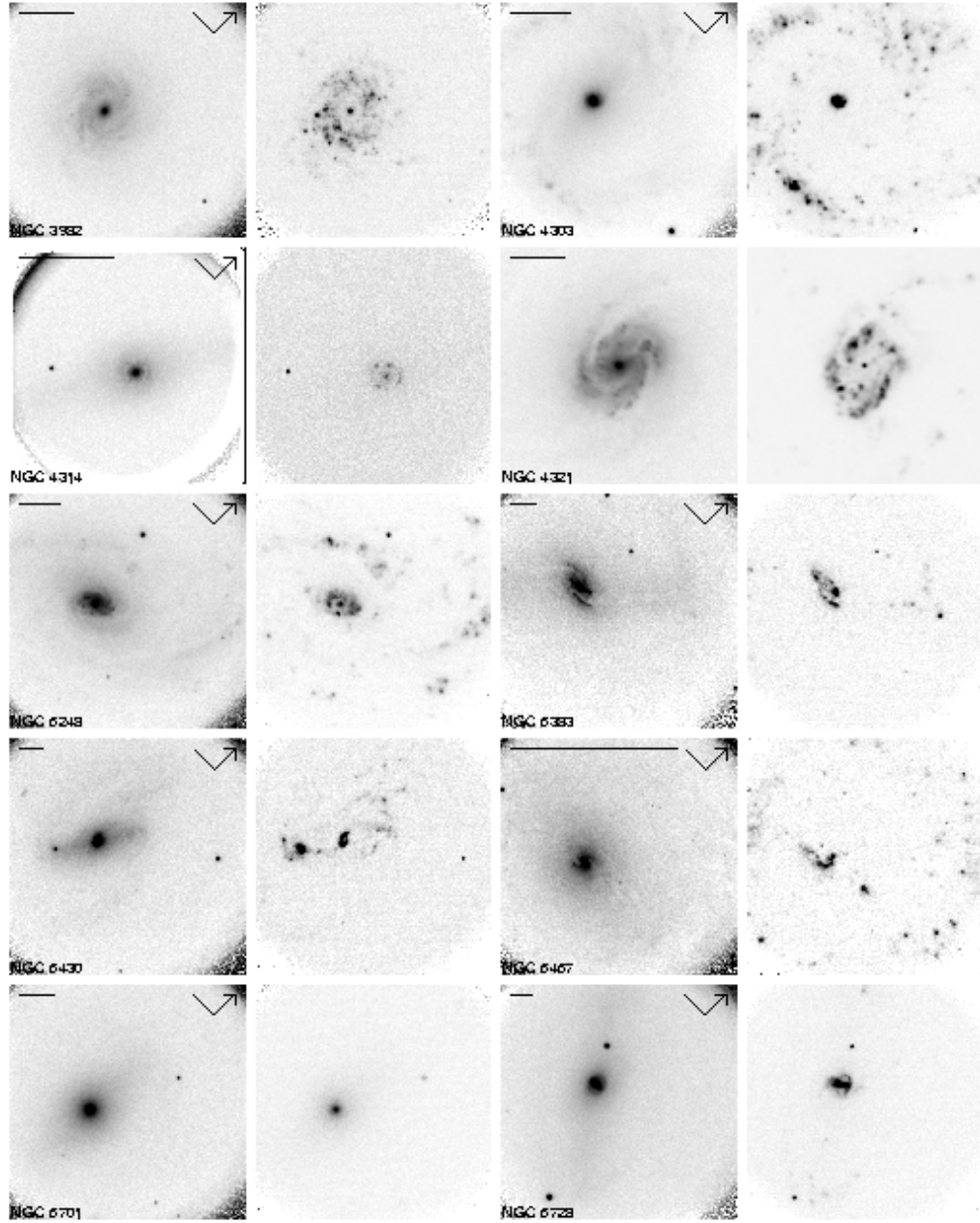


Figure 2.1: (Continued)

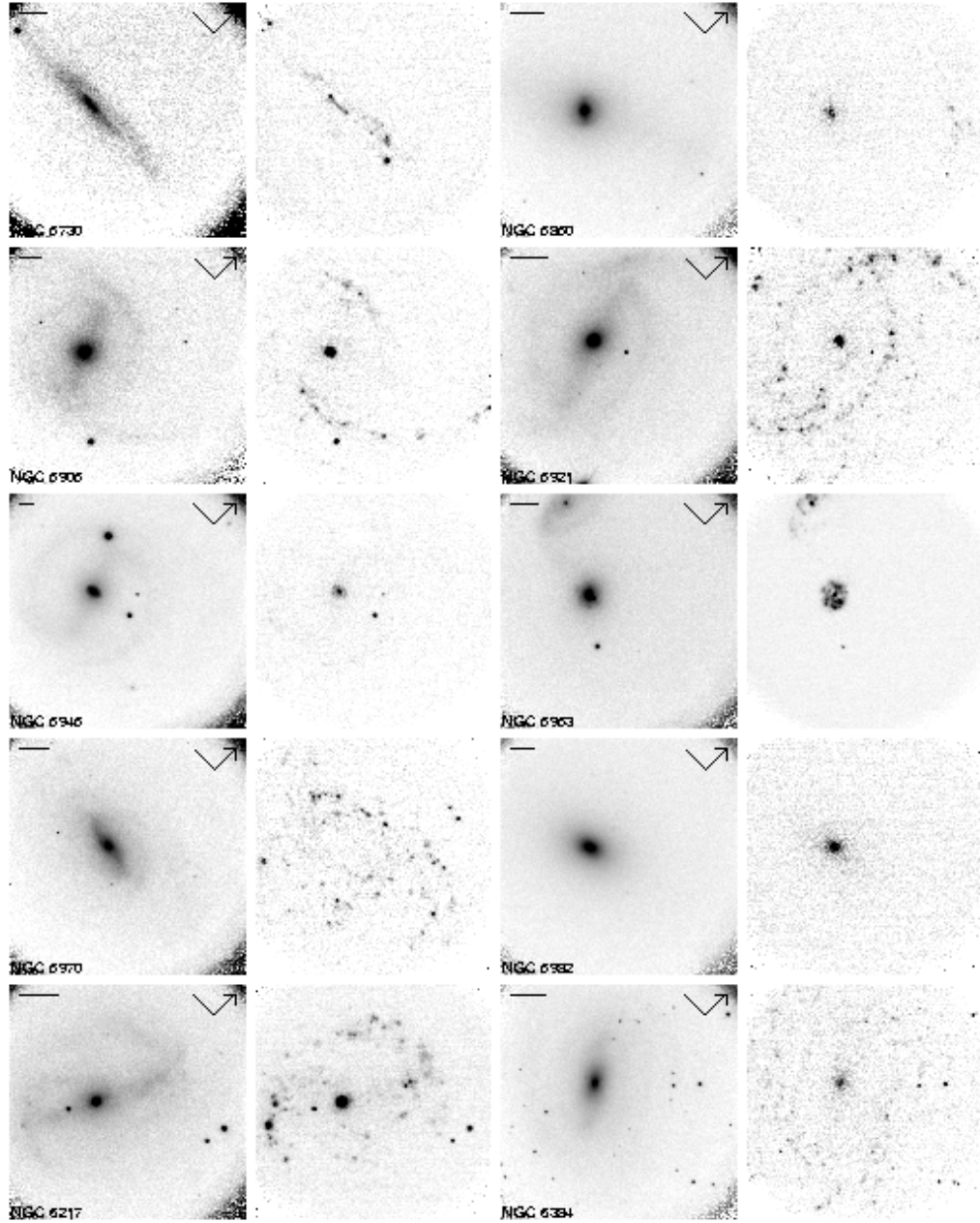


Figure 2.1: (Continued)

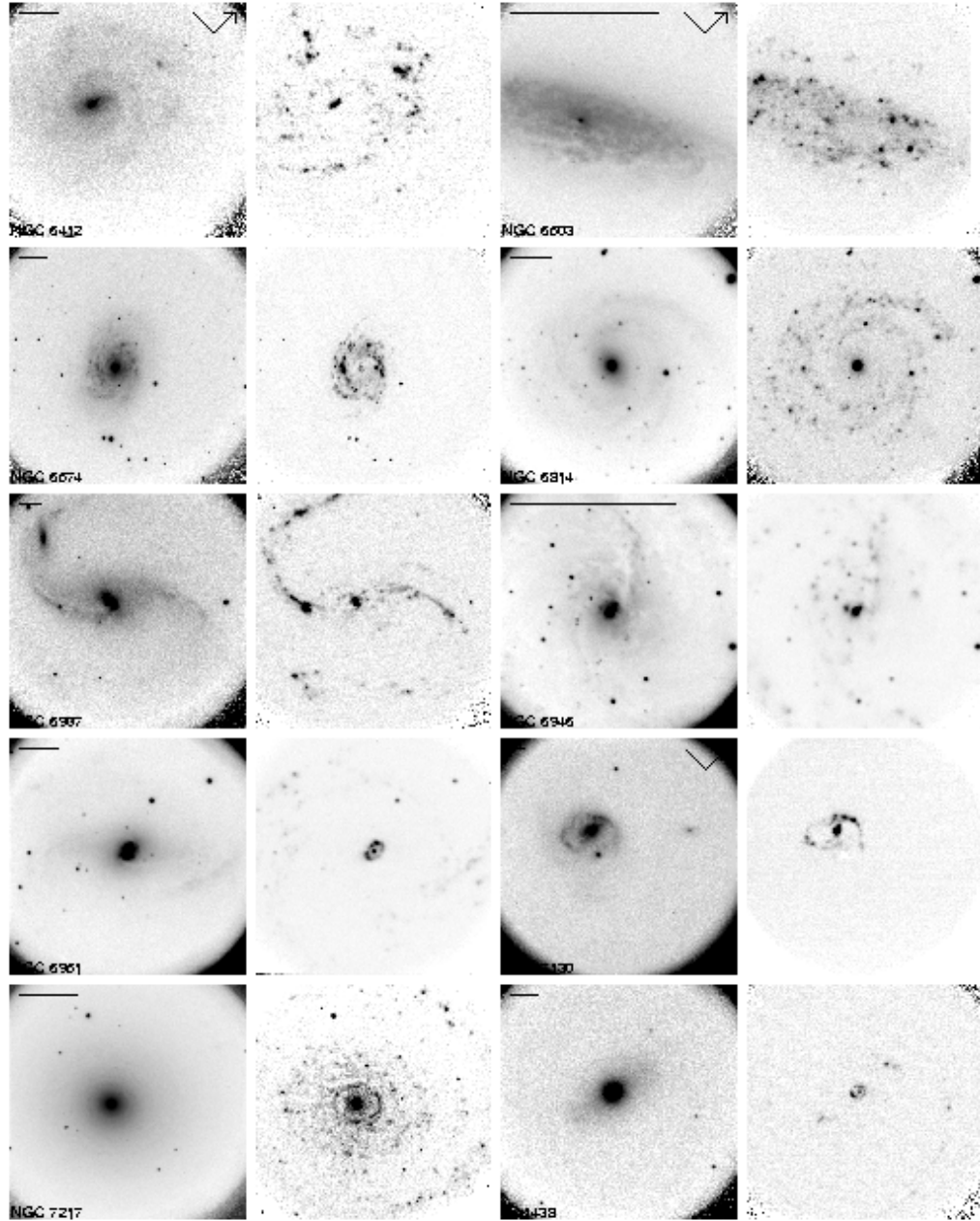


Figure 2.1: (Continued)

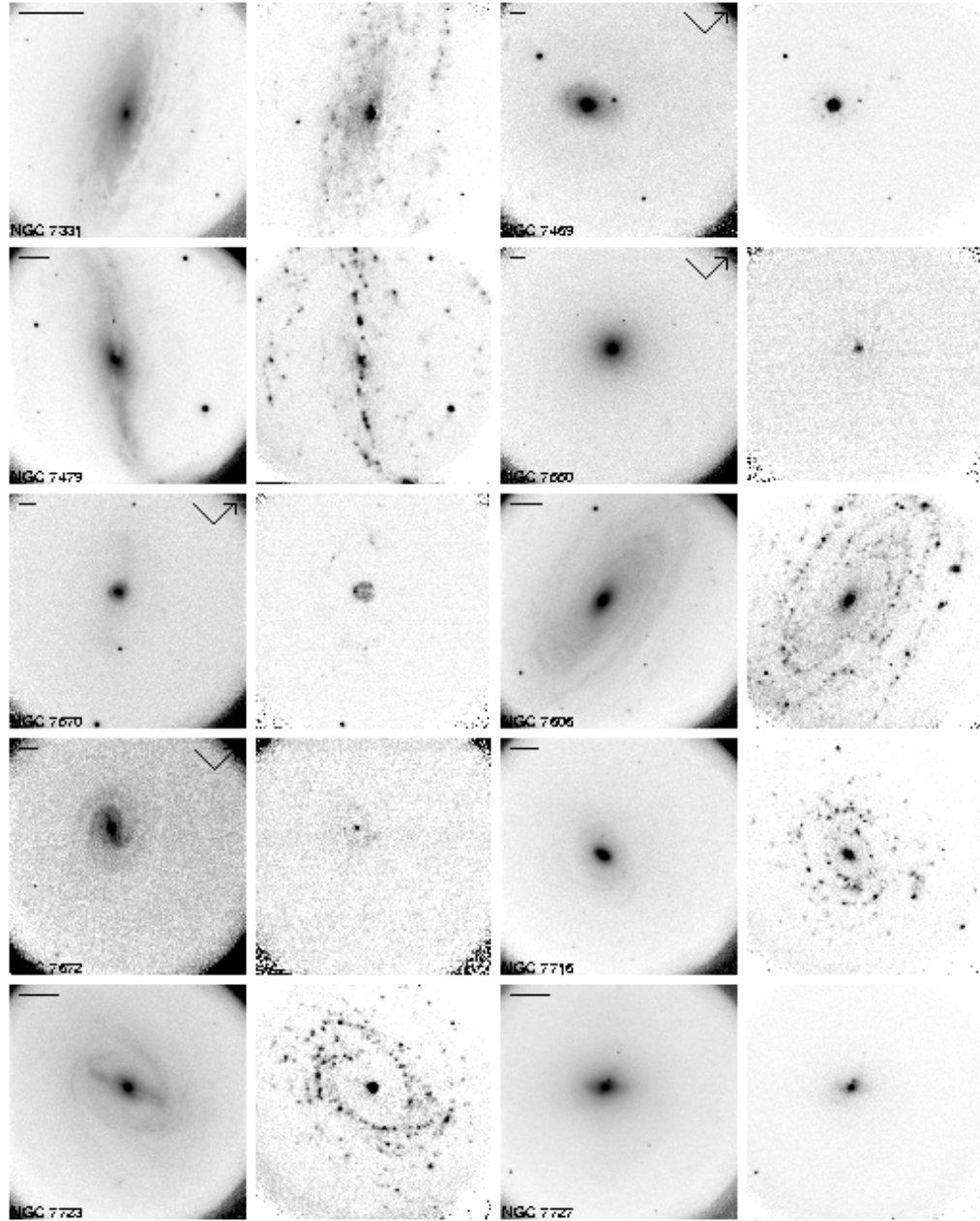


Figure 2.1: (Continued)

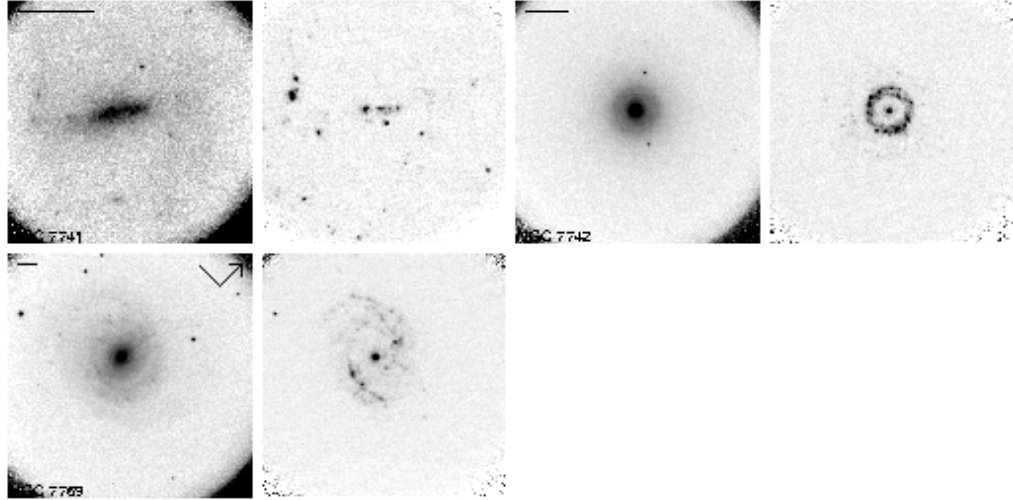


Figure 2.1: (Continued)

2.4.2 Circumnuclear H α morphology

For the purpose of this paper, we consider the morphology of the H α emission in the circumnuclear region as that arising from outside the nucleus and within a radius of 2.0 kpc from the nucleus of the galaxy. The range in distances to our sample galaxies, from 5 to 74 Mpc (Table 2.1), implies that this 2 kpc radius corresponds to a range of linear sizes in our images, varying roughly from 77 arcsec to 6 arcsec. The H α morphology was classified by visual inspection of the images within the appropriate radial area.

We used a minimal number of different morphological classes, following the scheme introduced by K05. The main categories are, first, “none”, where obviously no H α emission is detected in the circumnuclear region (there will usually be emission from the nucleus). Second, “patchy”, where individual and clearly delimited patches of H α emission are detected, tracing individual H II regions, but not in an obvious ring pattern. The “patchy” class includes galaxies where the circumnuclear H II regions form a spiral pattern, but because such a pattern is hard to classify simply and unambiguously, we have not explicitly classified such cases as spiral. Third, “ring”, which denotes H α emission organised into a well-defined nuclear ring. In three galaxies, circumnuclear H α is detected which is not confined to individual patches, and these three galaxies have been classified “diffuse”. The classifications are given in Table 2.1.

Of the 22 nuclear ring galaxies reported here, to the extent of our knowledge three have not been reported as nuclear ring hosts in the literature. These newly

identified nuclear rings are those in NGC 473, NGC 5953, and NGC 7716.

The classification scheme used here is rather coarse, but we believe that it offers a good compromise between the need for classification and the enormous variety encountered in the detailed H α morphology from galaxy to galaxy. This variety is no doubt partly due to the nature of H α emission - originating in regions of massive star formation whose ionised gas emission will show a strong time evolution.

We will not discuss the fractions of galaxies in our sample which show patchy, ring-shaped, or no H α emission, because the selection criteria of our sample imply that any conclusions from such a discussion would have no wider significance. This is in contrast to the study of K05, where the selection of a statistically meaningful sample leads, for instance, to the result that one of every five spiral galaxies has a nuclear ring. What the current sample can be used for, except of course for selecting sub-samples of specific interest such as the nuclear ring sample of Chapter 3, or for referring to individual objects, is an analysis of how ascertain circumnuclear H α morphology is distributed with respect to host galaxy parameters such as morphological class or presence of a bar, provided that reference is made to the distribution of such parameters across the whole sample under consideration (next Section).

2.5 H α morphology and host galaxy parameters

2.5.1 Overall results

The results on the overall distribution of the different H α morphology classes are summarised in Table 2.2. Strong nuclear emission is found in 44 of our 73

Emission	N	d (Mpc)	M_B (mag)
(1)	(2)	(3)	(4)
Overall sample			
	73	23.9	-20.4
Nuclear emission			
Strong	44	23.8	-20.6
Weak	10	24.5	-20.1
None	18	31.0	-20.1
Circumnuclear emission			
Patchy	39	22.8	-20.2
None	9	26.6	-21.0
Ring	22	26.5	-20.4
Diffuse	3	28.9	-21.0

Table 2.2: Median values of the host galaxies' distance (in Mpc, from Tully 1988; col. 3), and absolute magnitude (calculated using m_B from the RC3 and the distance; col. 4), for the overall sample and the different classes of nuclear and circumnuclear emission (col. 1; the number of galaxies in each category is shown in col. 2).

sample galaxies, while 10 are classified as having weak nuclear $H\alpha$ emission, and 18 as having no $H\alpha$ emission at all. The circumnuclear $H\alpha$ emission is patchy in more than half of our galaxies (39 out of 73), and in the form of a nuclear ring in 22. A further 9 galaxies show no circumnuclear $H\alpha$ emission at all, and 3 have diffuse emission.

Table 2.2 also lists the median values of a number of key host galaxy parameters for the overall sample and for the different classes of nuclear and circumnuclear $H\alpha$ emission. We have listed distance and absolute blue magnitude. The only trend worth noting for the nuclear $H\alpha$ emission is that those galaxies without $H\alpha$ emission from the nucleus are, in the median, further away than those with emission, which is easily understood as related to sensitivity and detection. Those galaxies with strong $H\alpha$ peaks in the nucleus are slightly brighter than others, but this may be a

morphological type effect (see next section). As for the circumnuclear $H\alpha$ emission, Table 2.2 shows how the 12 galaxies with or without diffuse $H\alpha$ emission are fainter than the others. Those with patchy $H\alpha$ emission are, in the median, at smaller distances from us.

2.5.2 Morphological type of the host galaxy

T -type

Table 2.3 lists the distribution of the various classes of nuclear and circumnuclear morphology with spiral T -type, as obtained from the morphological classifications listed in the RC3 (the translation of T -type as used in the RC3 and more widely used descriptors of the type Sa, Sb, etc., is given in the header to Table 2.3). These results are shown as histograms in Figures 2.2 and 2.3 for the circumnuclear and nuclear $H\alpha$ morphology, respectively. The results confirm those presented by K05. The overall distribution of T -type for the sample shows a peak near types Sb and Sbc ($T = 3$ and 4, see Table 2.3), a broad distribution ranging from S0 to Sm, and a lack of galaxies of type Sdm. For two galaxies, no T -type is given in the RC3. We reiterate that no attempts were made at the sample selection stage to achieve a specific type distribution.

Galaxies with patchy *circumnuclear* $H\alpha$ morphology tend to be of later types, and in fact there are only two galaxies of the 19 of type later than Sbc which are *not* classified as patchy (an Sc with no circumnuclear $H\alpha$, and an Scd with a ring). Ring-like morphology is preferentially found in earlier types, peaking at Sb and Sbc

Emission	<i>N</i>	Morphological type <i>T</i>											Spiral type			
		0 S0	1 Sa	2 Sab	3 Sb	4 Sbc	5 Sc	6 Scd	7 Sd	8 Sdm	9 Sm	-	SA	SX <i>N</i> (%)	SB	-
(1)	(2)	(3)	(4)	(5)	(6)	(7)	(8)	(9)	(10)	(11)	(12)	(13)	(14)	(15)	(16)	(17)
	73	5	8	3	22	14	10	6	1	0	2	2	16 (22)	28 (38)	24 (33)	5 (7)
		Total sample														
		Nuclear emission														
Strong	44	4	6	3	13	10	5	1	0	0	1	1	11 (25)	16 (36)	14 (32)	3 (7)
Weak	10	1	1	0	1	3	1	2	0	0	0	1	3 (30)	6 (60)	1 (10)	0 (0)
None	18	0	1	0	7	1	4	2	1	0	1	1	2 (11)	6 (33)	8 (44)	2 (11)
Position	1	1														
		Circumnuclear emission														
Patchy	39	1	1	0	13	7	9	5	1	0	2	0	8 (21)	14 (36)	14 (36)	3 (8)
None	9	3	0	1	1	1	1	0	0	0	0	2	3 (33)	2 (22)	3 (33)	1 (11)
Ring	22	1	6	2	6	6	0	1	0	0	0	0	4 ¹ (18)	11 (50)	7 (32)	0 (0)
Diffuse	3	0	1	0	1	0	0	0	0	0	0	1	1 (33)	1 (33)	0 (0)	1 (33)

Table 2.3: Morphological and bar type distribution of the various types of circumnuclear H α emission. For the whole sample and for the nuclear and circumnuclear emission, col. 2 gives the total number of galaxies in each category (as described in col. 1), with the number of galaxies of each morphological type (from the RC3) in columns 3-13, and bar type (from the RC3) in columns 14-17. In these four columns, the numbers in brackets are the percentages of the total.

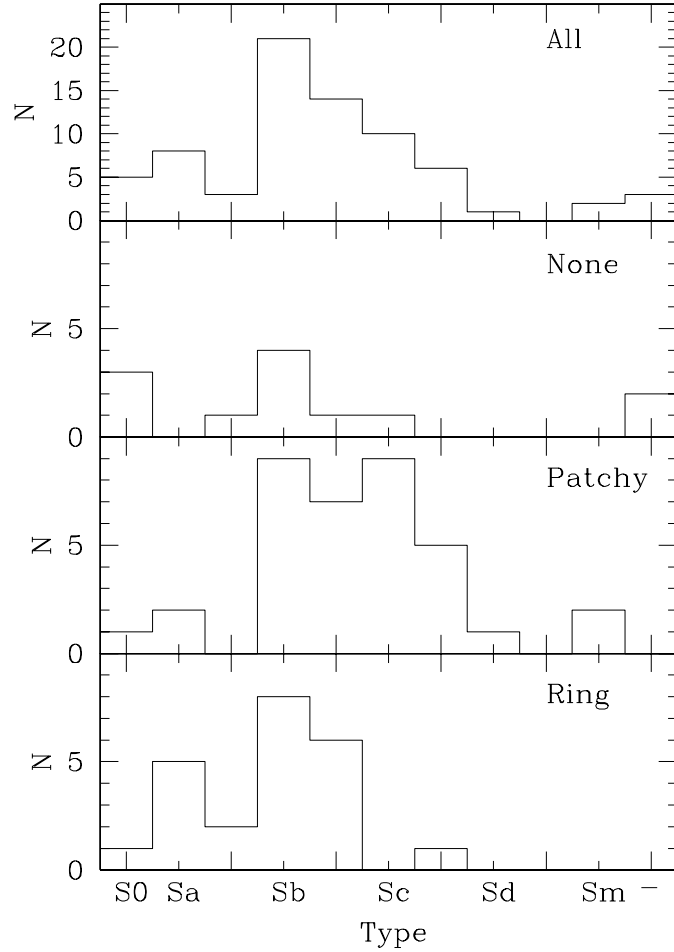


Figure 2.2: Set of histograms showing the distribution of circumnuclear H α emission morphology with host galaxy type, the latter obtained from the RC3.

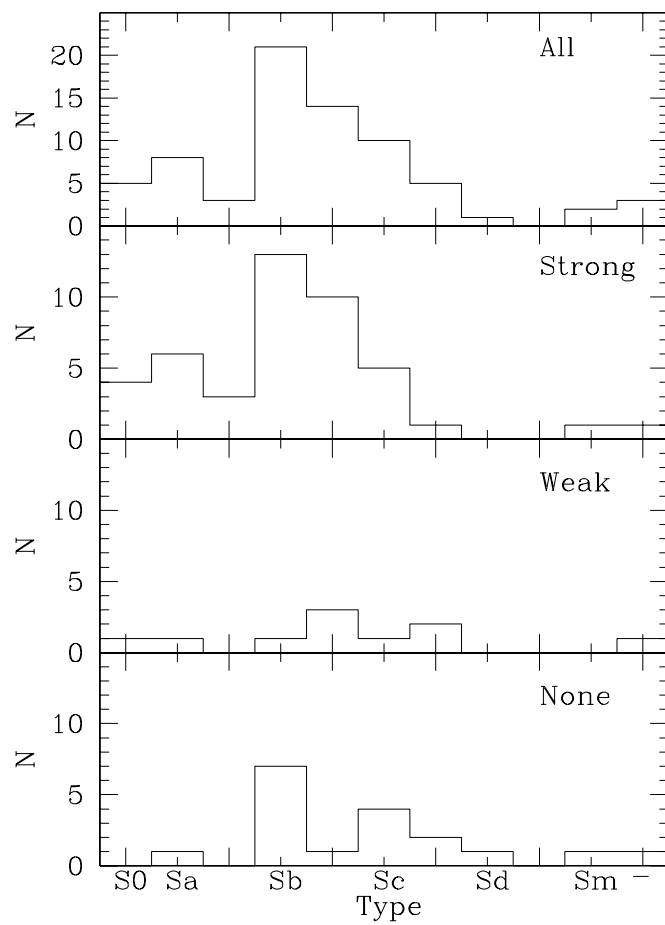


Figure 2.3: Set of histograms showing the distribution of nuclear H α emission morphology.

types. Galaxies with no circumnuclear H α emission are also preferentially of early type, confirming the findings of K05.

Not much can be deduced from the distribution of *nuclear* H α morphology with morphological type of the host galaxy (Figure 3) because of the relatively low numbers of galaxies with weak, or no, nuclear H α emission, but the *T*-type of the host does not seem to correlate with the presence of relative strength of the nuclear H α emission.

Bars

The distribution of H α morphology has been tabulated (Table 2.3) for the various bar classifiers used in the RC3: SA, SX (often quoted as SAB), and SB, in Table 2.3. Five galaxies have merely been classified as 'S' in the RC3 and are not considered here. The distribution between SA, SX, and SB classes seen across the whole sample is closely mirrored in the sub-samples of different nuclear and circumnuclear H α morphology. The numbers in the Table might appear to indicate a slight excess of SX galaxies among those with weak nuclear H α , and a slight lack of SA galaxies among those with no nuclear emission. Poisson statistics show that in either case the significance of this difference is at most 1σ . Considering the same number from the perspective of non-barred vs. barred galaxies, we see that $69\% \pm 12\%$ of the non-barred (SA) vs. $58\% \pm 7\%$ of the barred (SX+SB) galaxies has “strong” nuclear H α emission, $19\% \pm 10\%$ vs. $13\% \pm 5\%$ “weak”, and $13\% \pm 8\%$ vs. $27\% \pm 6\%$ “none”. Again, none of the differences are significant.

The bar distribution in the galaxies in the different classes of circumnuclear emission mirror those in the overall sample closely (the apparent deviations in the case of the three SA and two SX “none” galaxies are a 1σ effect). Table 2.3 shows explicitly how the percentages of barred and non-barred galaxies are rather stable for the different classes of morphology. Calculating the percentage of the different morphology classes for barred and non-barred galaxies, we see the same effect, for instance, $50\% \pm 13\%$ of non-barred (SA) galaxies have a patchy circumnuclear H α morphology, versus $54\% \pm 7\%$ of barred galaxies (SX+SB). These numbers are $19\% \pm 10\%$ vs. $10\% \pm 4\%$ for “none”; and $25\% \pm 11\%$ vs. $35\% \pm 7\%$ for “ring” (but see below).

The galaxies hosting circumnuclear rings in H α only show a rather moderate preference for SX and SB hosts, which at first sight may appear to be at odds with the findings of K05, who confirmed the standard picture that bars are almost exclusively responsible for the existence of nuclear rings. In fact, K05 pointed out that of the 12 nuclear ring hosts considered, only two have been originally classified as non-barred SA, but that each of those two has clear evidence from near-IR imaging for the existence of a bar. We will discuss the four SA-type nuclear ring host galaxies in the current sample in more detail in Sect. 2.5.4.

2.5.3 Starburst and AGN activity

We have scanned the NED for nuclear activity classifications of our sample galaxies. As explained in K05, the information from NED may not be as reliable

	Total	AGN	H II/SB	non-AGN	non-AGN non-SB
Nuclear emission					
Sample size	72	31	5	41	36
Strong	44	26	1	18	17
Weak	10	3	–	7	7
None	18	2	4	16	12
Circumnuclear emission					
Sample size	73	31	5	42	37
Patchy	39	13	5	26	21
None	9	5	–	4	4
Ring	22	13	–	9	9
Diffuse	3	–	–	3	3

Table 2.4: Nuclear and circumnuclear H α emission for different categories of nuclear activity, basically AGN (including LINER-type activity) and starburst. Column 2: total sample. Column 3: AGN, which includes all galaxies classified in NED as either Seyfert or LINER. Column 4: H II/SB, all galaxies classified by NED as starburst or H II (excluding those whose classification also includes a LINER or Seyfert which have been classed AGN). Column 5: All galaxies not classified as Seyfert or Liner. Column 6: as col. 5, but now also excluding the galaxies of col. 4.

as a uniformly conducted spectroscopic survey, although K05 showed that this did not significantly alter their results. In addition, our sample includes galaxies at larger distances than those in K05. More galaxies may thus not have been checked for nuclear activity in detail, and will hence, by default, have no nuclear activity classifier in the NED. The results are tabulated in Table 2.4, which shows that of our 73 sample galaxies, 31 have been classified as AGN of some sort (we include Seyfert, LINER, and “AGN” types in this category), with another five galaxies classed as starburst using various nomenclature, including “H II”.

The results, then, show two interesting features which are worth discussing here. The first is the significantly higher fraction of AGN which show strong nuclear H α emission. Only a handful of galaxies, in fact, show weak or no nuclear H α emission. Any AGN should have H α emission, but the absence in the few cases

where we report it can be explained as a differential extinction effect. We use the significantly redder I -band for the subtraction of the continuum from the relatively bluer $H\alpha$ line, which in a dust-extincted environment will lead to surplus subtraction. This will lead to artificially reduced $H\alpha$ central peaks. Galaxies classified as starbursts (or “H II”) but with “none” nuclear $H\alpha$ emission may well suffer from the same effects. Another possibility is that the classification as AGN or starburst as given on the NED is in fact erroneous, but checking that is outside the scope of this paper.

The second interesting feature from Table 2.4 is the enhanced fraction of AGN among the nuclear ring host galaxies. Of the AGN, 42% have a ring, against 30% of the complete sample. Conversely, 59% of the ring galaxies have an AGN, versus 42% of the complete sample. K05 found a similar effect, but much more marked; there, almost all nuclear rings were accompanied by AGN or starburst activity.

The ring-AGN connection occurs partly because both rings and AGN are most common among the early-type galaxies. Of our sample, 52 galaxies (71%) have $T \leq 4$ (Sbc), but 21 out of our 22 rings (95%) and 26 out of our 31 AGN (84%) are hosted by galaxies of such early types. This means that half of all $T \leq 4$ galaxies are AGN, and statistically 10.5 ring hosts will also host AGN. We concur with K05 in finding a higher number than this statistically expected one. As discussed in more detail by K05, the connection between rings and AGN is most likely to be through the availability and recent inflow of gas, which fuels both the massive star formation in the ring and nuclear activity. In this interpretation, the nuclear rings are merely a by-product of the gas inflow from the disk toward the very central

region (Shlosman 2005). A fraction of the inflowing gas moves further inward, and is ultimately responsible for the AGN activity.

2.5.4 Nuclear rings and their dynamical origin

We identify 22 nuclear rings, three of which have not been reported in the literature so far (those in NGC 473, NGC 5953, and NGC 7716). These are star-forming nuclear rings, classified as such purely on the basis of our $H\alpha$ imaging. There may be a small number of additional rings which are, for instance, too small, or too dusty to be picked up by our imaging (the latter category might well include NGC 1241, for which Böker et al. (1999) find a small nuclear ring in $Pa\alpha$ which is absent from our $H\alpha$ image). Of the 22 nuclear rings, Table 2.1 shows that four occur in galaxies classed as unbarred (NGC 5953, NGC 6503, NGC 7217, and NGC 7742). In addition, NGC 278, although classified as SX in the RC3, does not in fact have a bar. Knapen et al. (2004b) made a detailed study of this galaxy, and found from an analysis of near-IR and optical ground-based images, as well as of *Hubble Space Telescope* (*HST*) imaging, that there is no evidence at all for the presence of a bar. Radio 21 cm interferometry, however, showed that the outskirts of the galaxy have a severely irregular and disturbed morphology and kinematics in HI, indicative of at least a minor merger event in the recent history of the galaxy. Knapen et al. (2004b) postulate that this minor merger lies at the origin of the massive star forming in the nuclear ring, rather than a bar as is more conventional for nuclear ring hosts. Considering that the favoured formation scenario of a nuclear ring is

one where the ring forms in the vicinity of inner Lindblad resonances set up by a non-axisymmetry in the gravitational potential, due to, e.g., a bar or an interaction (see, e.g., Athanassoula 1992; Knapen et al. 1995b; Buta & Combes 1996; Heller & Shlosman 1996; Knapen et al. 2004b), it is instructive to scrutinise the four cases identified here of nuclear rings in supposedly non-barred galaxies.

- NGC 5953 (classed as SA but interacting): this galaxy forms part of a small interacting group of galaxies with NGC 5954 (visible in Fig. 1) and UGC 9902. Hernández-Toledo et al.(2003) report the presence of a small (~ 60 pc) “bar-like central structure”. As in the case of NGC 278, it is plausible that this interaction has led to the formation of the nuclear ring, and the disturbed and complex HI morphology and kinematics observed by Chengalur et al.(1994) lends support to this suggestion.
- NGC 6503 (classed as SA but inclined): this galaxy is rather inclined ($i = 70^\circ$) and it is thus very unlikely that any bar can be detected from optical or near-IR imaging – we postulate from statistical grounds only that this ring galaxy is most likely to be in fact barred. The HI velocity field is regular (Shostak, Willis, & Crane 1981; van Moorsel & Wells 1985), but Bottema & Gerritsen (1997) find evidence for a separate kinematically distinct nuclear component.
- NGC 7217 (classed as SA): this is a well-studied galaxy which in fact has three rings (e.g., Combes et al. 2004 and references therein). There is no evidence for a bar, but Merrifield & Kuijken (1994) reported the presence of the distinct counter-rotating disk population. Although this is evidence for a

past merger history, its current gravitational effects are most probably limited. The velocity field as seen from HI mapping is regular (Verdes-Montenegro et al. 1995). Buta et al. (1995) and Combes et al. (2004) show that there is an oval distortion in this galaxy, which can explain the occurrence of its three rings (nuclear, inner, outer). This may well be an indicator of a historical, but now destroyed, bar.

- NGC 7742 (classified as SA): This is another well-known ring galaxy, without any evidence for a bar or other asymmetry (Rix & Zaritsky 1995; Kornreich, Haynes, & Lovelace 1998). No HI velocity field is available from the literature. De Zeeuw et al. (2002) describe, on the basis of SAURON integral field spectroscopy, that the gaseous ring counter-rotates with respect to the central stellar component. We present a detailed emission-line ratio analysis of this galaxy in Chapter 5.

We thus summarise that of the four nuclear ring host galaxies classified as SA in the RC3, one is interacting, and one is too inclined to allow us to see any bar it may have. The remaining two galaxies (NGC 7217 and NGC 7742) do not have a bar. NGC 7217 has an oval distortion, which is able to maintain the nuclear ring, as shown by simulations (Combes et al. 2004). It is possible that the nuclear ring was formed during a recent bar episode, of which the oval distortion is the remnant. This scenario is supported by the presence of three rings in this galaxy, at the right resonant locations. NGC 7742 has not been studied in nearly as much detail, has no evidence for an oval, but does have counter-rotating gas and stars in the nuclear

region.

NGC 278, although classified as SX in the RC3, does not have a bar, but does show clear evidence for a recent minor merger (Knapen 2004b). We can thus conclude that none of the galaxies reported here challenges the standard scenario of nuclear ring formation to a significant degree. In this scenario, gas and ensuing massive SF accumulate near one or more inner Lindblad resonances, induced by an asymmetry in the gravitational potential of the host galaxy, in turn due to a bar or an interaction. Galaxies like NGC 278, NGC 7217, and NGC 7742 which appear at first sight bar-less and isolated, remain excellent test cases which warrant detailed studies.

In Chapter 3 we will present a detailed discussion of the properties of the 22 nuclear rings, and of how these properties relate to those of their host galaxies and of their host bars, where those exist. We will also discuss the identification and age determination of the individual H II region complexes or stellar clumps within the rings. We will also compare the observed azimuthal age gradients, or lack thereof, around the rings to dynamical models of ring formation.

2.6 Conclusions

We obtained a set of images in the B and I broad bands and in $H\alpha$ of a sample of 73 spiral galaxies. The data, obtained with the WHT and mostly at a spatial resolution of below an arcsec, are presented here, along with a classification of the morphology of the nuclear and circumnuclear $H\alpha$ emission. Most galaxies in our

sample have relatively strongly peaked nuclear $H\alpha$ emission, and patchy emission from the 2 kpc radius circumnuclear region, the latter indicative of the presence of individual $H\text{ I}$ regions. We explore trends with host galaxy parameters, and confirm that late-type galaxies have a patchy circumnuclear appearance in $H\alpha$, and that nuclear rings occur primarily in spiral types Sa-Sbc. We identify three previously unknown nuclear rings. Although we report four cases where a nuclear ring is hosted by an unbarred galaxy, we confirm that nuclear rings are predominantly hosted by barred galaxies. Bars thus stimulate nuclear rings, but do not influence the relative strength of the nuclear $H\alpha$ peak, nor other aspects of the circumnuclear $H\alpha$ morphology.

Chapter 3

A Connection between Star Formation in Nuclear Rings and their Host Galaxies

(submitted to the Astrophysical Journal, May 2006)

3.1 Overview

Nuclear rings consist of distinct compact areas of young massive stars near the centers of spiral galaxies, which can dominate the overall star formation (SF) in early Hubble type barred spiral galaxies (Martinet 1995; Buta & Combes 1996; Kormendy & Kennicutt 2004). Theories for nuclear ring formation vary. It is commonly accepted that the location of nuclear rings is close to the Inner Lindblad Resonance(s) (ILRs), which are neutral zones of negligible net torque that allow gas to accumulate and star formation to ensue (Pogge 1989; Shlosman, Begelman, & Frank 1990; Benedict 1993; Knapen et al. 1995a). Alternate theories include those from Kenney, Carlstrom, & Young (1993), who claim that nuclear rings can be remnants of a nuclear starburst, and Regan & Teuben (2003), who show that the rings are related to the presence of x^2 orbits.

Nuclear rings are typically within the central kiloparsec, and contain a mixture of neutral and ionized gas and dust with masses of 10^8 to $10^{10} M_{\odot}$ (Heller & Shlosman 1996; Rubin, Kenney, & Young 1997). These rings are a key component in the

dynamical evolution of their host galaxy and can interrupt the gas flow into the galactic center, which may in principle prevent the formation of an AGN or a nuclear starburst (Knapen et al. 1995b; Heller & Shlosman 1994; Heller & Shlosman 1996). The perturbing effects of nuclear rings have also been shown to alter the morphology of two major periodic families of orbits, x_1 and x_2 , that are within the corotation radius (Piner, Stone, & Teuben 1995; Heller & Sholsman 1996; Regan & Teuben 2003).

The great majority of nuclear rings are found in barred spiral galaxies, where the bar provides essential fuel for the formation and evolution of the ring via shock-induced channeling of disk gas to the nuclear regions (e.g., Schwarz 1981; Combes & Gerin 1985; Shlosman, Begelman, & Frank 1990; Athanassoula 1992). The shocks can act as instigators for angular momentum loss, which is crucial for directing the gas towards the central regions and forming nuclear rings. In such a picture massive SF would result and be most intense near where the bar dust lanes intersect the ring, called the contact points. The contact points can lead the bar by as much as 90° with respect to the galactic rotation (Heller & Shlosman, 1996; Regan, Vogel, & Teuben 1997; Regan et al. 1999; Ryder, Knapen, & Takamiya 2001; Allard, Peletier, & Knapen 2005).

While many galaxies with nuclear star-forming rings have been identified (Knapen 2005 states that 20% of local spirals host them), it is hard to generalize on the physical mechanisms behind the triggering and propagation of massive SF due to the inconsistent and incomplete nature of the existing data. To allow for a more statistical approach to answering some of the mysteries of these rings, we

performed an imaging survey of 73 galaxies in $H\alpha$ and the B and I bands, many of which host nuclear rings. An overview of this survey is presented in Knapen et al. (2006; hereafter Paper I). In Paper I we classified the morphology of the nuclear and circumnuclear HII regions and confirmed that (1) most late-type galaxies have a patchy circumnuclear appearance in $H\alpha$, (2) nuclear rings occur primarily in spiral types Sa-Sbc, and (3) found that the presence or absence of a close companion does not significantly affect the $H\alpha$ morphology around the nucleus nor the strength of the nuclear $H\alpha$ peak.

Of these 73 galaxies, we identified 22 that host nuclear rings as judged from our $H\alpha$ images, of which 19 were previously known as such. This paper isolates the individual H II regions forming the nuclear rings. We present information on the observations and data reduction in Section 3.2. We derive morphological parameters of the rings using ellipse fitting, and then compare those to the disk characteristics, in Section 3.3. In Section 3.4, we identify and analyze the H II regions forming the rings, compute their equivalent widths (EWs), and estimate error budgets. Using evolutionary models, we convert the EWs of the H II regions to ages and discuss the assumptions we make with respect to the type of starburst activity occurring in and around the rings in Section 3.5. We present our age distribution analysis, star formation rate estimations, and a discussion of the stellar bar dynamics with respect to the rings in Section 3.6, before summarizing our conclusions in Section 3.7.

3.2 Observations and Data Reduction

The ring images presented here are part of a larger William Herschel Telescope (WHT) imaging survey conducted to characterize the nuclear and circumnuclear morphology in nearby galaxies (Paper I). We selected galaxies with some evidence for $H\alpha$ structure in their central regions, either from the literature (e.g., Buta & Combes 1996; Buta & Crocker 1993) or from our own past work. Since one of the aims of our overall study is the detailed analysis of nuclear rings, our sample was biased towards certain morphological classifications known to host such features.

The images presented in this paper have been obtained using the Auxiliary Port (Aux Port) camera on the 4.2m WHT, operated by the Isaac Newton Group in La Palma. The camera's circular field of view (FOV) is $\sim 1'.8$ in diameter, imaged with a 1024×1024 pixel TEK CCD. The angular sizes of the nuclear rings in our sample vary between $5''$ and $30''$, which fit well into the FOV. We used Harris B and I filters, and one of four narrow-band $H\alpha$ filters, depending on the systemic velocity of the galaxy. We refer the reader to Table 3.1 of Paper I for a listing of the complete sample, along with their global parameters. Table 1 of the present paper lists morphological type, ring ellipticity, position angle (PA) of the disk and bar, and derived ring size for our subsample of 22 galactic nuclear rings.

We observed spectrophotometric standards to calibrate the $H\alpha$ images, and photometric standards to calibrate the B and I band images. We observed the standards through the same filters as the galaxies, with exposure times ranging from 5 to 20 seconds. The instrumental magnitude of each star in each filter was

NGC	Morph Type	ϵ_r	PA_r ($^\circ$)	$Size_r$ ($''$)	$Size_r$ (kpc)	PA_d ($^\circ$)	PA_b ($^\circ$)	SFR ($M_\odot \text{ yr}^{-1}$)
(1)	(2)	(3)	(4)	(5)	(6)	(7)	(8)	(9)
278	SAB(rs)b	0.06	120	4.4×4.1	0.2×0.2	-	no bar	0.5
473	SAB(r)0/a	0.37	160	12.2×6.9	1.7×1.0	153	164	2.2
613	SB(rs)bc	0.3	122	5.1×2.6	0.4×0.2	120	110	2.2
1300	(R)SB(s)bc	0.25	135	4.1×3.1	0.3×0.2	106	102	0.2
1343	SAB(s)b	0.25	60	8.8×6.6	1.2×0.9	80	82	6.8
1530	SB(rs)b	0.35	25	6.8×4.9	1.2×0.8	8	122	3.8
4303	SAB(rs)bc	0.14	88	3.3×2.8	0.2×0.2	-	-	1.4
4314	SB(rs)a	0.10	135	6.6×5.9	0.3×0.3	-	-	0.1
4321	SAB(s)bc	0.12	170	8.8×7.0	0.7×0.6	30	153	-
5248	(R)SB(rs)bc	0.3	115	6.6×4.6	0.7×0.5	110	137	4.2
5728	(R1)SAB(r)a	0.4	125	5.3×3.2	1.1×0.6	-	33	4.0
5905	SB(r)b	0.2	141	1.6×1.5	0.3×0.3	135	25	2.6
5945	SB(rs)ab	0.1	105	3.5×3.2	1.2×1.1	105	10	4.4
5953	SAa	0.1	192	6.1×5.5	1.0×0.9	169	no bar	9.9
6503	SA(s)cd	0.65	121	38.5×13.4	1.1×0.4	123	no bar	1.5
6951	SAB(rs)bc	0.2	146	4.6×3.7	0.5×0.4	170	85	1.4
7217	(R)SA(r)ab	0.20	89	11×8.8	0.8×0.7	95	no bar	0.6
IC1438	SAB(r)a	0.10	130	3.3×3.0	0.5×0.5	-	124	1.3
7469	SAB(rs)a	0.09	38	1.6×1.5	0.5×0.5	135	56	-
7570	SBa	0.05	135	4.4×4.2	1.3×1.3	30	75	1.4
7716	SAB(r)b	0.2	30	6.3×4.2	1.0×0.7	35	34	3.2
7742	SA(r)b	0.05	133	9.9×9.4	1.0×1.0	-	no bar	4.3

Table 3.1: Morphological characteristics of the galaxies in the observed sample. Galaxies are listed in order of increasing RA (Col. 1); morphological type as stated in the RC3 (Col. 2); ellipticity of the nuclear ring as derived by using the IRAF ELLIPSE task (Col. 3); PA of the ring major axis, calculated counterclockwise from North to East (ELLIPSE; Col. 4); ring radius in arcseconds (Col. 5) and kpc (Col. 6); PA of the galactic disk from RC3 (Col. 7), except for NGC 1530 (Regan et al. 1996) which is based on kinematical data; PA of the bar major axis, except for NGC 1530 (Regan et al. 1996) and NGC 7469 (Davies, Tacconi, & Genzel 2004) which are based on kinematical data (Col. 8); and the ring SFR (Col. 9) is derived from the total ring luminosity using the Kennicutt (1998) $H\alpha$ -SFR relation.

obtained using the IRAF package PHOT. This photometry package calculates the magnitude, among other parameters, based on user-defined values for the radius and annulus of a sky aperture. To convert from instrumental magnitude to AB magnitude for the spectrophotometric standard stars, an interpolation method was used based on results from Oke (1990). Oke defines values of AB at points where no ambiguity exists for instrument calibration problems due to spectral resolution. Therefore, to obtain magnitudes for the filters used in our survey, magnitudes with respect to the wavelengths just above and below the interested filter wavelength were chosen. Interpolating between these values yields the absolute magnitude for the five H α filters. The resulting integrated fluxes of the rings (on the order of $10^{-12} - 10^{-14}$ erg s $^{-1}$ cm $^{-2}$) and luminosities of the H II regions (on the order of $10^{38} - 10^{40}$ erg s $^{-1}$; see Appendix A) are consistent with published data (e.g., Pogge 1989; Storchi-Bergmann, Wilson, & Baldwin 1996; Regan et al. 1996; Sheth et al. 2000).

3.3 Ring Morphology

We fitted the nuclear rings of the 22 galaxies with the IRAF task ELLIPSE. We obtained the central position of each ring from the peak in the *I*-band image, and fixed the center while iteratively fitting elliptical isophotes to the H α image. We masked out the nucleus and foreground stars that could affect the fitting process, and provided initial estimates of the major axis length, ellipticity, and PA. The task produced measurements of the azimuthally integrated intensity, observed ellipticity,

and PA of the ring major axis as a function of radius. We determined the best-fitting ellipse, which corresponded to the peak isophotal intensity across the radial range of the ring (see Table 1). Figure 3.1 shows the resulting fits of the 22 rings, overlaid on the H α images. The pixel-based ring diameters produced from ELLIPSE were converted to arcseconds and kiloparsecs (see Table 1, Columns 5 & 6, respectively). The rings vary in major axis from 0.2 kpc to 1.7 kpc, which is typical for nuclear rings (Buta & Crocker 1993). In most cases, the galaxy distance was obtained from the Nearby Galaxies Catalog (Tully 1988); in the cases where there were no catalog values recorded, we computed them by dividing the recessional velocity by the Hubble constant (taken at $75 \text{ km s}^{-1} \text{ Mpc}^{-1}$) – see Paper I for details. Table 1 lists the parameters of the isophote best representing each ring, chosen on the basis of the peak isophotal intensity across the radial range of the ring.

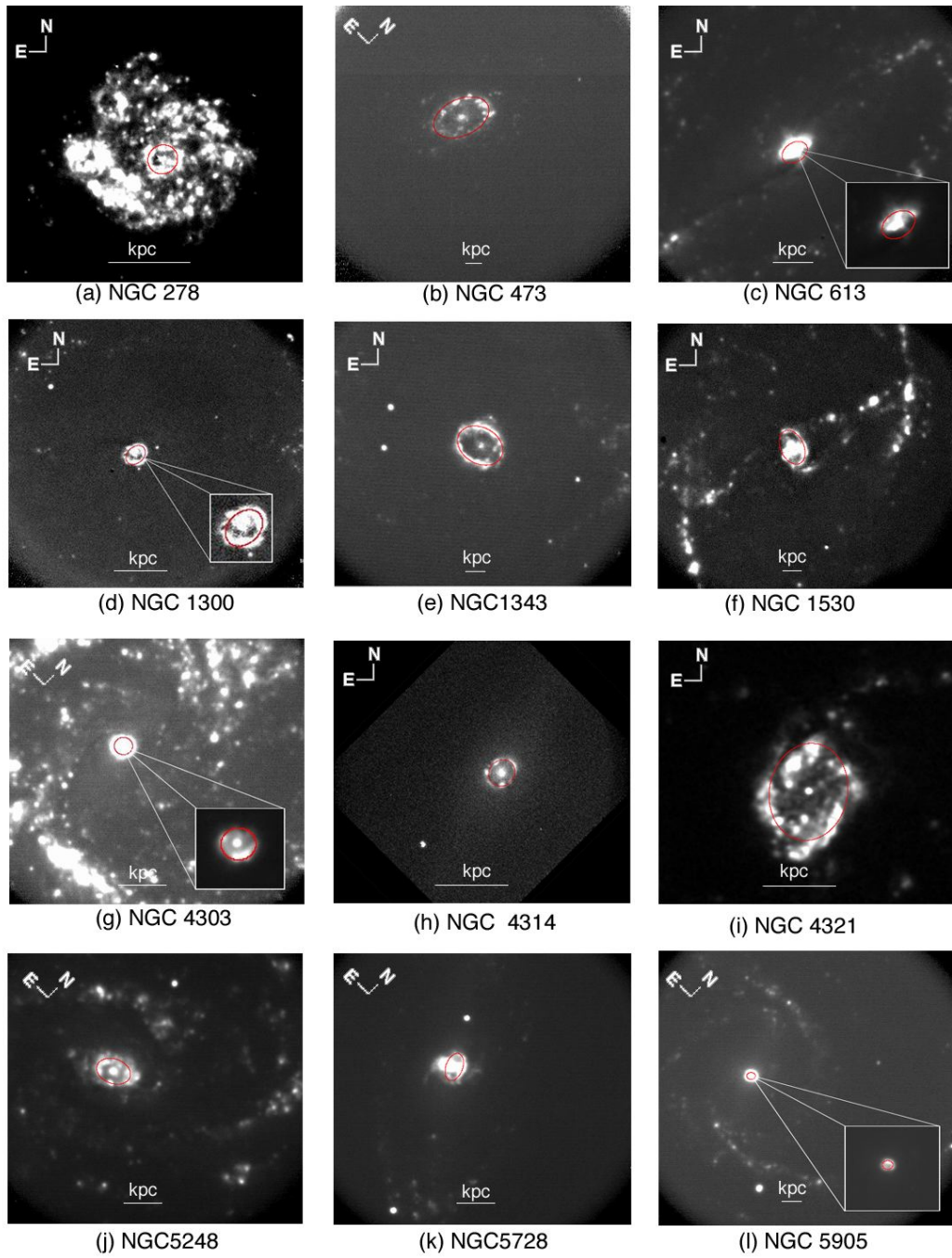


Figure 3.1: panels a. - l.: Ellipse fits for the nuclear rings in the sample galaxies produced by the IRAF task ELLIPSE, overlaid on the $H\alpha$ images. The major axis lengths were optimized based on the maximum intensity along a given contour as computed using ELLIPSE (see Section 3.3).

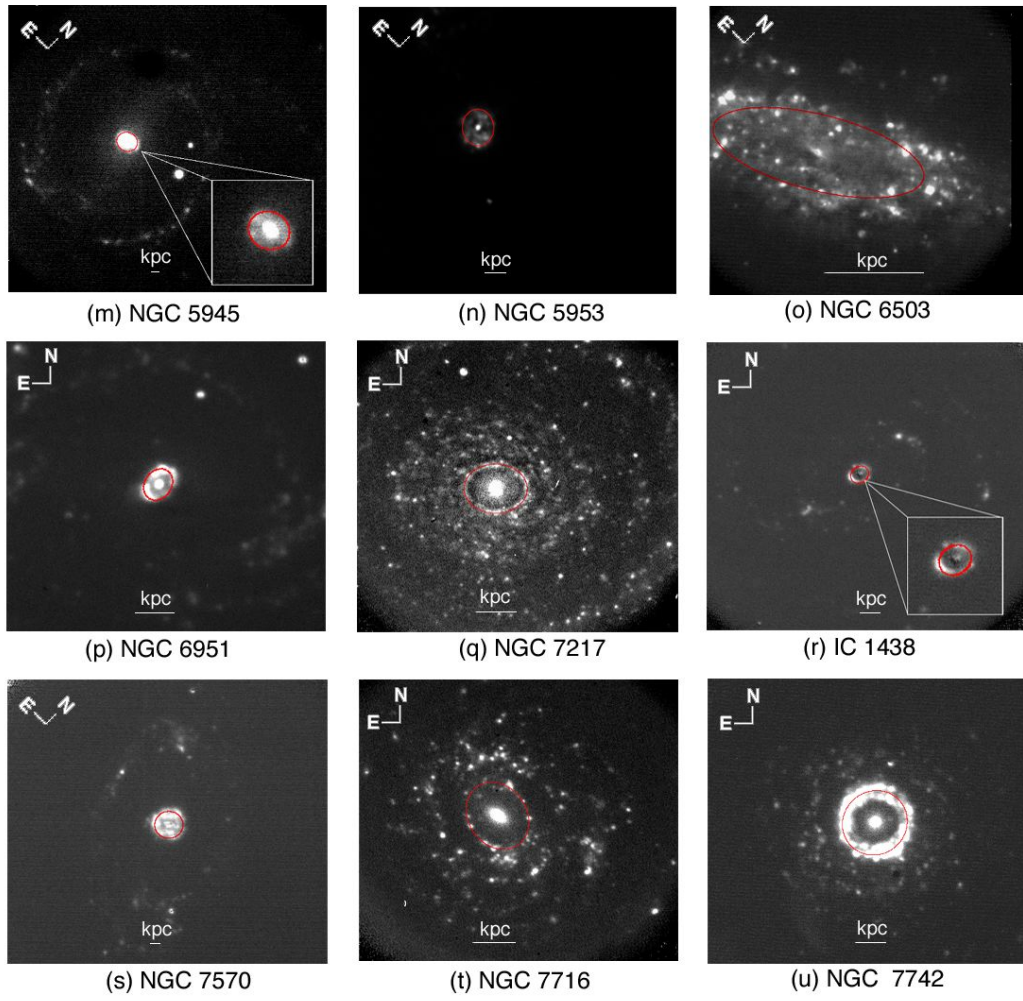


Figure 3.1: continued: panels m. - v.

We compare the ellipticity and PA of each ring to that of its host disk. Disk ellipticities and PAs are from the RC3, with the exception of the values for NGC 1530, which are based on the kinematical data of Regan et al. (1996). Figure 3.2 compares the PAs and ellipticities of the rings to their host disks. The plots show a clear linear relationship between the ring and its host disk with respect to both PA and ellipticity. This indicates that the rings are in the same plane as the disk and are nearly circular when deprojected. In some cases (NGC 278, NGC 4303, NGC 4314, IC 1438, and NGC 7742) the disk is nearly circular; those galaxies are seen face-on and do not appear in Figure 3.2. The disk morphology in these cases is consistent with that of the rings, which all have very low ellipticities (less than 0.1). The only exception to this general statement is NGC 7570 whose ring PA and ellipticity differ significantly from those of the disk. The ring appears to be nearly face-on so the PA of the chosen isophotal fit may not be reliable. However, the disk high inclination ($i=54^\circ$; RC3) is not consistent with the observed nearly circular ring. This strongly suggests that the ring is not in the same plane as the disk.

3.4 Equivalent Widths of HII Regions in Nuclear Rings

3.4.1 Identification of HII Regions

To identify the individual H II regions forming a given ring, we used the program SExtractor (Bertin & Arnouts 1996), which builds a catalog of H II regions and their associated fluxes from an astronomical image. The various parameters used allow for the detection of H II regions even at very low H α intensities. We

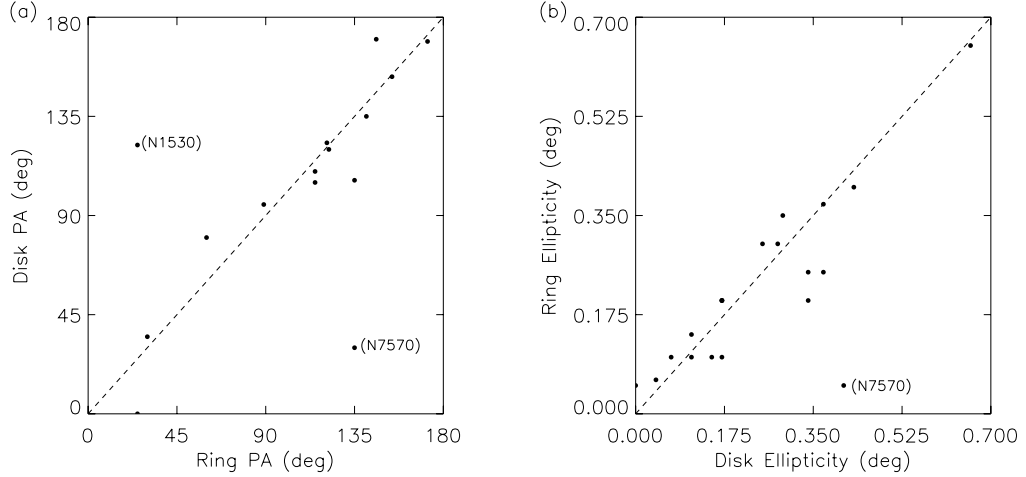


Figure 3.2: (a) PA of the disk versus the ring major axis for those rings whose ellipticity is greater than or equal to 0.1. (b) Ellipticity comparison between the ring and the galactic disk. Both plots show a linear relationship between the ring and host galaxy PA and ellipticity, and indicate that the rings are in the same plane as the disk and are nearly circular.

masked out the nucleus and extraneous stars that were clearly not part of the ring. The catalog file produced by the program records the position, area, and flux of each H II region detected. Figure 3.3 shows the outlines of the fitted H II regions overlaid on the continuum subtracted H α images. In the case of NGC 7469, SExtractor was unable to identify any H II regions due to poor spatial resolution compared to the small angular size of the ring. This galaxy is well known to contain a nuclear ring of 0''.5 in radius (Genzel et al. 1995; Davies, Tacconi, & Genzel 2004; Díaz-Santos et al., submitted to ApJ), which is consistent with our ELLIPSE results (Section 3.3). The lack of sufficient spatial resolution in our images, however, prevents us from continuing with the analysis of the individual H II regions in the ring, but we refer to above citations for a detailed study of its SF properties, based on high-resolution imaging and near-IR spectroscopy.

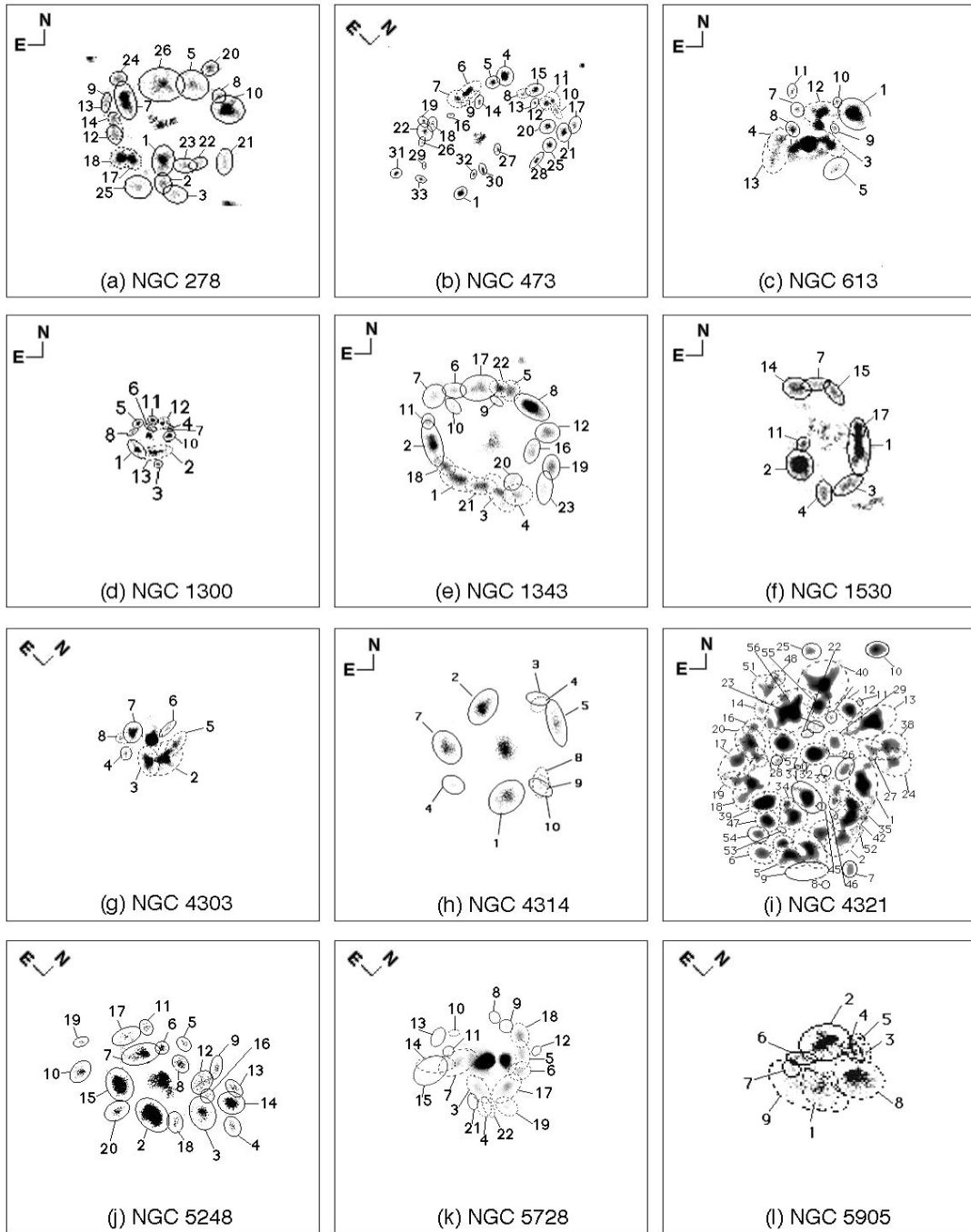


Figure 3.3: panels a. - l.: Results from SEXTRACTOR. Each H II region identified is fitted using a Kron ellipse, which calculates the total magnitude of the extended H II region. In the cases where the H α boundaries are merged from one or more sources, the program deblends the regions and indicates these fittings with a dashed ellipse. SEXTRACTOR could not identify any H II regions for NGC 7469 due to poor spatial resolution.

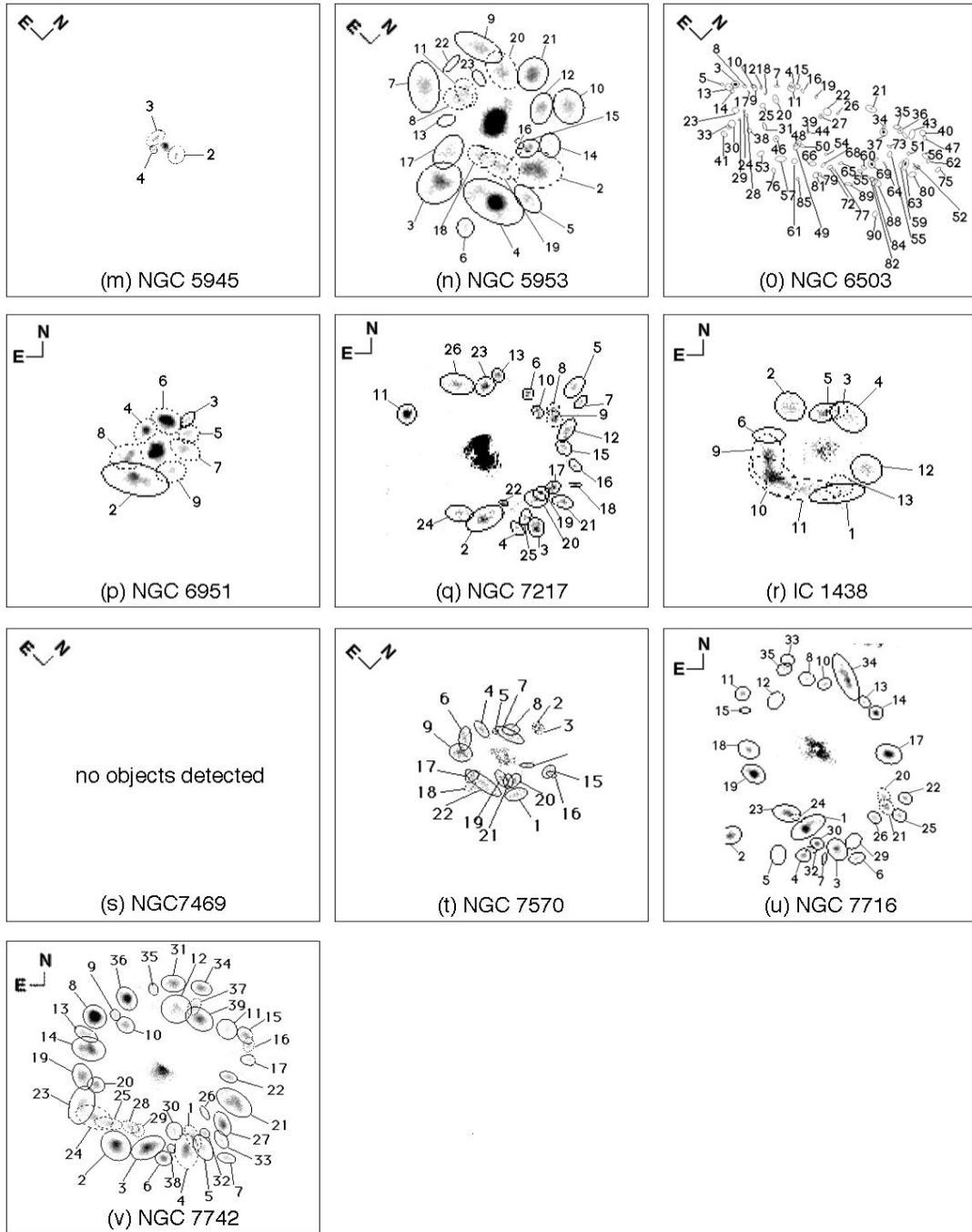


Figure 3.3: Continued

To obtain EWs of the H II regions, we measure fluxes in both the I -band and H α . We do this by first imposing the position and shape of the apertures from the SExtractor analysis of the H α image onto the I -band image, making use of the fact that these images have already been registered (see Paper I). We then run SExtractor in its two-image mode to obtain the corresponding I -band fluxes. Among the many parameters to be defined in SExtractor, two are of particular importance, namely the initial box size for the H II region detections, and the threshold value used to determine the extent of an individual H II region. For the first parameter we chose a value corresponding to the average seeing value in our images, namely 8 pixels or 0".9. For the threshold value, we chose twice the standard deviation, σ , of the combined galaxy and sky background across the whole image.

We confirmed our parameter settings by independently varying the threshold value and box size and comparing the resulting ring morphology and EWs to our "reference" values. Several test cases were run by altering each parameter (fixing one parameter while modifying the other) by $\pm 50\%$ of the reference values. Figure 3.4 shows the resulting images for NGC 1343, as a representative example. Figures 4a and 4b are the result of fixing the threshold and altering the box size. Modifying the box size by $\pm 50\%$ of the reference value (8×8 pixel box) to a 12×12 box and 4×4 box, respectively, causes a significant change in the visual appearance of the H II regions. Increasing the box size results in an obvious over-blending of the H II regions, with the opposite occurring when decreasing the box size. Figures 4c and 4d of Figure 3.4 are the products of modifying the threshold by $\pm 50\%$ of the reference value (2σ), to 1.33σ and 3σ , respectively. Changing the threshold in

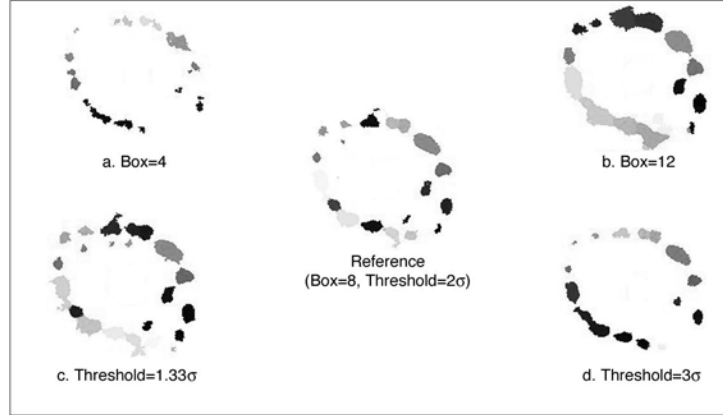


Figure 3.4: Change in ring morphology for NGC 1343 based on variation of the background box size and detection threshold value. Top row shows the resolved H II regions based on fixing the threshold at 2σ and varying the box size - a) box size = 4×4 pixels with 31 H II region detections; b) box size = 12×12 pixels with 20 detections. The center image is the reference image: box size = 8×8 pixels with 25 detections. Bottom row shows the images based on fixing the box size at 8×8 pixels and varying the threshold value - c) threshold = 1.33σ with 30 detections; d) threshold = 3σ with 19 detections. The grayscale is *not* representative of the ages of the regions, but rather the order in which SExtractor identified the regions.

either direction causes a significant change in the number of H II region detections forming the ring. Overall, the isophotal detection area is more sensitive to the box size, while the number of detections is more sensitive to the threshold. These parameters are important since the background to be subtracted from the I -band and $H\alpha$ data is locally defined by SExtractor for each H II region, and includes both the sky background and the emission from the galactic disk. In general, this empirical analysis gives us confidence that our parameter choices do indeed best represent the H II region morphologies.

3.4.2 Equivalent Widths

To obtain EWs for the individual H II regions, the H α flux was divided by the *I*-band flux within the same aperture as defined by SExtractor. We describe below some of the intricacies of the EW determination. We specifically discuss the correction of those cases where the *I*-band flux of an H II region is particularly low, as well as the error budget of the EW values.

Negative *I*-band Fluxes

Many of the galaxies in our sample (16 out of 20) contained H II regions whose *I*-band emission was lower than the background due to noise. This resulted in negative *I*-band fluxes, which are unphysical and cannot be used to determine the EW. Rather than changing either the H II region aperture or specific SExtractor parameters, we chose to use a physically meaningful upper limit to the *I*-band flux. We did this by taking, for all galaxies, the lowest *I*-band flux per pixel (f_{\min}) of all of the H II regions. We assume the lowest value to be representative of a 6σ deviation from the mean. Where f_{\min} is negative, we correct any *I*-band flux per pixel lower than the value $f_{\text{corr}} = \frac{1}{2}|f_{\min}|$ (equivalent to a 3σ adjustment) to have a corrected H II region flux $F_{\text{corr}} = f_{\text{corr}} \times \text{area}$. This method, thus, applies a correction to those H II regions whose emission is positive but very low. See Appendix A for details on individual H II region corrections.

To estimate the impact of the 3σ corrections on the EWs, we also corrected these fluxes to a lower level, namely $\frac{1}{3}|f_{\min}|$ (equivalent to a 2σ adjustment). The

maximum impact on EW that we found in such cases was an increase in EW of order 0.2 in $\log(\text{EW})$, although in many cases the difference was less than 0.1. In 10 out of the 16 galaxies affected by negative I -band emission, 5%, on average, of the H II regions subject to the 3σ correction would not be subject to a 2σ correction. That is, those H II regions with very low positive I -band emission that were changed using the 3σ discriminator were no longer affected when compared to the 2σ value. The other six galaxies were entirely unaffected by the correction change and can therefore be considered more reliable. We present these findings in Figure 3.5 using a 3σ correction. Regions whose I -band flux was changed to the 3σ value but was unaffected by the 2σ comparison are labeled as a diamond with a cross; these represent lower-limits in the $\log(\text{EW})$ since we find that these values would have increased if we had chosen a 2σ correction. All other H II regions with corrected I -band fluxes, including the ones that were negative, are labeled as open diamonds. Those H II regions where no corrections were needed are labeled as filled diamonds, and we consider those the most reliable.

Characterizing the Uncertainties

We estimate typical uncertainties in the EW values by considering uncertainties due to background subtraction and H II region detection, which both result from the application of SExtractor. Additional contributions to the overall error budget will come from measurement errors in the standard stars, the calibration uncertainties associated with our method of continuum subtraction (see Paper I), and

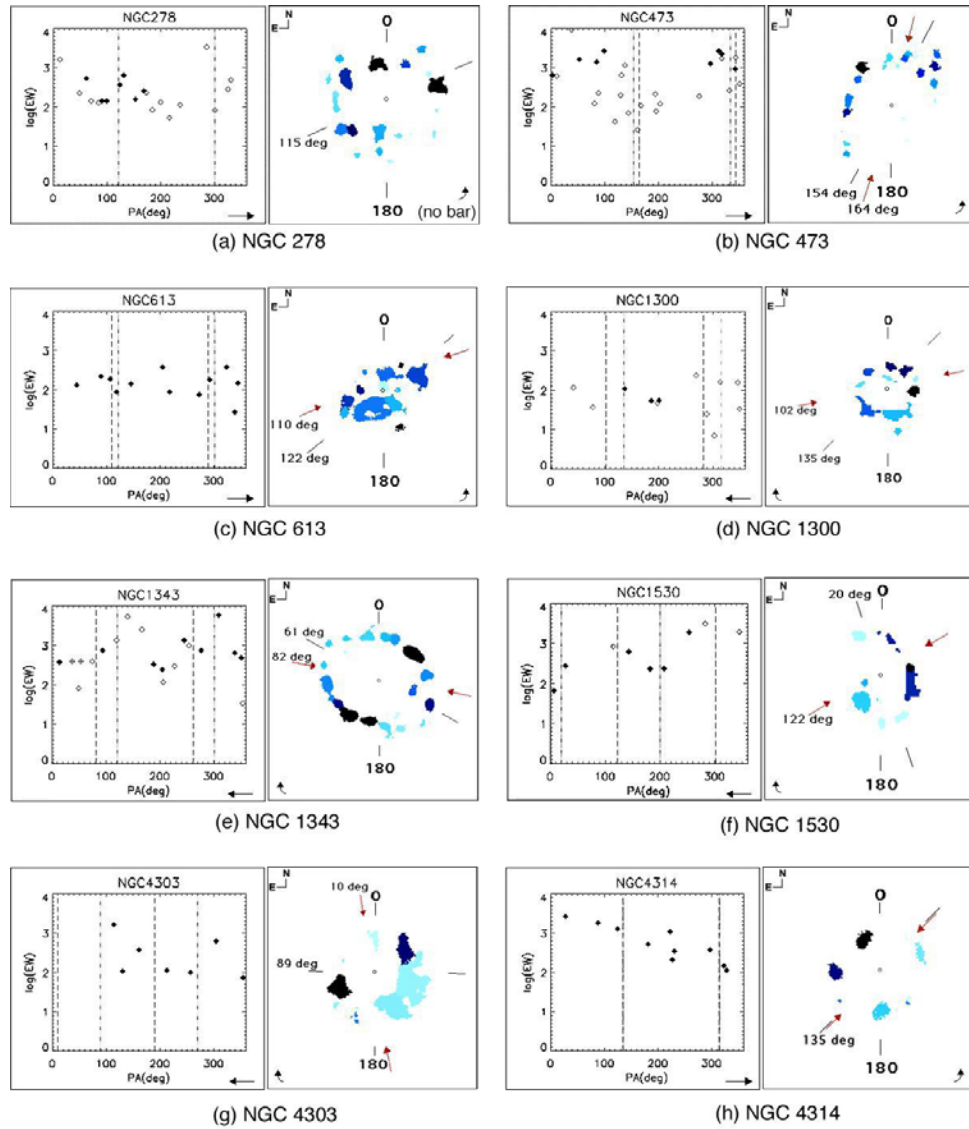


Figure 3.5: Age distribution – a. through h. The left panels plot the PA of each H II region vs. their EW. Solid diamonds represent those EWs whose I -band fluxes were not affected by the background 3σ noise; open diamonds indicate EW where I -band fluxes needed to be increased to compensate for the dominant background noise; open diamonds with crosses show those H II regions that would not have needed their flux modified if using a 2σ constraint. The right panels picturize the rings with their identified H II regions. Age decreases as the shade of color changes from light to dark. Arrows are drawn to indicate the PA of the bar major axis, as well as the rotational direction of flow in the ring, if applicable. The ring major axis is indicated by two dashed lines. All rings have been rotated to a typical North-East configuration. See Section 3.6.1 for details. NGC 4321 is based on $H\beta$ analysis from Allard et al. (2006).

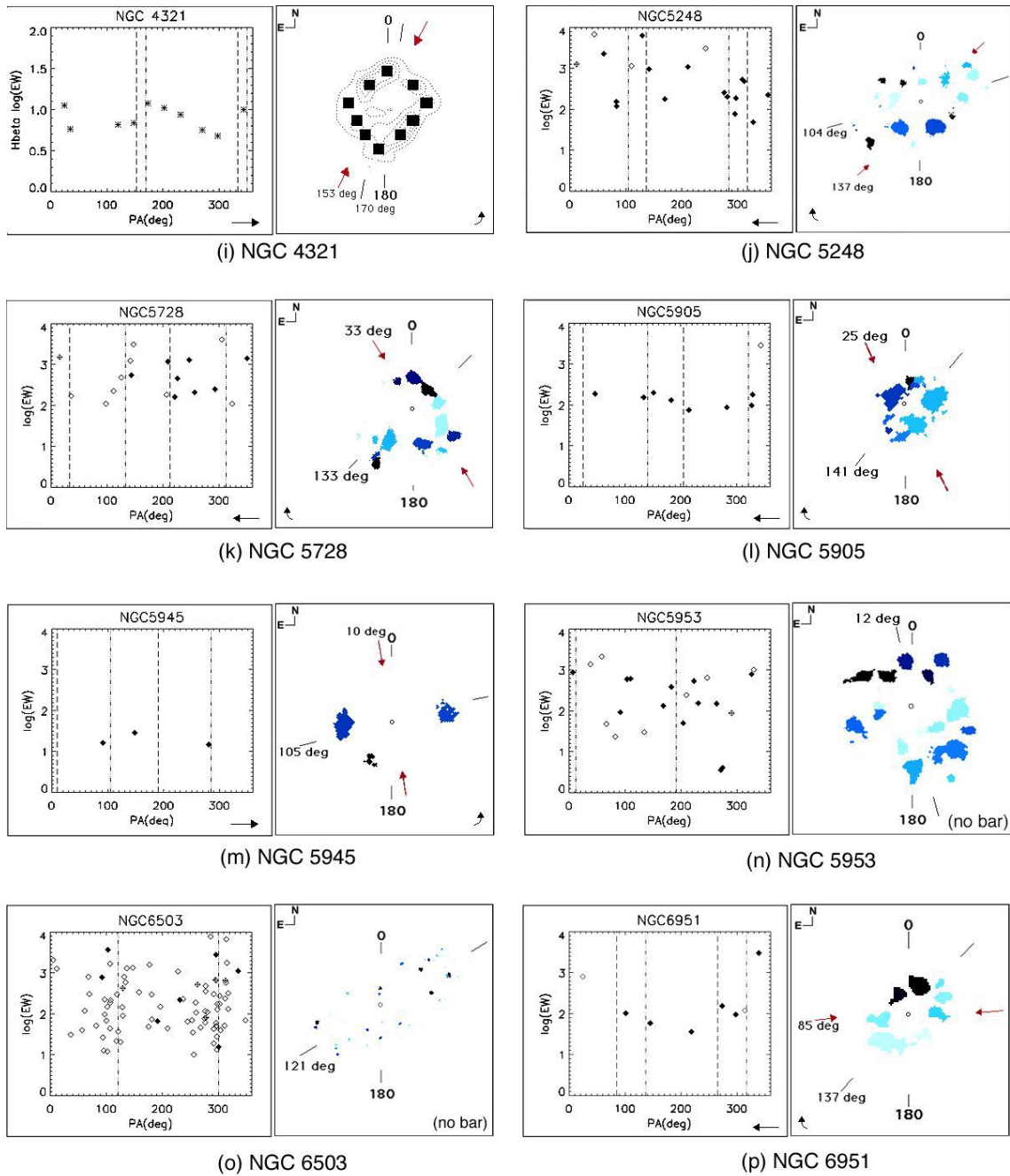


Figure 3.5: Continued

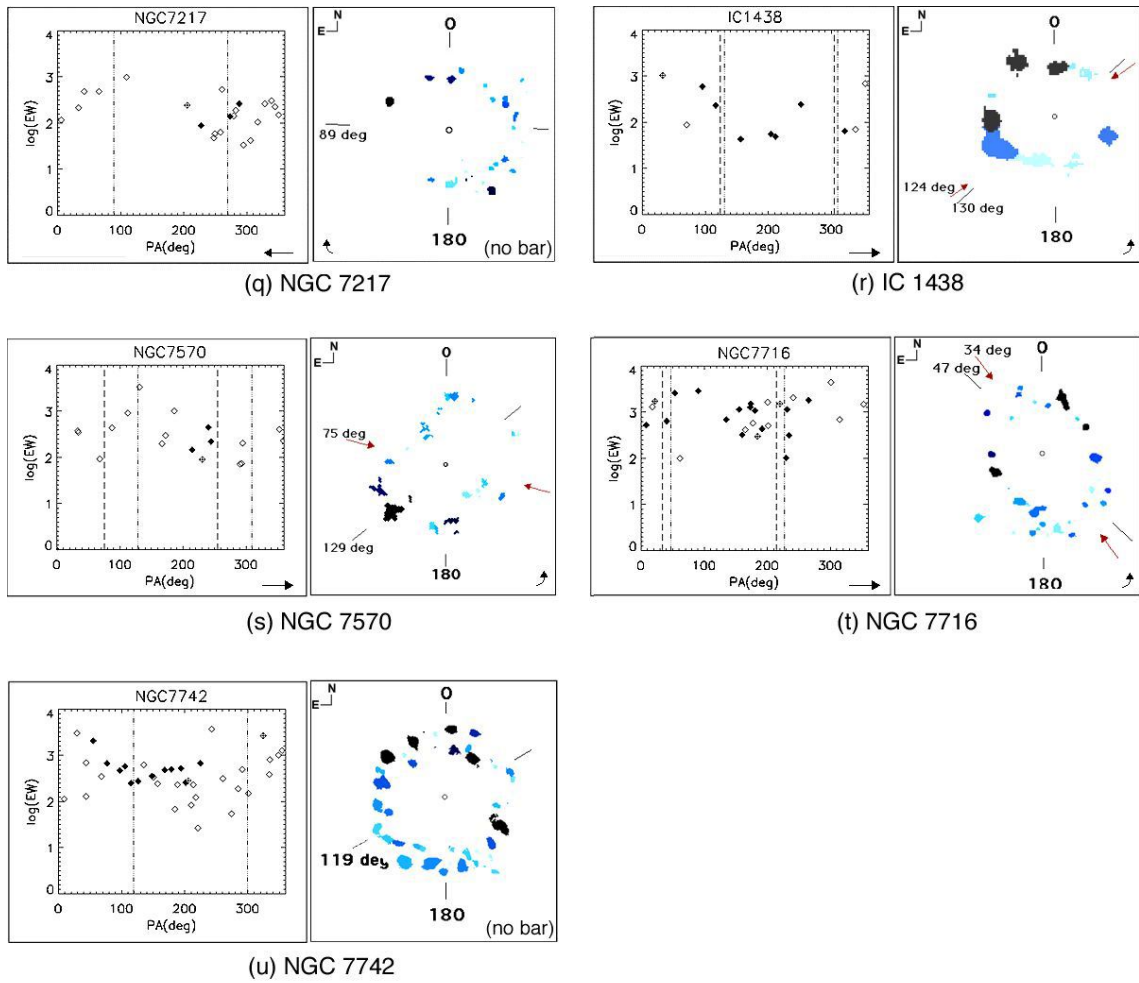


Figure 3.5: Continued

in the filter response curves, but we will assume that they are negligible compared to the two main contributors.

To make a conservative estimate of the uncertainty in the background subtraction we consider the I -band backgrounds. These will be more affected than the $H\alpha$ measurements because (1) the background is higher in I than in $H\alpha$, (2) the contrast between the H II region and background is much smaller than in $H\alpha$, and (3) the basic morphology of an H II region has been set by its $H\alpha$ appearance in the I -band. From our analysis of the negative residual I -band fluxes, we know that the maximum difference in the log of the EW between the two cases (i.e., applying a 2σ versus 3σ correction to the affected measurements) is 0.2. Such a difference of $\log(\text{EW})=0.2$ corresponds to a factor of 1.5 difference in the I -background subtracted before measuring the flux of an H II region, where $\log(\text{EW})=0.1$ would correspond to a factor of 1.3. Even considering the small field of view of our I -band images, these factors cover the uncertainty in the determination of the background.

The other main contributor of the EW uncertainties is in the flux measurement of the H II regions. An RMS value, based on Gaussian noise statistics, is associated with each detection. On average, we estimate the RMS to be 5% of the detection, which equates to 0.02 in the log of the EW.

We thus arrive at a conservative error budget consisting of two components, 0.2 and 0.02 in the $\log(\text{EW})$. These combine in a worst case scenario to a factor of 1.6, or an error budget in $\log(\text{EW})$ of 0.2. We take 3σ of the total error budget as a guideline for discriminating between EWs (and thus H II regions). As a consequence, two EW values must be 0.6 apart in the log to make them significantly different.

Whereas this is by all means a large uncertainty, Figure 3.5 shows that the values can range by as much as 3 in the log for a given ring during the evolution of massive stars that, in fact, most of our measurements lead to straightforward and believable conclusions on at least relative ages, as discussed in Section 3.6.1. We stress that the error budget determined here is a very conservative one, and that for most H II regions the actual uncertainty will typically be significantly smaller.

3.5 Age Dating

We use Starburst99 (Leitherer et al. 1999) stellar population modeling to estimate the age of the individual H II regions. The models present the time evolution of the $EW(H\alpha)$ for varying initial starburst rates, IMFs, and metallicities, all of which will affect the evolution of the population. Figure 3.6 shows the time evolution of $EW(H\alpha)$ for both an instantaneous starburst (i.e., all stars are formed simultaneously in an instantaneous starburst episode) and a continuous starburst (i.e., the star formation rate is constant in time). While the starburst choice can greatly affect the determination of the ages of the population greater than ~ 5 Myr, it is not clear which model best represents the stellar activity in nuclear rings. Since active massive star formation is prevalent in H II regions, adopting an instantaneous burst would seem to fit the model predictions of younger ages better over the range of 1 Myr - 10 Myr. If, on the other hand, there is an abundant supply of gas entering the ring, starbursts may be a composite of episodic bursts (Elmegreen 1997; Allard et al. 2006). Star formation in the ring would cyclically enter an active starburst

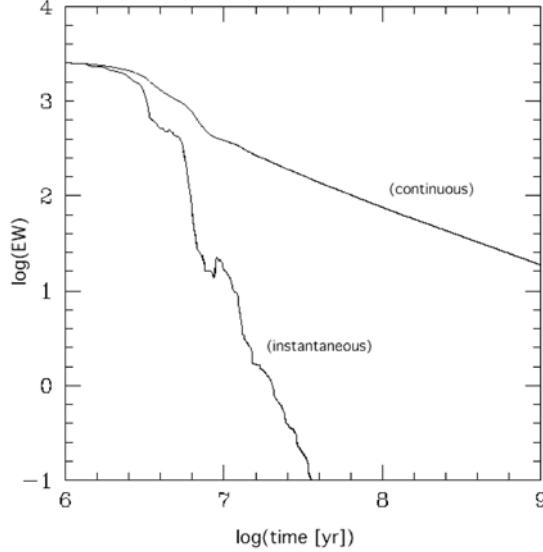


Figure 3.6: H α EW vs. time following Leitherer et al. (1999; Starburst99 curves) for an instantaneous and a continuous burst of star formation with a Salpeter IMF between $M_{low} = 1 M_{\odot}$ and $M_{up} = 100 M_{\odot}$. A solar metallicity of $Z = 0.02$ is used.

period until it exhausts the surrounding gas supply, and then cease star formation until enough gas sparks a new starburst period.

Figure 3.7 shows Starburst99 model curves for an instantaneous and a continuous starburst with different IMF slopes, mass cut-offs, and metallicities. We vary the IMFs in both scenarios and find that the evolution model is not very sensitive to the upper limit masses (i.e., $30 M_{\odot}$ and $100 M_{\odot}$) or the IMF slopes ($\alpha = 2.35, 3.3$), especially in the instantaneous starburst case. The models also confirm that high metallicity H II regions show lower EW(H α) while low metallicity regions have invariably high EW(H α). Regardless of the metallicity or type of burst, however, we find that all of the predicted evolution curves show a significant monotonic drop of EW with increasing age. Since we are more interested in the relative age difference from one H II region to the next, the sharply declining curve (in either starburst

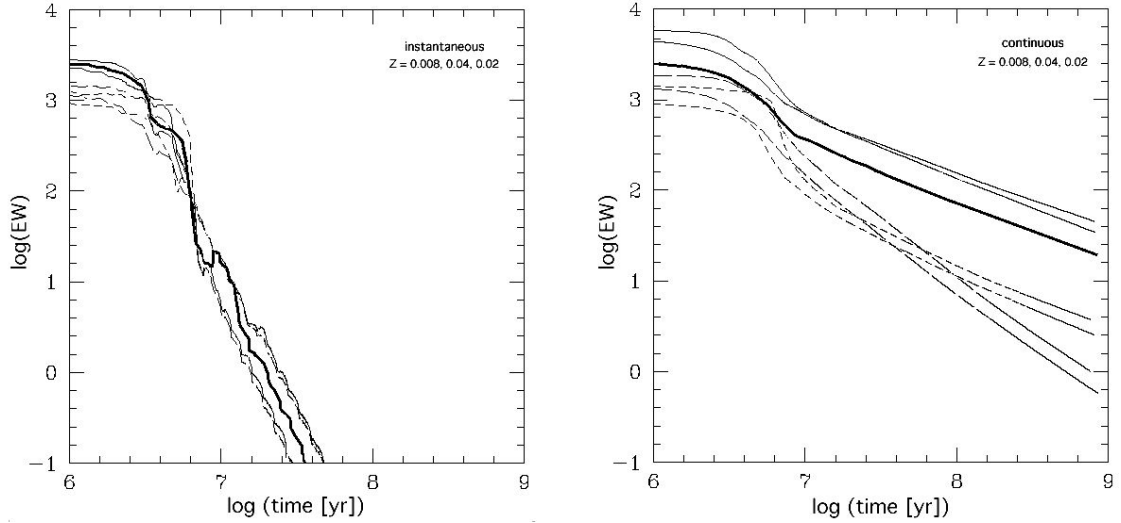


Figure 3.7: H α EW vs. time following Leitherer et al. (1999; Starburst99 curves) for an instantaneous burst of star formation (left panel) and continuous burst (right panel) for varying IMF slopes, upper limit masses, and metallicities. The thick solid line represents the model prediction we adopted for IMF between $M_{low} = 1 M_{\odot}$ and $M_{up} = 100 M_{\odot}$, IMF slope = 2.35, and $Z = 0.02$. Long dashed lines represent a slope of 3.3 and $M_{up} = 100 M_{\odot}$ for $Z=0.04$ and $Z=0.008$. Short dashed lines represent a slope of 2.35 and $M_{up} = 30 M_{\odot}$ for $Z=0.04$ and $Z=0.008$.

case) allows for an unambiguous discussions of age gradients. We adopted an instantaneous stellar starburst with a Salpeter (1955) IMF between $M_{low} = 1 M_{\odot}$ and $M_{up} = 100 M_{\odot}$, and a solar metallicity, which is a good predictor for circumnuclear regions of barred galaxies (Allard et al. 2006).

3.6 Discussion

3.6.1 Age Distribution

The results from SEXTRACTOR were used to map the ages of each H II region according to their azimuthal location in the ring. The right panels of Figure 3.5 show the resolved H II regions, which are color-coded according to age, in terms of EW.

We assigned the physical center of the ring (as computed with ELLIPSE) to be (0,0), and viewed an H II region’s azimuthal position in a counter-clockwise rotation from North to East. The color ranges are unique to each ring and, thus, do not denote the same EWs for all rings. Although we did not deproject the rings, all H II regions have a unique position, which allows us to search for any unambiguous distribution patterns. The PA of the major axes of the ring and the bar are indicated in the image. To complement the images, plots are shown in the left panels, which graph the $\log(\text{EW})$ versus PA, and again indicate the PAs of the ring and bar major axes.

We use $B - I$ color index maps as morphological indicators of the ring kinematics. These maps provide direct tracers of the bar dust lanes, which show the flow of gas to the ring. In the cases where the dust lanes were present, the azimuthal direction of the ring rotation was consistent with that of the galaxy in all cases. The contact points of the dust lanes with the ring are clearly visible in most of our images and indicate an offset of $\sim 90^\circ$ between the contact points and the bar (see Section 3.6.3 for details). The dust lanes also show directional flow around the ring, assuming that rotation continues in the same direction as seen with the bar dust lanes and spiral arms. The adopted rotational direction of the rings is listed in Table 3.2 and indicated for each ring containing a bar in Figure 3.5.

We find that several galaxies, both barred and non-barred, exhibit relative azimuthal age gradients within the ring, as also observed by Ryder, Knapen, & Takamiya (2001) and Allard et al. (2006) for NGC 4321. We only consider age gradients over a significant portion of the ring (greater than 25% of the ring) with amplitudes that exceed the uncertainties for differentiating between points over the

NGC	CP #1	H II region #1	CP #2	H II region #2	Rotation	Δ PA #1	Δ PA#2
	($^{\circ}$)	($^{\circ}$)	($^{\circ}$)	($^{\circ}$)		($^{\circ}$)	($^{\circ}$)
(1)	(2)	(3)	(4)	(5)	(6)	(7)	(8)
473	254	312	74	38	ccw	58	36
613	200	205	20	323	ccw	5	57
1300	12	345	192	269	cw	27	77
1343	172	140	352	309	ccw	32	43
1530	32	344	212	282	cw	48	70
4303	280	304	100	114	cw	24	14
4314	45	27	225	222	cw	18	3
5248	47	43	227	243	cw	4	16
5728	303	305	123	147	cw	2	24
5905	295	343	115	151	cw	48	36
5945	100	148	280	280	ccw	48	0
6951	355	339	175	100	cw	16	75
IC1438	214	251	34	32	ccw	37	2
7570	345	353	165	131	cw	8	34
7716	124	91	304	301	ccw	33	3

Table 3.2: Comparison of the location (i.e., PA) of the contact points (CP) to that of the youngest H II region in each hemisphere, as bisected from the bar. The PAs of each contact point are given in Col. 2 and 4; the location of the youngest H II region in each hemisphere is given in Col. 3 and 5 with the ring rotational direction cited in Col 6, as observed in the $B - I$ images; Col. 7 and 8 indicate the difference in location between the contact points and the respective H II region. In most cases the separation is small, which is consistent with the notion that the youngest H II region (in its respective hemisphere) should be near the location of the contact points.

range of interest. We highlight the age gradient cases here and comment on the rest of the sample in Appendix B. We summarize the characterization of the age distributions for all of the rings (e.g., azimuthal gradient, radial gradient, flat distribution, or no recognizable pattern) in Table 3.3 (Column 2).

- NGC 278 (Fig. 3.5a): The entire ring as seen in $H\alpha$ is very small in size (0.2 kpc in radius) with 20 individual H II regions detected that comprise the ring. This ring is the smallest one recognized in the galaxy; a second nuclear ring appears at ~ 1 kpc and is discussed in detail in Knapen et al. (2004). The host galaxy does not contain a bar in the optical nor near-IR wavelengths (Knapen et al. 2004). There is a decrease in the $\log(EW)$ (i.e., an increase in age) over approximately one third of the ring ranging from the positions of the H II regions centered at azimuth 124° to 236° . This indicates a counterclockwise rotation within the ring. A radial gradient spans the same range, with the younger H II regions lying on the inner side of the ring. A similar pattern, although not as clearly defined, appears over the range of 12° to 100° .
- NGC 473 (Fig. 3.5b): Two-thirds of the ring can be seen in the $H\alpha$ image, defined by 27 H II regions. A galactic bar exists at a major axis PA of 164° along the major axis. The bar dust lanes indicate a counterclockwise flow of material around the ring. There is a sharply sloped age gradient over the range of 38° to 203° from younger to older, respectively.
- NGC 1343 (Fig. 3.5e): The ring in this barred spiral galaxy is seen as complete in $H\alpha$ with 20 resolved H II regions. The mapping of EW to H II region location

indicates a clear bi-polar age pattern around the ring with maxima at PA = 140 and 309°. There is a distinct age gradient approximately from one contact point to the other contact point (located at 172° and 352°, respectively), where the age decreases counterclockwise from the bar contact points.

- NGC 1530 (Fig. 3.5f): Three-quarters of the ring can be seen in H α containing 9 distinct H II regions. The galaxy has a large bar at PA = 122° and two open spiral arms originating from its ends, rotating clockwise. We find bipolar age gradients, one in each hemisphere, as bisected by the position of the bar. The youngest H II regions are near the bar PA, (i.e., not the contact points) over the range of 283° to 207° and 115° to 7°, with the ring rotation also clockwise. Half of the ring is distinctly younger than the other half, where the turnover points coincide with the ring major axis PA (= 25°).
- NGC 4314 (Fig. 3.5h): The small ring consists of 10 H II regions showing a smooth and well-defined age gradient. The age gradient flows from older to younger in the same direction as the presumed ring rotation (clockwise). The youngest H II region is within 20° of one of the contact points (PA = 45°).
- NGC 4321 (Figure 3.3.5i): The well resolved full ring contains 57 detected H II regions. Because missing data prevent the calculation of H α equivalent widths and ages, we refer to Allard et al. (2006) for a similar analysis in H β . They find a bipolar age gradient corresponding to the ring PA (at 170° and 350°) and the location of the youngest H II region in each hemisphere. The age increases in a counter-clockwise direction along the direction of flow.

- NGC 5728 (Fig. 3.5k): Eighteen H II regions define the partial ring, which is three-quarters complete. A very steep but small gradient exists from PA = 147° to PA = 98° from younger to older, according to the clockwise directional flow of the ring. One contact point (PA = 303°) is within 2° of the youngest H II region in the ring. The second youngest H II region (PA = 147°) is within 24° of the second contact point (PA = 123°), although it does precede that contact point.
- NGC 6951 (Fig. 3.5p): The ring is small but complete with eight detected H II regions. The youngest H II region (PA = 339°) is within 16° of its respective contact point. The ages steeply increase (by a factor of 10) from 339° to 218° in a clockwise direction, consistent with the directional flow of the galaxy.
- NGC 7217 (Fig. 3.5q): The ring is three-quarters complete in H α . Twenty-two H II regions were detected in the ring of this unbarred galaxy. Ages increase in a clockwise direction from PA = 109° to PA = 6° .
- IC 1438 (Fig. 3.5r): This barred galaxy hosts a complete ring with 11 H II regions detected. There exists an increasing age gradient from PA = 32° to PA = 211° in a counterclockwise direction. This direction is consistent with the ring rotational flow. The youngest H II region is within 2° of its respective bar contact point (PA = 304°)

- NGC 7570 (Fig. 3.5s): Eighteen H II regions comprise a mostly complete ring in this barred galaxy. An increasing age gradient ranges counterclockwise from PA = 112° to PA = 295°. There is also a radial gradient spanning the same range as the azimuthal gradient, with two distinct arcs at nearly identical slopes, and where the inner arc appears consistently older than the outer one. No correlation to the bar contact points is evident.

While many of the rings contain age gradients, a few show no gradient, namely NGC 613, NGC 5905, and NGC 5945. This type of distribution is qualitatively more consistent with Elmegreen’s (1994) predictions, which suggest that the massive star formation in the nuclear ring is shocked into existence due to gravitational instabilities in the nuclear region around the ILRs. Therefore, age gradients would not exist. Comparisons of EW to age for these three rings also indicate that these starbursts are relatively older than those seen in the other rings, on the order of 10 Myrs and higher. Elmegreen (1997) suggests that these rings (i.e., with no gradient) could last for as long as 100 Myrs before SF ceases if the inflowing gas rate is high enough. The SFRs of these three rings ($2M_{\odot}/\text{yr}$, $2M_{\odot}/\text{yr}$, and $4M_{\odot}/\text{yr}$, respectively; see Section 3.6.2 and Table 3.1 for SFR and inflow discussion) are among the higher values in our sample but are consistent with other rates documented (Regan et al. 1997; Jogee et al. 2002). If we take into account that NGC 613 and NGC 5945 are partial rings in the optical, then the SFRs calculated here are lower limits.

NGC	Age Distrib	V_{rot} (km s^{-1})	Ref	T (Myr)	CP time (Myr)	H II region #1 (Myr)	H II region #2 (Myr)
(1)	(2)	(3)	(4)	(5)	(6)	(7)	(8)
278	az.gradient	63	(a)	35	-	-	-
473	az. gradient	127	IFU	103	72	89	62
613	flat	115	(b)	23	13	13	9
1300	no pattern	135	(c)	17	0.6	16	4
1343	az. gradient	131	IFU	39	18	15	14
1530	az. gradient	185	IFU	50	4	48	14
4303	no pattern	97	IFU	9	6	8	7
4314	az. gradient	161	IFU	30	4	2	3
4321	n/a	170	(d)	32	-	-	-
5248	az. gradient	152	IFU	40	5	5	7
5728	az. gradient	180	(e)	47	45	40	43
5905	flat	150	(f)	15	11	14	14
5945	flat	150	(g)	62	17	25	17
5953	rad gradient	200	IFU	40	-	-	-
6503	no pattern	90	(h)	94	-	-	-
6951	az. gradient	160	(c)	24	24	23	19
7217	az. gradient	248	(i)	25	-	-	-
IC1438	az. gradient	204	(j)	19	11	13	11
7570	rad gradient	150	(g)	67	66	65	57
7716	no pattern	150	(g)	51	18	13	17
7742	no pattern	116	IFU	96	-	-	-

Table 3.3: Age distribution and H II region times. Col. 2 cites the age distribution, which fell into 4 categories: azimuthal gradient, radial gradient across the ring, flat, no pattern. For those rings with host bars, the period of the ring (Col. 5) is computed based on the rotational velocity at the ring radius (Col. 3) and the ring major axis radius (see Table 3.1, Col. 5); literature references for the rotational velocities are in Col. 4: a) Knapen et al. (2004); b) Blackman (1981); c) Knapen, Laine, & Relaño (1999); d) Knapen et al. (2000); e) Rubin (1980); f) Moiseev, Valdés, & Chavushyang (2004); g) no reference found- assumed a rotational velocity value of 150 km s^{-1} ; h) Bottema (1989) for H β line; i) Peterson et al. (1978); j) P. M. Treuthardt & R. J. Buta, private communication; 'IFU' refers to our WIYN IFU data (L. M. Mazuca et al. 2006). Travel times from the bar major axis PA to the contact points (Col 6) and to the youngest H II region in each hemisphere (Col. 7 and 8), when a bar exists.

3.6.2 Inflow and Star Formation Rates

In this Section we explore possible reasons for the result that only three galaxies show bi-polar age gradients around their rings, whereas many of the rings (9 of 22) show partial gradients along 25% - 30% of their rings, with the rest (10 of 22) showing no gradient.

We find no apparent relationships between the presence or absence of age gradients and the morphology of the rings or their host galaxies. For example, whereas NGC 4321, with its bi-polar age gradient, has a pair of well-defined dust lanes coming into the ring through the bar, NGC 1300 and NGC 5248 have similar dust lane morphologies yet show no gradients. Some of the poorly resolved rings, such as those in NGC 4303 or NGC 5945, do not show gradients, but given the presence of measured age gradients in the comparably small rings in NGC 6951 and IC 1438, the lack of spatial resolution in the former two cannot easily be used as an argument for the lack of a gradient. But even if we ignore galaxies with either small and badly resolved rings, or rings that do not have the classical aspect of dynamically-induced resonance rings (NGC 613 and NGC 6503 are in the latter category), we are left with a significant number of rings in which we should have detected gradients if present, but which for some reason do not show any. This category includes, for instance, NGC 1300, very similar to NGC 4314 or NGC 6951 which do show gradients (all compact well-defined rings with around a dozen H II regions, sitting in strong bars with well-defined sets of dust lanes); NGC 5248, similar to NGC 4321 (complex, rich rings with many H II regions organized into spiral arms

fragments and hosted by a relatively weak bar); NGC 7716, similar to NGC 7217 which does have a gradient; and NGC 7742. For those rings that contain a gradient we also find no correlation between the presence of the gradient and direction of the ring rotation.

In relating the location of the youngest H II regions to those of the contact points between the dust lanes and ring, we have been assuming that massive SF will follow very rapidly once the inflowing gas joins the ring. The appearance of a gradient in the ring may thus depend on whether or not material flowing in will immediately trigger gravitational collapse, and initiate massive SF. This in turn may be due to either a higher mass inflow rate (or possibly increased clumpiness of the inflow) and/or an overall higher existing gas density in the ring. Each of these possibilities will ensure that soon after a clump of inflowing gas joins the ring, it will start to form massive stars. The alternatives, of low inflow rate and/or overall low gas density in the ring, might lead to a more gradual increase of the gas density, without necessarily leading to immediate gravitational collapse and massive SF on short timescales. In this case, the positions of the H II regions would bear no relation to the locations of the contact points. The ring would, in such a case, merely increase its gas density gradually, until at some stage, somewhere along the ring, an individual clump would become unstable to collapse; therefore, no age gradients would ensue.

To test this simple model, we must first consider the quantities mentioned above, gas inflow rate and gas density in the ring. These can in principle be determined from interferometric CO measurements, but the process is not straight-

forward. The main issues are the conversion factor of L_{CO} to M_{H_2} (the X -factor), which may well not be equal to the canonical value in the kind of environments we consider here, and the determination of the fractions of detected molecular gas which are in fact flowing into the ring rather than around it (as a consequence of a “spray-type” flow, see, e.g., Regan, Vogel & Teuben 1997; Jogee et al. 2002), or with the right physical conditions such as velocity dispersion and clumpiness to take part in the massive SF process. So although CO interferometry has been presented for seven of our nuclear rings in the literature (by Regan, Vogel & Teuben 1997; Sakamoto et al. 1999; Jogee et al. 2002, 2005; Helfer et al. 2003; Combes et al. 2004; García-Burillo et al. 2005), we will not attempt here to derive the gas inflow rate and gas density in the ring from this collection of data, all with different observational characteristics. For two of our rings, NGC 1530 and NGC 5248, gas inflow rates have been explicitly determined in the literature. For the former galaxy, Regan et al. (1997) give a value of $\dot{M} = 1 \text{ M}_{\odot} \text{ yr}^{-1}$, whereas Jogee et al. (2002) determine a value of “a few” $\text{M}_{\odot} \text{ yr}^{-1}$ for the latter galaxy. Considering the uncertainties in these values, we can say little more than that they are consistent with the SFRs determined for our nuclear rings (see discussion below, and values in Table 3.1).

We could assume that the SFR of the ring can act as a tracer of the inflow rate, although that would imply assuming, for instance, that inflowing gas is transformed into massive stars on very short timescales. If we do this, we would expect the age gradients to occur in those galaxies with the higher SFRs, which would be representative of higher gas inflow rates. In contrast, lower SFRs would indicate a low inflow rate so that the gas will gradually fill the ring, leading to SF only if and

when the local gas density leads to gravitational collapse. This will occur essentially at random and thus result in a ring with no gradients.

Kennicutt (1998) derives a relation between the $H\alpha$ ionizing flux and the SFR for normal disk star forming galaxies, where the conversion factor is computed using stellar population synthesis modeling. Since only stars with masses larger than $10 M_{\odot}$ and lifetimes less than 20 Myr dominate the integrated ionizing flux, the $H\alpha$ emission line provides a nearly instantaneous and linear measure of the SFR, independent of the previous star formation history. For solar abundances and our adopted IMF ($\alpha = 2.35$; $M_{\text{low}} = 1 M_{\odot}$ and $M_{\text{up}} = 100 M_{\odot}$), we can use Kennicutt's (1998) equation:

$$\text{SFR}(M_{\odot} \text{ yr}^{-1}) = 7.9 \times 10^{-42} L(H\alpha) (\text{erg s}^{-1}).$$

to compute SFRs integrated over the entire ring, which are given in column 10 of Table 3.1. Since a nuclear ring environment is similar to that of a star forming disk region (i.e., a patchy region of active star formation versus a classical starburst), we claim that the choice of a higher upper mass limit is more representative of the physical environment.

Variable extinction certainly adds uncertainty in the computation of the SFR for circumnuclear regions. The patchiness of the extinction is very clear in several of our galaxies (e.g., NGC 473, NGC 613, NGC 1530, NGC 5945), which reveal only partial rings in $H\alpha$. The less obscured regions will contribute more heavily to the line fluxes in these cases. It is difficult to precisely model the effect of the

dust, but attempts have been made for nuclear regions in particular. Osmer, Smith, & Weedman (1974) analyzed six galaxies and derived integrated extinction values across the entire circumnuclear region ranging from $A_{\text{H}\alpha} \approx 2.5 - 3$ mag, while Hummel, van der Hulst & Keel (1987) found an extinction of $A_{\text{H}\alpha} \approx 1.1$ in the central region of NGC 1097. Kennicutt (1998) acknowledges the high uncertainty and estimates that the errors in the SFR can be as high as $\pm 50\%$. A high-resolution survey paper by Phillips (1996) for nine circumnuclear regions confirms the potential for high uncertainty values. Following Kennicutt, he finds that the SFRs vary by as much as a factor of ten when applying extinctions of $A_{\text{H}\alpha}=1.1$ and $A_{\text{H}\alpha}=3.4$ mag. He concludes that circumnuclear SF can be a dominant factor to the overall rates of such galaxies. We thus place the same caution that our SFRs contain potentially high uncertainties due to variable extinction throughout the nuclear rings.

Figure 3.8 plots the integrated SFR over the entire ring for all galaxies and distinguishes those rings that show a gradient and those that do not. There is no obvious correlation between the SFR and the appearance of a gradient. The average mean for those without gradients ($\overline{\text{SFR}} = 3.6 \pm 2.5 M_{\odot} \text{ yr}^{-1}$) is slightly larger for those with a gradient ($\overline{\text{SFR}} = 2.2 \pm 2 M_{\odot} \text{ yr}^{-1}$), but given the large mean deviations, we cannot distinguish in a statistical sense between the two cases. This could be due to several factors. All of the gradients, except for those in NGC 1343 and NGC 4321, are partial gradients. That is, their gradient does not range continually from one contact point to the next. NGC 1343 and NGC 4321, which represent the “ideal” scenario, do have high SFRs ($6.8 M_{\odot} \text{ yr}^{-1}$ for both cases) when compared to the rest of the sample. Computing the average SFR of the ring also is insensitive to the

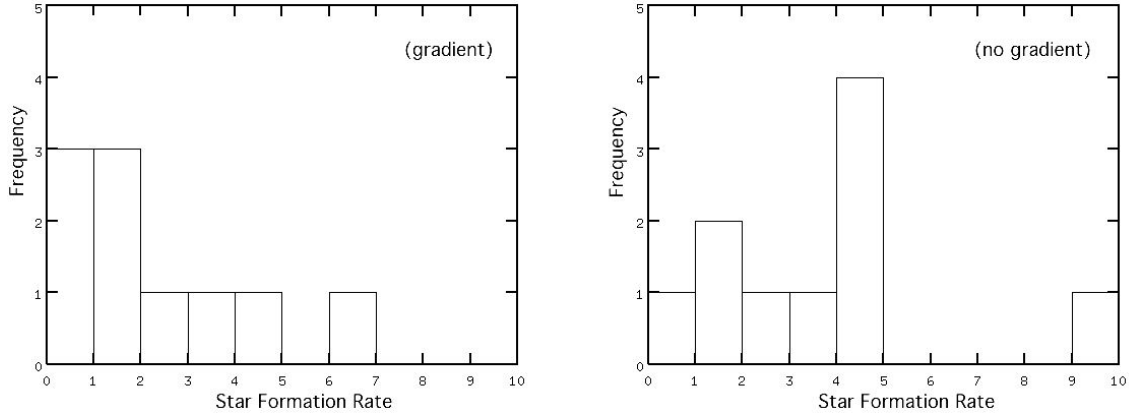


Figure 3.8: Integrated SFR of the rings. The SFR is compared to the presence (left panel) or absence (right panel) of an age gradient. The mean SFR values are $2.2 \pm 2 \text{ M}_{\odot} \text{ yr}^{-1}$ for the galaxies with and $3.6 \pm 2.5 \text{ M}_{\odot} \text{ yr}^{-1}$ for those without gradients.

steepness of the gradient, the size of the ring, the size of the individual H II regions, or the patchiness of the ring, which all add complexity to the interpretation of the data.

From our analysis of age gradients we thus conclude that although age gradients along the ring are detected convincingly in more than half of the rings, all other rings show random variations of H II region EW, and thus age, with azimuth. We cannot pinpoint any morphological parameters that might distinguish the host galaxies and bars of those rings with from those without gradients. Another strong conclusion from our analysis is that the kind of clear bi-polar age gradient seen before in NGC 4321 (Ryder, Knapen, & Takamiya 2001; Allard et al. 2006) is rare - we only see a similar bi-polar gradient in one more galaxy, NGC 1343. It is not clear why these two galaxies show their gradients, whereas other galaxies with very similar bar-ring systems show gradients that are not bi-polar, or no gradients at all.

3.6.3 Nuclear Ring and Stellar Bar Dynamics

It is agreed that the presence of a galactic bar can have significant influence on angular momentum and re-distribution of gas, including inflow towards the central regions (e.g., Combes & Gerin 1985; Heller & Shlosman 1996; Knapen et al. 1995a). Observed kinematics reveal that the shock-induced flows move gas radially inwards along the bar dust lanes and tend to collect at the intersection of the dust lanes with the ring. These contact points are thought to be approximately perpendicular (within the plane of the disk) to the PA of the bar major axis (Regan & Teuben 2003) but have been seen to lead the bar by as little as 60° in numerical models (Heller & Shlosman 1996). The pile up of gas at these two points in the ring can be expected to spark SF. Therefore, one could predict to find the youngest stellar H II regions in the ring near the contact points.

For the barred spiral galaxies in our sample, we compare the location of the youngest H II regions in the ring to the derived location of the contact points. We first identified the youngest H II region in each hemisphere, where the hemispheres are separated by the bar PA. Taking into account the direction of flow around the ring (from our $B - I$ images), we calculate the PA offset between the H II region and the contact points. Table 3.2 shows the PAs of both the contact point and the youngest H II region in each hemisphere, along with the directional flow of the ring. We find that in two-thirds of the galaxies, one of the bar contact points is aligned with the youngest H II region in the associated hemisphere within 20° of the contact point. Two galaxies, NGC 4314 and NGC 5248, have the youngest

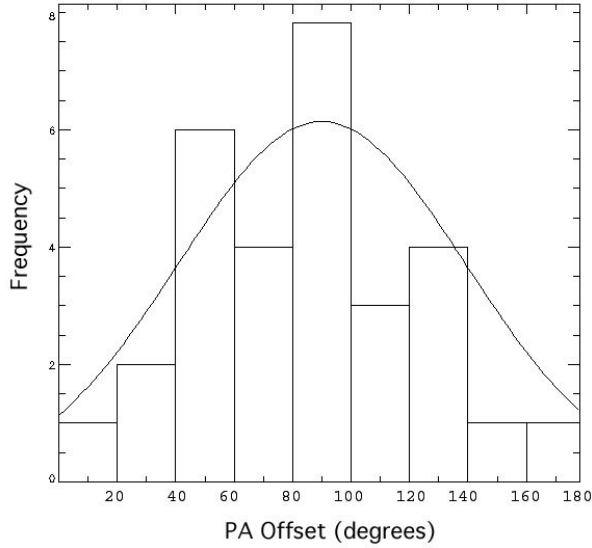


Figure 3.9: Histogram showing the distribution of angular offsets between the bar major axis PA and the locations of the youngest HII region in each hemisphere, which is bisected by the bar. A Gaussian fit to the distribution is overlaid, and shows a peak at an offset of 90° , which is consistent with the location of the contact points. See Table 3.2 for more details.

H II region in both hemispheres aligned with the contact points. Our results for both of these rings are consistent with those of Benedict et al. (2002) and Maoz et al. (2001), respectively, who also find that the youngest stars were located at the contact points. Figure 3.9 shows a histogram of the distribution of the angular offsets between the bar major axis and the locations of the two youngest HII regions in each ring. A peak in frequency around the contact point locations is seen and a Kolmogorov-Smirnov (KS) test confirms that the cumulative distribution of the data is not uniform.

We next compare the times from the bar major axis PA to the location of the contact points with those of the youngest H II region in each hemisphere, assuming we azimuthally move in the direction of ring flow. We compute the period of the

rings using measurements of the ring radius and the rotational velocity at the ring radius. We chose the major axis length of each ring as derived from ELLIPSE (see Section 3.3 and Table 3.1), and obtained the rotational velocity values from the literature and from our own DensePak IFU data taken in 2003 & 2004 (L. M. Mazzuca et al. 2006, in prep.). Table 3.3 shows the major axis ring radius, the adopted rotational velocity along with its reference, and the period for each ring. Since we predict the contact points to be $\sim 90^\circ$ from the bar major axis, we can compute their location with respect to the bar PA in each hemisphere, and thus calculate the amount of time it would take to travel to that location. We compare this travel time to that associated with the location of the youngest H II region in each hemisphere. Figure 3.10 plots the travel times to the contact points versus the times of youngest H II region in each hemisphere from the bar PA. Overall, the travel times to the contact points are very similar to the times computed from the bar PA to the youngest H II regions. We find only one H II region, in NGC 1530, that deviates from the general trend. In this case, the youngest region in one of the hemispheres is more aligned with the PA of the ring than that of the bar.

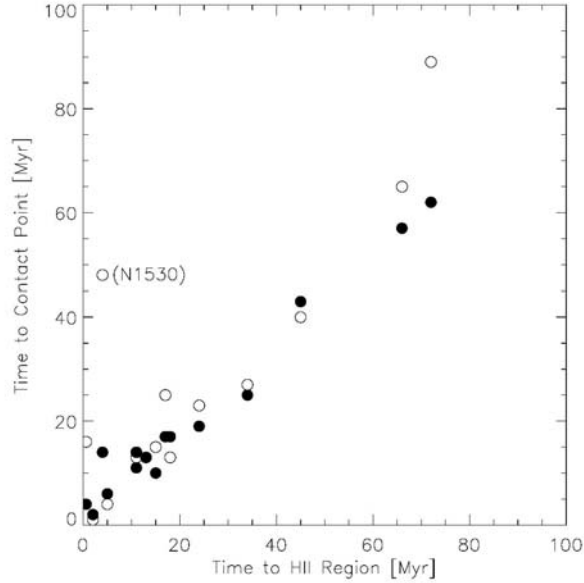


Figure 3.10: Comparison of travel times from the bar major axis PA to the contact points versus times to the youngest H II region in each hemisphere. Each ring has two contact points (intersection of the dust lanes with the ring at a 90° offset from the bar PA). We find the youngest H II region in each hemisphere as bisected by the bar and compare the travel time from the bar major axis to the H II region with that of the contact point location. Solid diamonds represent the comparison in one hemisphere, and open boxes in the other hemisphere. The linear relation indicates the times to the youngest H II regions are comparable to those of the contact points, which is consistent with the H II regions corresponding to the contact point locations. The time from the bar major axis PA to the contact point versus that to the youngest H II region in one of the hemispheres of NGC 1530 does not correlate with that of its respective contact point. See Table 3.3 for more details.

3.7 Conclusions

From a larger H α imaging survey we identified 22 galaxies that contain a nuclear ring. To identify their sizes and shapes, we fitted each ring with an ellipse based on the peak isophotal intensity across the radial range of the ring. The rings vary in size from 0.2 kpc to 1.7 kpc in major axis radius. We compare the ring morphologies to those of their host galaxies. In all but one case the ellipticity and PA of the rings approximately match that of their respective disk, which corroborates the idea that the ring is in the same plane as the disk, and circular. The exception is NGC 7570, which shows a distinct and self-consistent difference in both the PA and eccentricity in the ring versus the disk.

All but one of the rings had sufficient spatial resolution for us to identify individual H II regions. For each H II region, we computed the EW and converted differences between them into relative ages and age gradients using the Starburst99 evolutionary models. Although we adopted an instantaneous starburst model, we acknowledge that the rings may be more representative of a hybrid episodic scenario where star formation toggles between latent and active periods corresponding to the time it takes for gas build-up to reach critical density. Three rings, NGC 1343, NGC 1530, and NGC 4321, contain bipolar age gradients, where the ages increased from each of the contact points. Many of the rings in our sample exhibit a well-defined age distribution pattern, but not throughout the entire ring. This can be a result of the combination of bar-induced dynamics and gravitational instabilities that are occurring on an intermittent basis. We calculated the SFR in each ring

from the integrated luminosity contributed by all of the H II regions forming the ring, and compared those rates to the appearance of a gradient within each ring (or lack thereof). The large uncertainties associated with variable extinction across the rings and the large dispersion of SFR values for both cases yields no clear correlation between the SFR and the emergence (or lack thereof) of an age-dependent azimuthal distribution. We do see a connection between the location of the bar contact points and the youngest H II regions in two-thirds of the galaxies in our sample.

Chapter 4

Gas Kinematics in Nuclear Rings

4.1 Overview

Nuclear rings are seen as a by-product of gas inflow into the central regions of barred spiral galaxies, where they are preferentially found (e.g., Buta & Combes 1996, Heller & Shlosman 1996). The bar acts as a dominant source of fuel to the nuclear ring due to its ability to drive dust and gas radially inward. At the ring radius, material is significantly slowed down as the angular momentum loss experienced along the bar greatly decreases. This allows gas to accumulate at the ring radius, and ultimately spark star formation (Schwarz 1984; Combes & Gerin 1985; Shlosman et al. 1989). Kinematics have revealed that bars can perturb the potential and cause non-circular motions in the circumnuclear regions, as first noted by Rubin et al. (1975) and Peterson et al. (1976). Although small-scaled structures (~ 1 kpc in radius), a nuclear ring can also disturb the axisymmetry of the gas, as the ring intermingles with the dust lanes of the parent bar (e.g., Knapen et al. 1995; Heller & Shlosman 1996).

Kinematic models of circumnuclear regions containing a bar and a nuclear ring reveal a symbiosis between the two structures. Knapen et al. (1995) model the response of gas and stars caused by the presence of a nuclear ring and a bar. They show that the existence of the nuclear ring results from the gas response to

the nonaxisymmetric bar potential, in conjunction with the mass distribution of the galaxy. The distribution pattern is directly related to the presence of two Inner Lindblad Resonances (ILRs), and the x_2 family of orbits aligned with the bar minor axis, that reside between them. Heller & Shlosman (1996) add that the nuclear ring can ultimately weaken or even destroy the bar that feeds it, as it grows and increases the phase space allowable to the x_2 family, mostly towards the outermost orbits near the bar. This close relationship between the nuclear ring and bar is also modeled by Regan & Teuben (2003), who show a direct correlation between the location of where the bar dust lanes intersect the nuclear ring, along the bar minor axis, and the existence of the strongest velocity residuals within the ring and across the outer ring boundary. Of the small number of in-depth kinematic observational studies of nuclear rings (CO emission: Jogee et al. 2002 (NGC 5248), Benedict et al. 1996 (NGC 4314); CO + H α : NGC 4321, Knapen et al. 1995 & 2000, NGC 1530, Zurita et al. 2004; H β : NGC 4321, Allard et al. 2006), results mostly agree with the models.

CO kinematic studies reveal a correlation between the residual velocities and the existence of active star formation. Reynaud & Downes (1998) find that, for NGC 1530, strong velocity changes are inversely correlated with star formation. The existence of strong transitions indicate shocks and shears, which create an environment too turbulent to allow gas to form concentrated zones that may condense to form stars. They conclude that velocity gradients of order 100 km s^{-1} would prevent enhanced star formation. If this is true, then the residuals in all nuclear rings should be relatively low in order to be consistent with the fact that nuclear

rings harbor very young massive star formation (see Chapter 3 and the references there in).

In this paper, we present a detailed $H\alpha$ kinematic study of ten nuclear rings in nearby spiral galaxies, eight of which are clearly barred. The rings studied here are a subset of those presented in the imaging survey (B , I , $H\alpha$) from Chapter 3. The data in Chapter 3 were obtained to characterize the morphology of the nuclear rings, and to analyze the stellar distribution properties and ages. We now use the kinematic information within and just outside of the rings to draw stronger conclusions between the young massive star formation seen and the degree of residual velocities and gas dispersions. We begin by presenting an overview of the observations and morphological properties of the $H\alpha$ sample in Section 4.2. We discuss the basic data reduction method, which includes the construction of the velocity field (VF) maps, in Section 4.3. In Section 4.4 we derive the kinematical parameters associated with the rotation curves (RCs) of the nuclear regions, and present results pertaining to non-circular motions in and around the nuclear rings, including velocity residuals and dispersions. Our interpretation of the results are discussed in Section 4.5, with a summary in Section 4.6.

4.2 Sample and Observations

In December 2003 and April 2004, we obtained two-dimensional $H\alpha$ velocity maps for ten nuclear rings using the **DensePak** fiber-optic array and Bench spectrograph on the 3.5m WIYN (joint facility of the University of Wisconsin-Madison,

Indiana University, Yale University, and National Optical Astronomy Observatories). Eight of the ten nuclear rings are a subset of a larger H α nuclear ring imaging survey performed in 1999 using the AuxPort camera (Knapen et al. 2006; Chapter 3) at the William Herschel Telescope (WHT). These nuclear rings were chosen based on the confirmation of identifiable H II regions delineating the ring, a projected non-zero inclination, and a measurable position angle (PA). Rings too diffuse or small, with no resolved H II regions, were rejected. NGC 2903 and NGC 3351 were added to the sample based on their well-known nuclear ring structures, even though their sizes (all less than 1 kpc in radius) are considered small. We independently determined their ring inclination, PA, and size using the same method as described in Chapter 3. The ring sizes in our sample vary between 2'' and 12'', which all fit well into the array field of view (FOV). Table 4.1 shows the various morphological parameters for the sample.

The **DensePak** Integral Field Unit (IFU) Spectrograph (Barden & Wade 1988) consists of 91 fibers bonded into a 7×13 staggered rectangular grid that covers an area of $30'' \times 45''$ of sky with center-to-center fiber (3'' diameter) spacings of 4''. Four of the fibers are allocated as sky fibers, and are spaced around the grid roughly 1' from the center. The spectrograph was configured with the Bench camera, the Tek 2048 CCD (T2KC), the 860 l mm^{-1} grating, in the second order, centered at 6575 Å. We used a third order blocking filter (GG495). This arrangement provided a final spectral coverage of 925 Å from 6085 Å to 7010 Å at a resolution of 0.45 Å per pixel. The spectral range included H α as well as the [N II] $\lambda\lambda$ 6548, 6583 and [S II] $\lambda\lambda$ 6716, 6731 lines. The instrumental resolution was different for the two runs,

NGC	Morph Type	Center _{phot}		i ($^{\circ}$)	PA _r ($^{\circ}$)	PA _d ($^{\circ}$)	PA _b ($^{\circ}$)	Radius	Radius	Width	Run
		x ($''$)	y ($''$)					($''$)	(kpc)	($''$)	Date
473	SAB(r)0/a	-4.4	+7.2	49	154	153	164	12.2×6.9	1.7×1.0	4.4	Dec03
1343	SAB(s)b	-4.4	+7.8	41	60	80	82	8.8×6.6	1.2×0.9	2.2	Dec03
1530	SB(rs)b	-1.6	+11.3	48	25	8	122	6.8×4.9	1.2×0.8	3.5	Dec03
2903	SB(s)d			65	8	17	24	1.7×1.0	0.06×0.04	1.9	Dec03
3351	SB(r)b			34	20	13	112	2.7×1.9	0.15×0.11	1.7	Dec03
4303	SAB(rs)bc			18	88	-	-	3.3×2.8	0.2×0.2	1.4	Apr04
4314	SB(rs)a	-3.0	+6.3	26	135	-	148	6.6×5.9	0.3×0.3	2.4	Apr04
5248	SB(rs)bc	-3.3	+6.5	46	115	110	137	6.6×4.6	0.7×0.5	4.5	Apr04
5953	SAa	-6.0	+6.6	26	172	169	no bar	6.1×5.5	1.0×0.9	5.6	Apr04
7742	SA(r)b	+0.7	+7.5	18	133	-	no bar	9.9×9.4	1.0×1.0	5.7	Dec03

Table 4.1: Morphological and photometric parameters for the observed sample. Galaxies are listed in order of increasing RA (col. 1) with morphological type (col. 2) from RC3. Col. 3 lists the optical center of the H α image, as offset with respect to the center of the DensePak array. The center offset is oriented such that astronomical North and West are in the positive direction. The nuclear ring inclination (col. 4), PA (col. 5), and size (Cols. 8 and 9) were derived photometrically (H α imaging from Chapter 3) using the IRAF ELLIPSE task. The radial width of the ring is in col. 10. The disk PA (col. 6) is from RC3, and the bar PA (col. 7) is from Chapter 3, with the run date in col. 11.

which can be attributed to instrument setup. For the December 2003 run, the instrumental resolution (FWHM) averaged 0.97 \AA (44 km s^{-1}) around H α , with the resolution for the April 2004 at 1.31 \AA (60 km s^{-1}).

The center of each galaxy was positioned in the array to optimize the area of the entire ring while mitigating the impact of the dead fibers in the array. To avoid placing a part of the ring over a dead fiber, we limited ourselves to the upper North-East quadrant of the array. Because of this method, many of the rings approached the edge of the FOV along the array minor axis, which limits our discussion regarding the environment exterior to those rings in the North-East sectors. We used two to four pointing offsets, each 1800s in duration, to fill the dead fibers. This method also improved the sampling in some cases (see Section 4.3 for details). The major axis of the array was aligned along a North-South direction of each galaxy.

4.3 Data Reduction

The raw CCD frames were zero and bias-corrected, flat-fielded, cosmic-ray cleaned, and combined using the standard IRAF NOAO packages (ZEROCOMBINE, CCDPROC, FLATCOMBINE, COSMICRAYS, and IMCOMBINE, respectively). The combined images were wavelength-calibrated using the NOAO IRAF data reduction package DOHYDRA to extract the net spectrum yielded by each fiber. A CuAr comparison source was used for wavelength calibration. The reduced two-dimensional spectral image contains 89 rows, where each row is one pixel in height and corresponds to a fiber.

We created GIPSY (van der Hulst et al. 1992; <http://www.astro.rug.nl/gipsy>) scripts to identify and then subtract the continuum and sky from the VF following the method described in Bershady (2005). A first pass through the script subtracted the continuum within each fiber, and the sky lines across the image. Due to pointing uncertainties at the time of the runs, we established the measured pointing offsets (i.e., the shift from the center of the **DensePak** fiber array to the ring center) before the second pass. We followed the procedure outlined in Swaters et al. (2003), where the fitted continuum flux levels are used to determine and register the actual pointing offsets. Continuum levels are measured and compared with those from a constructed model using an *I*-band image, with known coordinates, from our AuxPort sample. By repeating this process for all positions in the image, we created a landscape contour grid of χ^2 values, where the minimum χ^2 corresponds to the measured pointing offset. To subtract the sky lines from the data, we directly used the values

obtained in the four reserved **DensePak** sky fibers, each located $1'$ from the center of the array, and averaged them since the sky fibers contained no $H\alpha$ emission from the target galaxy.

To construct a sparse VF map of the combined pointings, we first fitted Gaussians to the continuum- and sky-subtracted line profiles, using a 3σ threshold to unambiguously identify the $H\alpha$ emission lines. The velocities from the resulting $H\alpha$ lines were derived at each fiber and placed in a map at corresponding positions. We applied a correction to the observed velocities so that they can be compared to catalogued heliocentric velocities. In the cases of multiple velocity measurements at the same location (i.e., within the pixel size of the VF, 0.25\AA) we averaged the line profile fits before placing them into the map. To aid in the visual representation of the fiber points, we constructed contiguous VF maps. We created Gaussians with a beam of $5''.5$ around each data point and weighted the overlapping sections between the points. The weighted data points were then interpolated to form a smoothed VF map, as shown in Figure 4.1, for all of the galaxies. These maps should only be used for general impressions, however, since the results may not be accurate due to interpolation effects. Any quantitative interpretation comes from the sparse velocity maps, which have no interpolation of the data points. Figure 4.1 also plots the VF contour overlays, which are superimposed onto the $H\alpha$ images. The VF maps were registered with the AuxPort optical $H\alpha$ images so that they match in sky projection.

4.4 Results

4.4.1 Rotation Curve

For each galaxy, we derived the RC from the projected radial velocity map following the procedure outlined in Begeman (1989):

$$v_{proj} = v_{sys} + v_{rot} \cos(\theta) \sin(i) \quad (4.1)$$

where v_{proj} is the line-of-sight radial velocity at the sky coordinates x and y over the FOV, v_{sys} the systemic velocity, θ the azimuthal angle of the major axis in the plane of the ring with respect to the rotation center and PA, and i the inclination. We gave more weight to those positions along the major axis, since those data points carry most of the information about rotational velocities.

The RC is determined by fitting tilted rings to the observed VF. We chose the incremental radius to be $1''5$, which is approximately half of the width of a given fiber. Initial input values for all but V_{sys} originate from I -band images using the AuxPort camera as observed in either Chapter 3 or previous imaging. One exception is NGC 5953, whose systemic velocity was derived from the data due to a 26 km s^{-1} discrepancy with the NED value. The NED cited velocity may be influenced by the companion galaxy, NGC 5954. We derived the initial center position by taking the point where the I -band emission is the highest near the galaxy center. The input value for v_{sys} in the fit to the VF is from the NASA/IPAC extragalactic database (NED). To optimize the fit, each parameter was averaged only over radii where the scatter was low. Since most of the nuclear rings contained in the sample are of

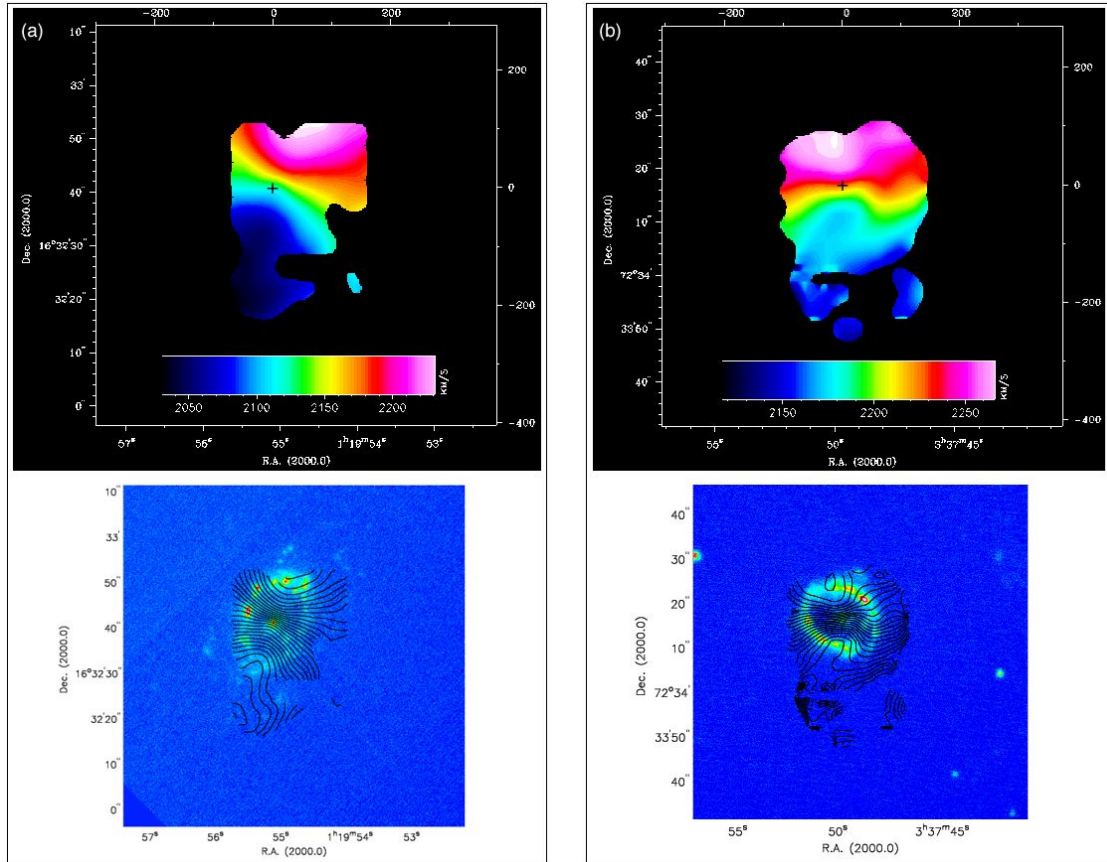


Figure 4.1: H α velocity field map (top) and velocity contours superimposed on the H α continuum-subtracted images (bottom) for: (a) NGC 473, (b) NGC 1343. The center of each nuclear ring is identified by a cross. Each VF map is registered to its respective H α image to account for sky projection differences.

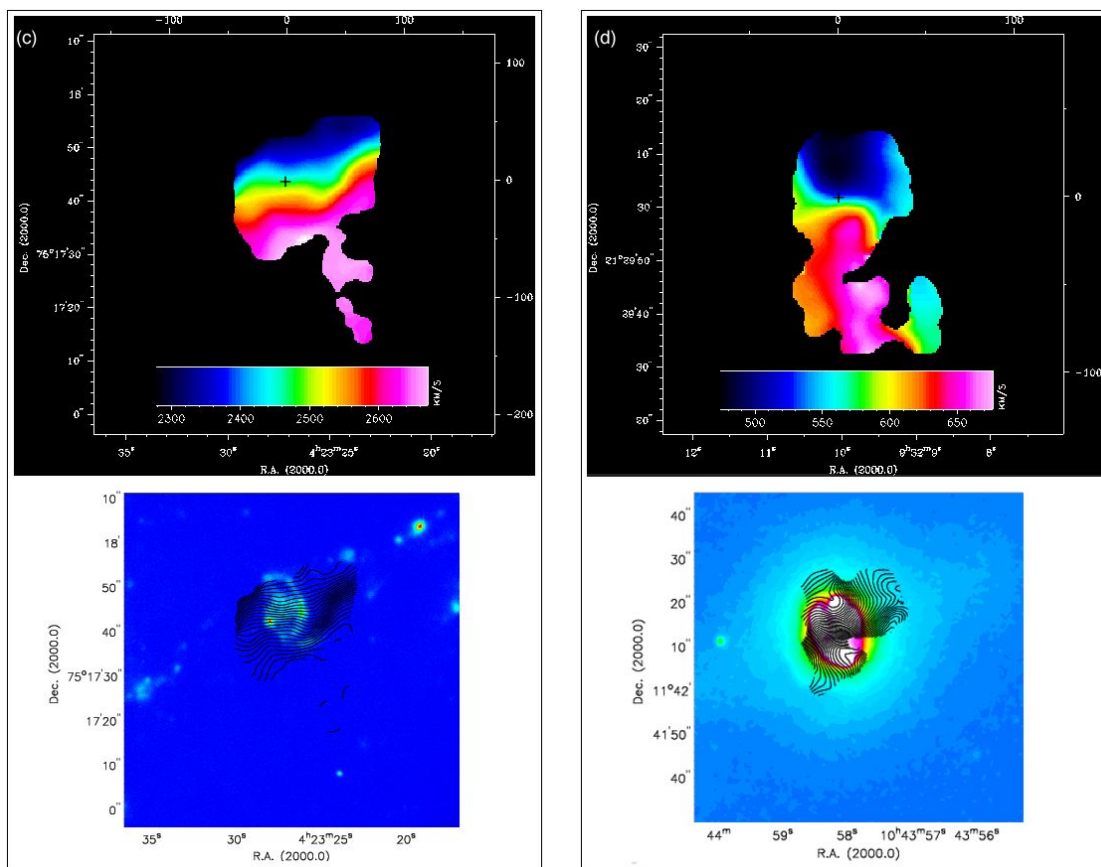


Figure 4.1: Continued. (c) NGC 1530, (d) NGC 2903.

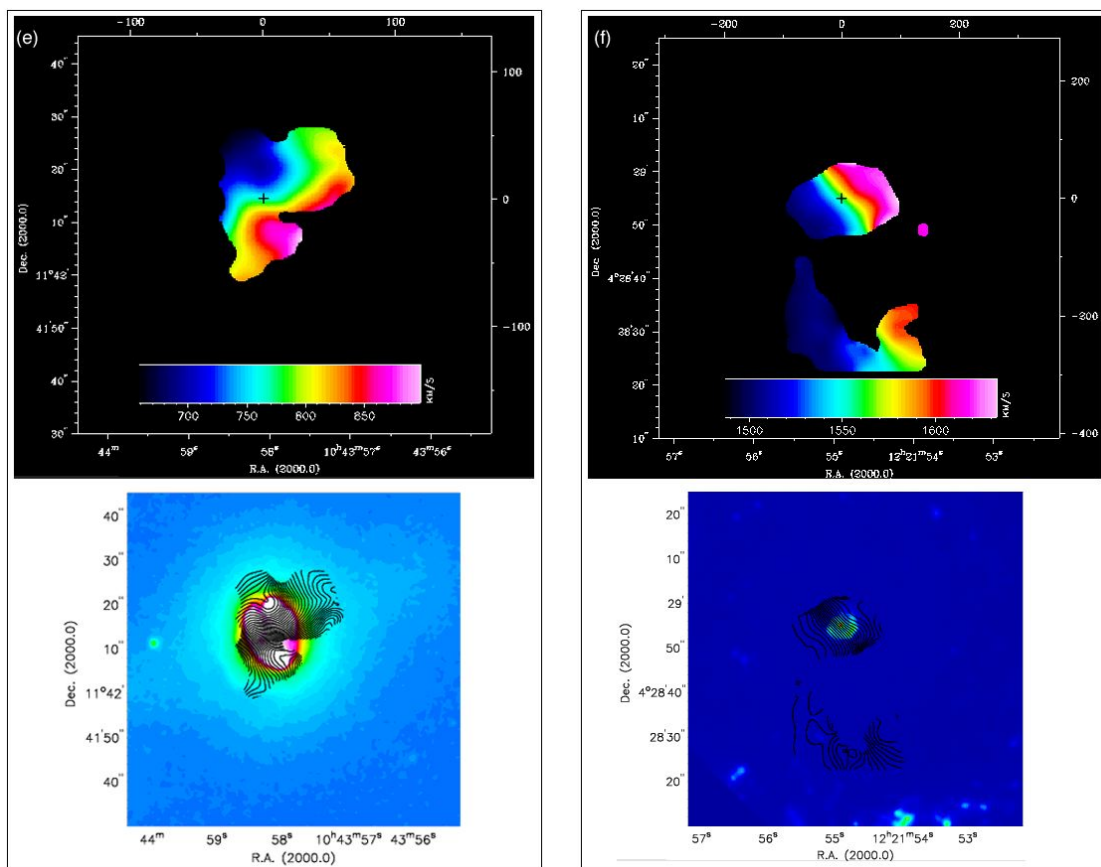


Figure 4.1: Continued. (e) NGC 3351, (f) NGC 4303.

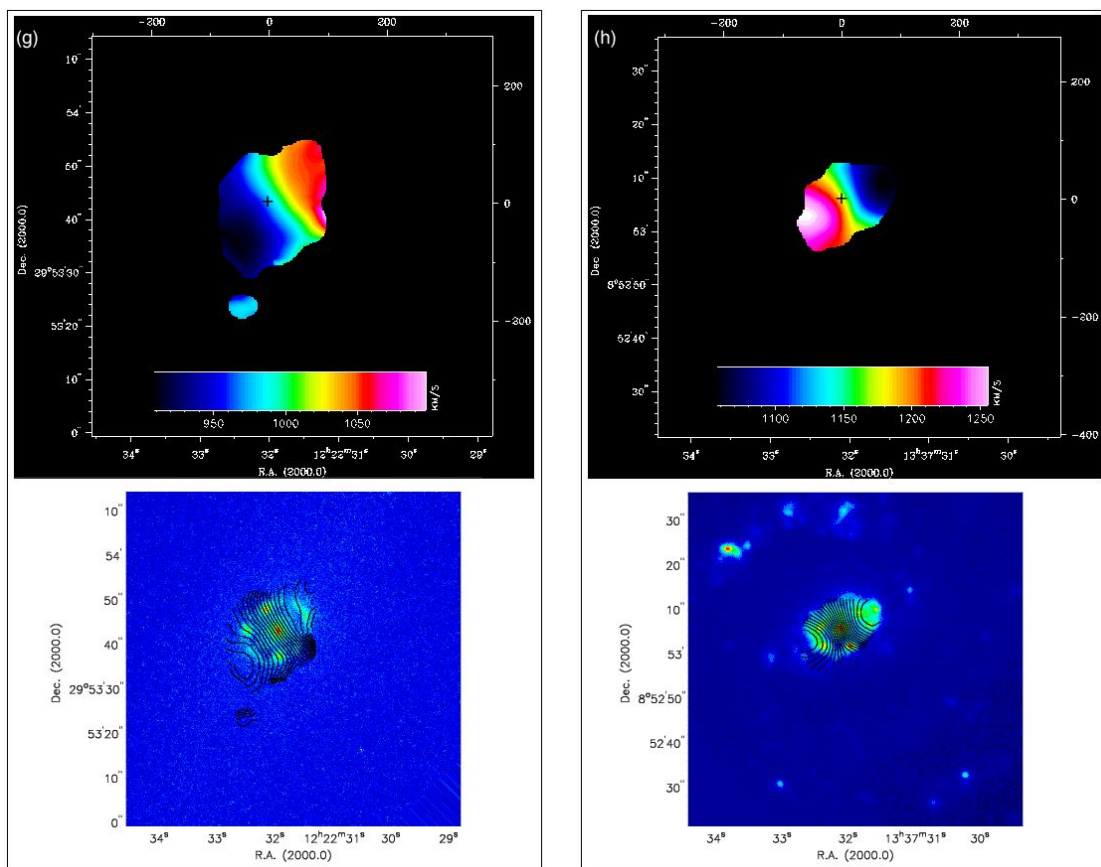


Figure 4.1: Continued. (g) NGC 4314, (h) NGC 5248.

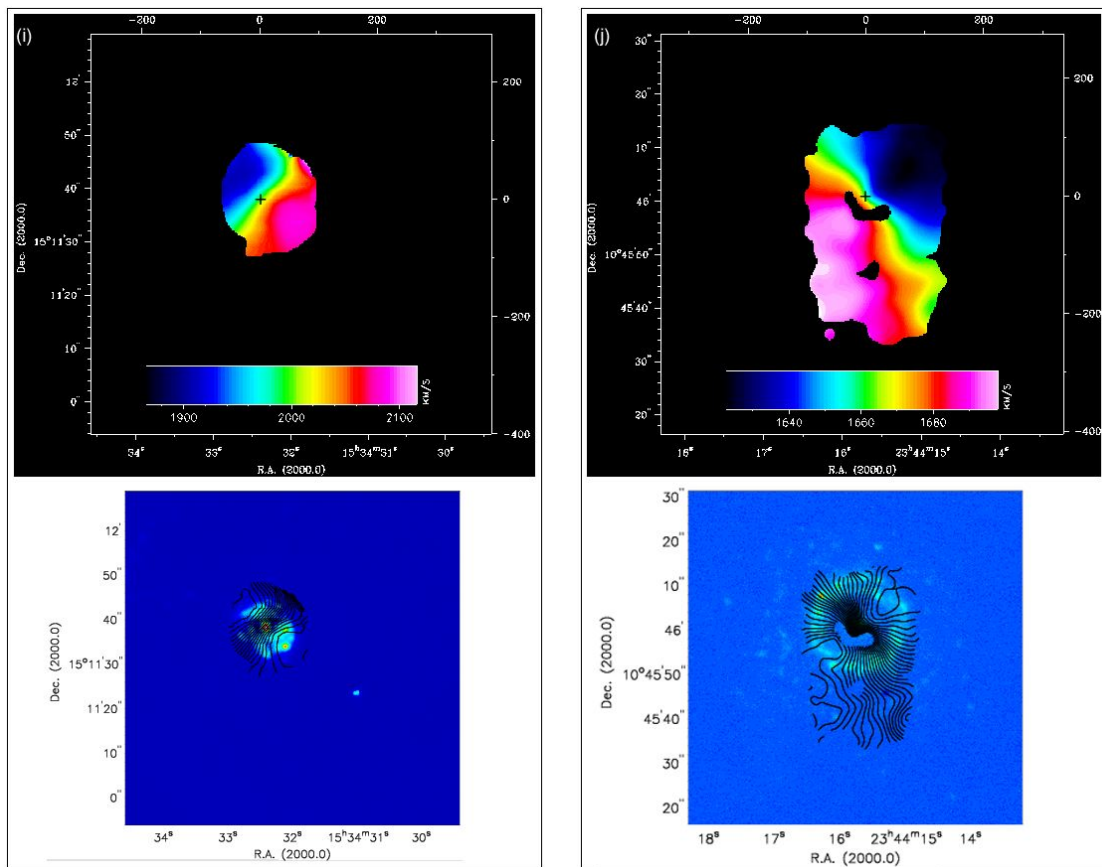


Figure 4.1: Continued. (i) NGC 5953, (j) NGC 7742.

fairly low inclination, the fitting routine had difficulties deriving the kinematical inclination. We therefore adopted the photometric values from Chapter 3, which are more reliable. We fixed all parameters to obtain the rotation velocity curve. Figure 4.2 shows the tilted rings superimposed on an outline of the nuclear ring, along with the positions of velocity data points. The respective RC is presented below each tilted ring image.

Due to their small size, three nuclear rings (NGC 2903, NGC 3351, and NGC 4303) suffered from poor sampling within the ring. This can be seen in the tilted ring plots (Figure 4.2). We therefore are unable to analyze these rings. For the remaining seven nuclear rings, we list the derived kinematic parameters in Table 4.2.

NGC	V_{sys} (km s^{-1})	Center _{kin}		PA _{kin} ($^{\circ}$)	PA _{kin} - PA _{phot} ($^{\circ}$)	Ctr _{kin} - Ctr _{phot}	
		x ($''$)	y ($''$)			x ($''$)	y ($''$)
(1)	(2)	(3a)	(3b)	(4)	(5)	(6a)	(6b)
473	2135	-5.0	+7.5	156±2	2	0.6	0.3
1343	2215	-5.3	+6.5	7±6	53	0.9	1.3
1530	2450	-1.6	+11.0	5±6	20	0	0.3
4314	979	-4.0	+5.5	122±3	13	1.0	0.8
5248	1149	-2.9	+6.3	115±5	0	0.4	0.2
5953	1991	-6.0	+6.7	229±3	57	0	0.1
7742	1658	+0.7	+6.6	131±3	2	0	0.9

Table 4.2: Kinematic parameters for the observed sample. Galaxies are listed in order of increasing RA (col. 1). Systemic velocity (col. 2), nuclear ring kinematic center position with respect to the center of the `DensePak` array (col. 3a & b) and kinematic PA (col. 4) were derived using the `GIPSY ROTCUR` task. The center offset is oriented such that astronomical North and West are in the positive direction. The difference (absolute value) between the kinematic PA and the photometric PA (see Table 4.1) is in col. 5, with the difference between kinematic and photometric centers is in col. 6a & b.

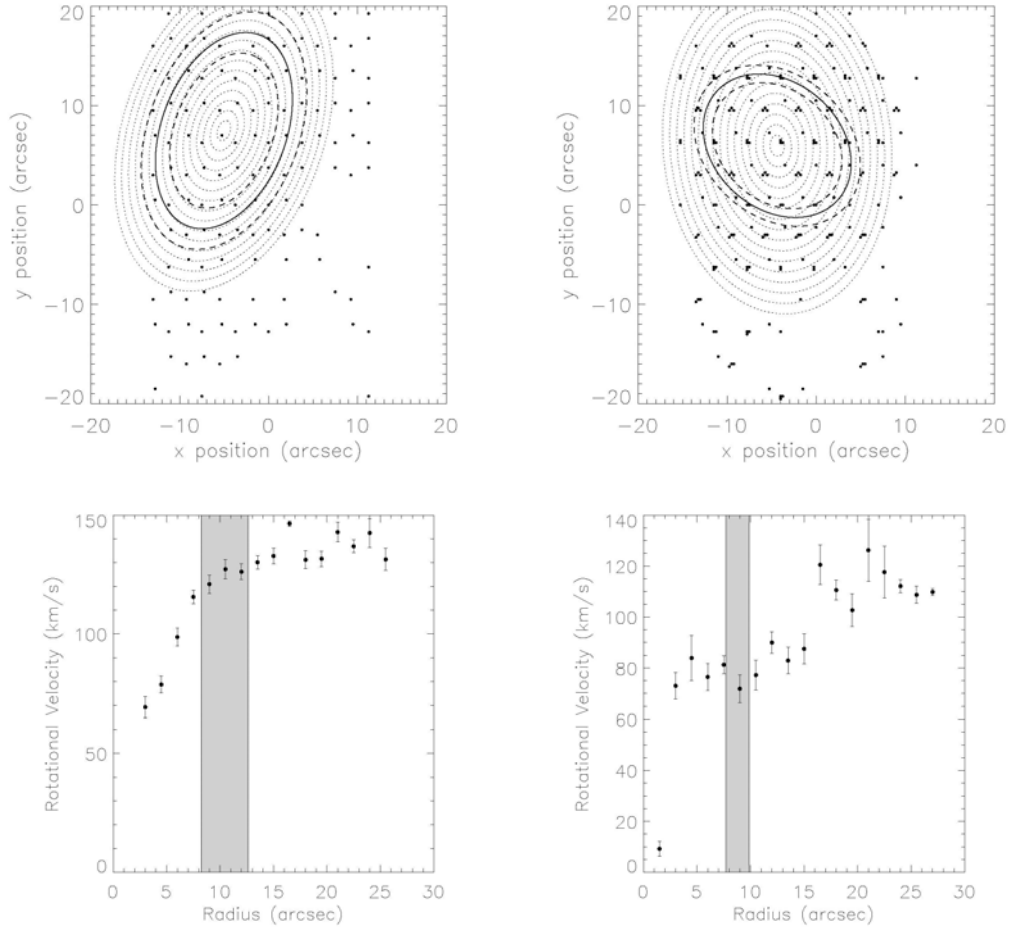


Figure 4.2: Tilted ring model for NGC 473 (left) and NGC 1343 (right). The nuclear ring is overplotted on the DensePak array, which is delineated by an inner edge, center ridge, and outer edge, as measured using the IRAF task ELLIPSE. The velocity data points in the FOV are also drawn in an x, y grid, for all pointings. Beneath each tilted ring image is its respective RC, with the radial range of the ring shadowed.

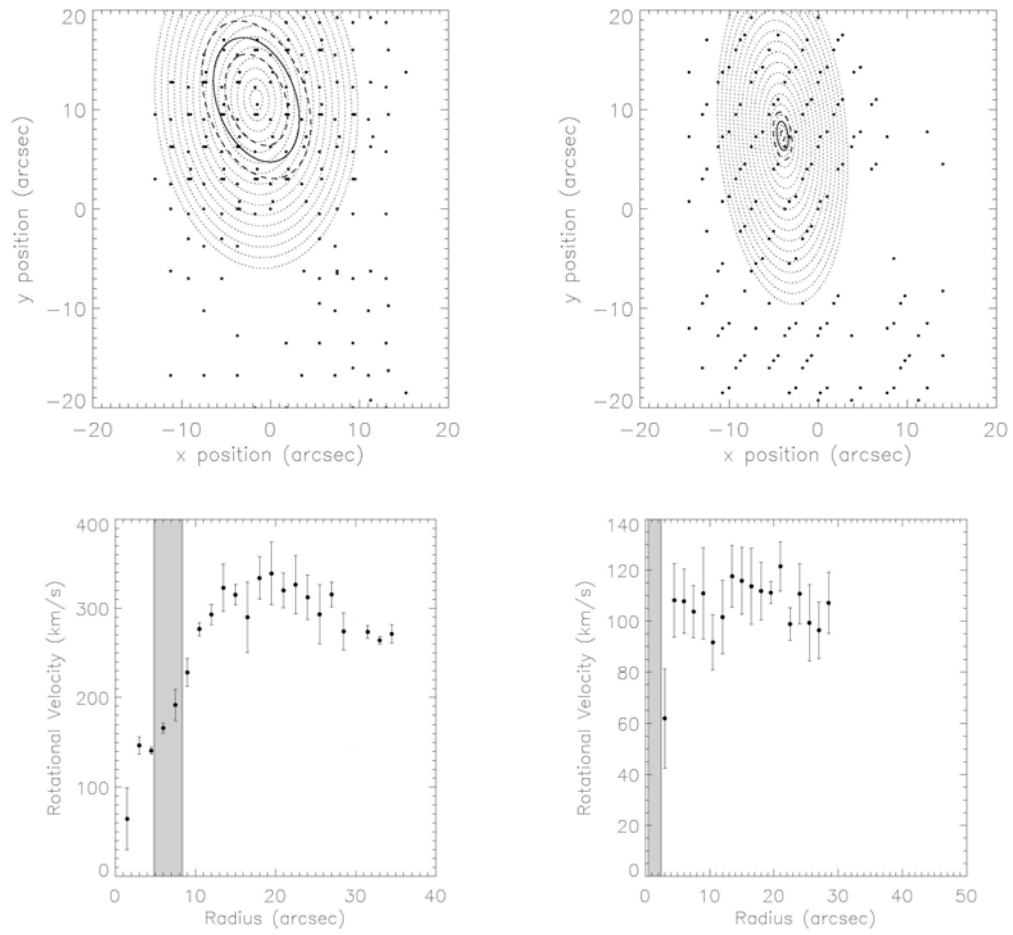


Figure 4.2: Continued. NGC 1530 (left), NGC 2903 (right)

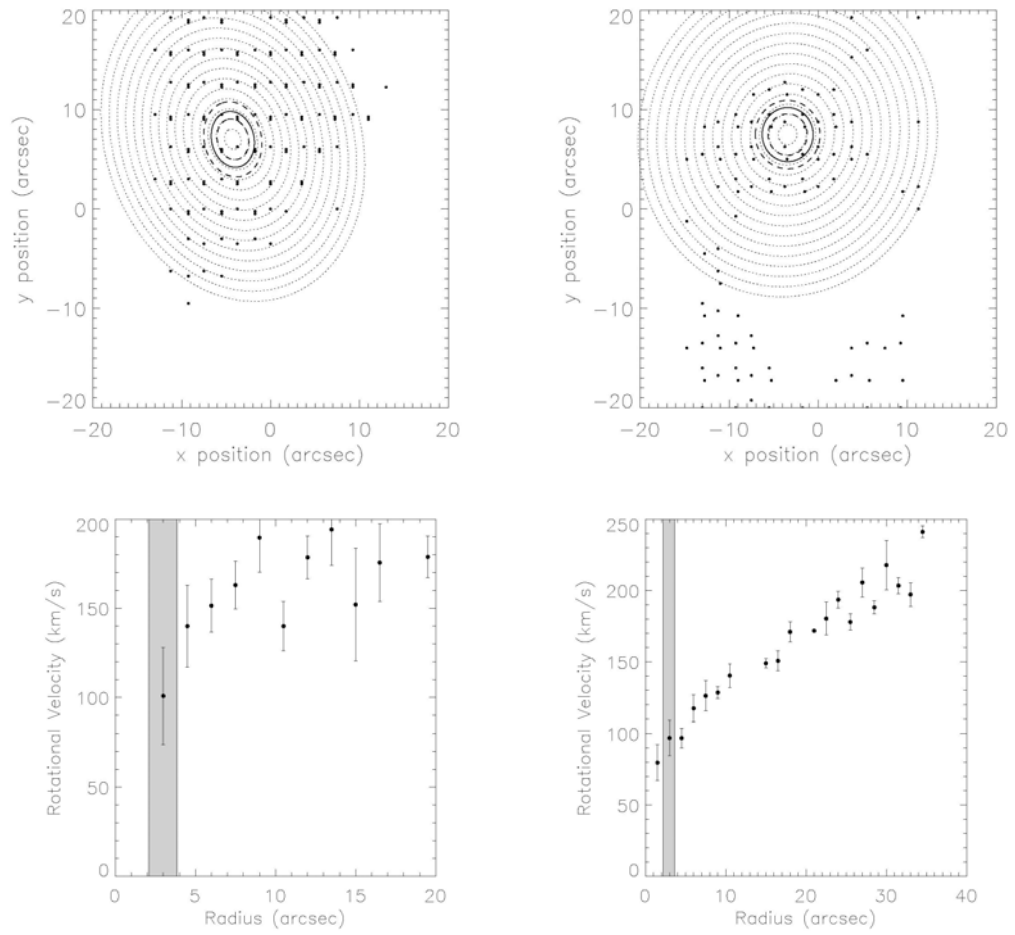


Figure 4.2: Continued. NGC 3351 (left), NGC 4303 (right)

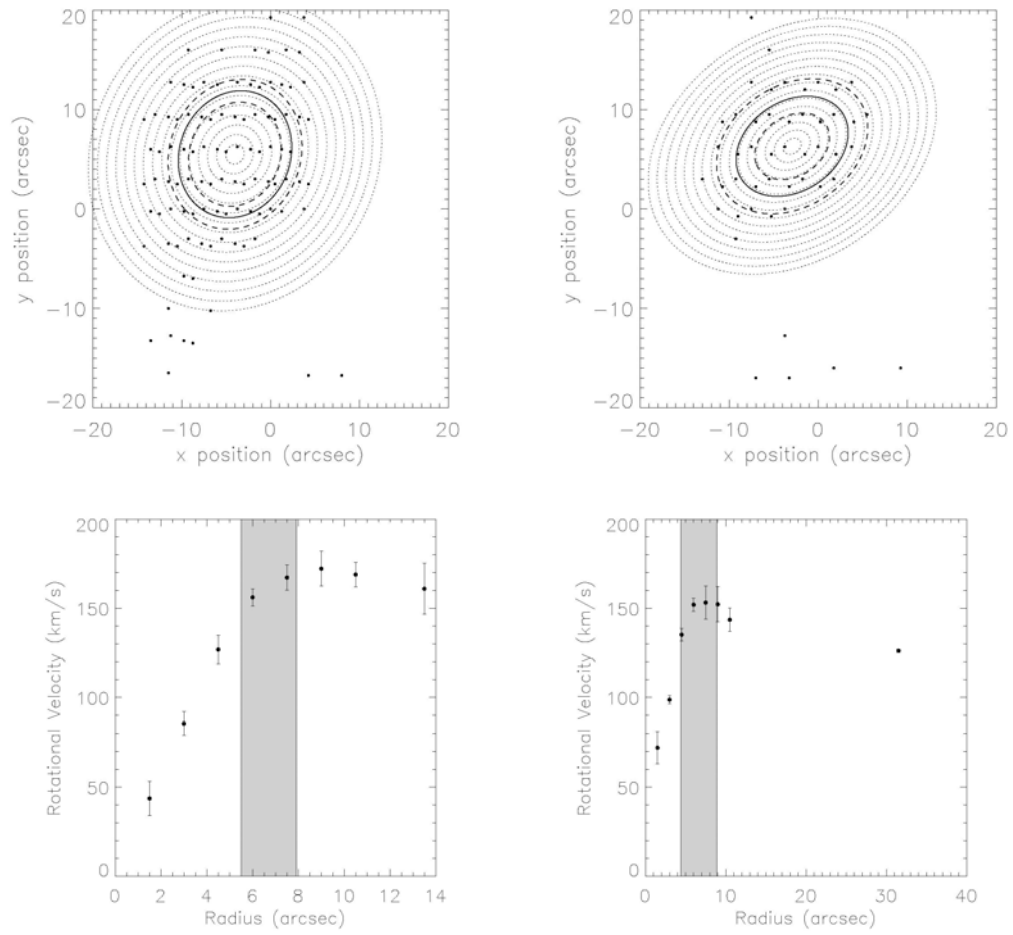


Figure 4.2: Continued. NGC 4314 (left), NGC 5248 (right)

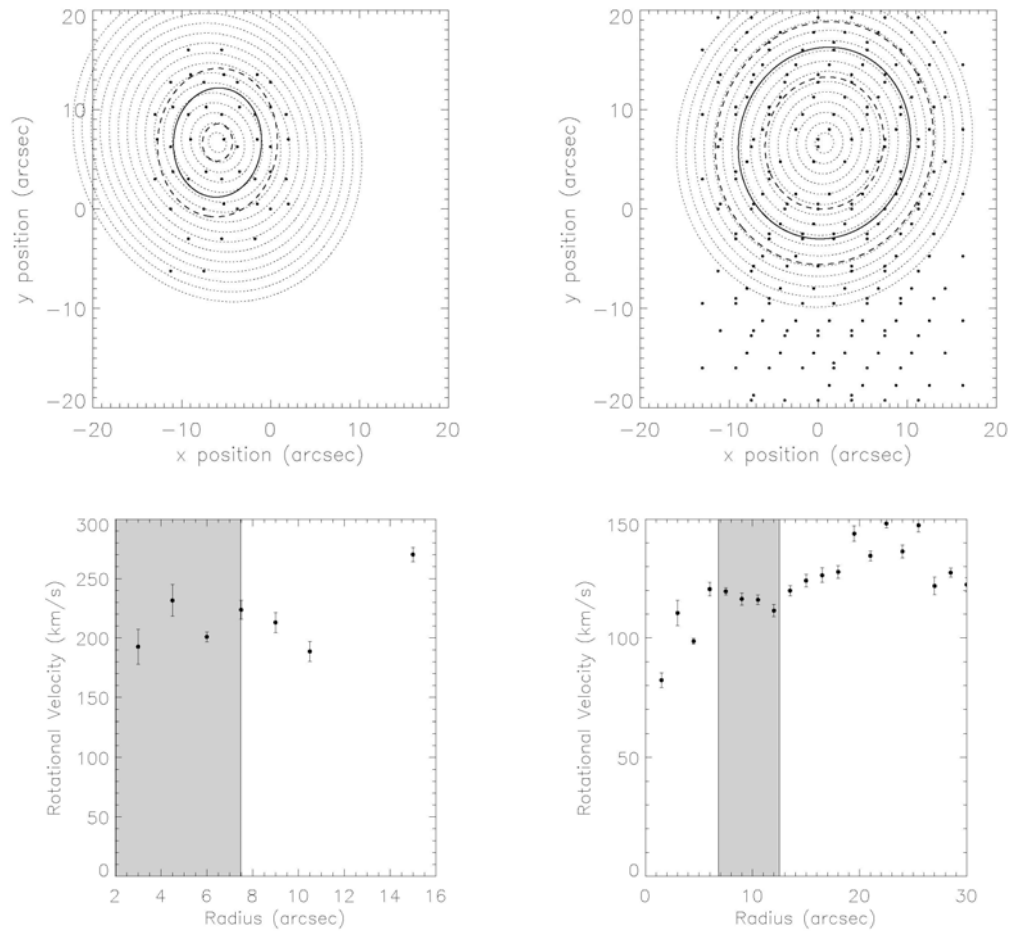


Figure 4.2: Continued. NGC 5953 (left), NGC 7742 (right)

4.4.2 Non-circular Motions

Bars and nuclear rings are known sources of non-circular motions (Buta et al. 1998, Reynaud & Downes, Schommer et al. 1988, Wong & Blitz 2000, Jogee et al. 2002, Regan & Teuben 2003, Zurita et al. 2004 who all studied nuclear rings in barred galaxies). Much attention has been given to the bar, whose easily observed large scale structure can introduce shocks and streaming motions in the gas. Analysis regarding nuclear rings as another major source is less common due to their small size, proximity to the nucleus, and dusty environment encapsulating them. Although the properties of nuclear rings are very different from those of the bar, we can apply the same general process for tracing possible deviations to pure circular motion by dissecting the VF. Diagnostic tools include radial velocity plots and residual maps, which can reveal velocity deviations. Higher-order harmonic expansion of the VF may provide a secondary means of finding smaller-scale perturbations. We utilize all three methods to gain insight into the velocity environment in and locally around the nuclear rings in our sub-sample. Figure 4.3 shows the resulting radial velocity plots, residual maps, and harmonic term curves for each of the seven nuclear rings. We present results of these plots in the following subsections.

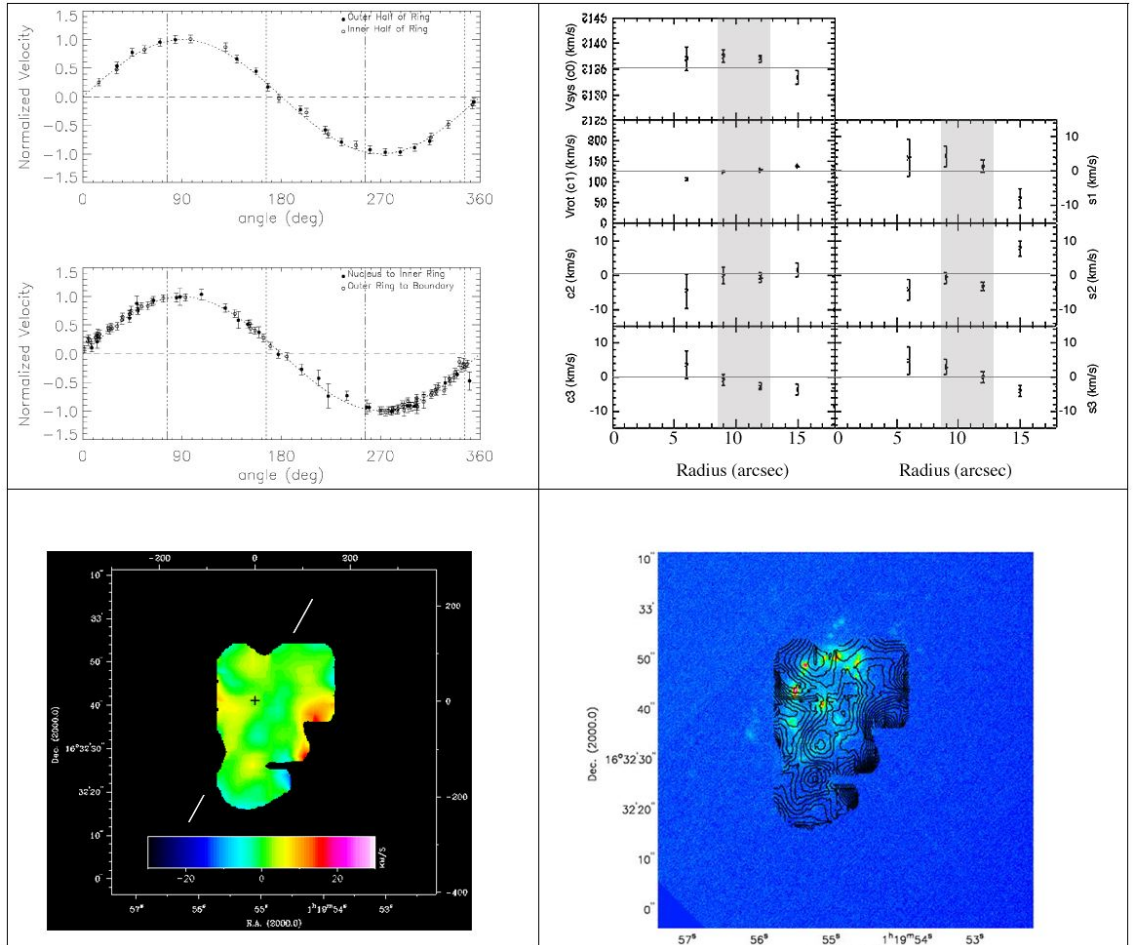


Figure 4.3: (a) NGC 473. The plots in the upper left quadrant show velocities at radii within (top plot) and exterior to (bottom plot) the nuclear ring. The radial coverage within the nuclear ring is further divided to show velocities along the inner half and outer half of the ring. Outside of the nuclear ring, velocities from the nucleus to the ring inner edge, and those from the ring outer edge to the radial limits of the FOV are plotted. All velocities are plotted with respect to the systemic velocity, normalized by the rotation velocity, and adjusted by removing the inclination in order to allow comparison with the curve representing circular motion. The bar major axis (dash-dot lines) and minor axis (dotted lines) are drawn for context. Note that there is a phase shift of 90° , plus the difference between the kinematic PA of the velocity data points and the photometric PA used to create the model curve, to allow the cross-over point to occur at 180° . The upper right quadrant plots the higher-order harmonic expansion of the VF, up to order 3, with the radial region of the ring indicated in the gray zones. The bottom half of the figure plots the velocity residuals, as derived by subtracting a model VF by the observed VF; the residual velocity map is in the lower left quadrant with the ring center and bar major axis marked; residual contours are overlotted on the $H\alpha$ image in the lower right quadrant.

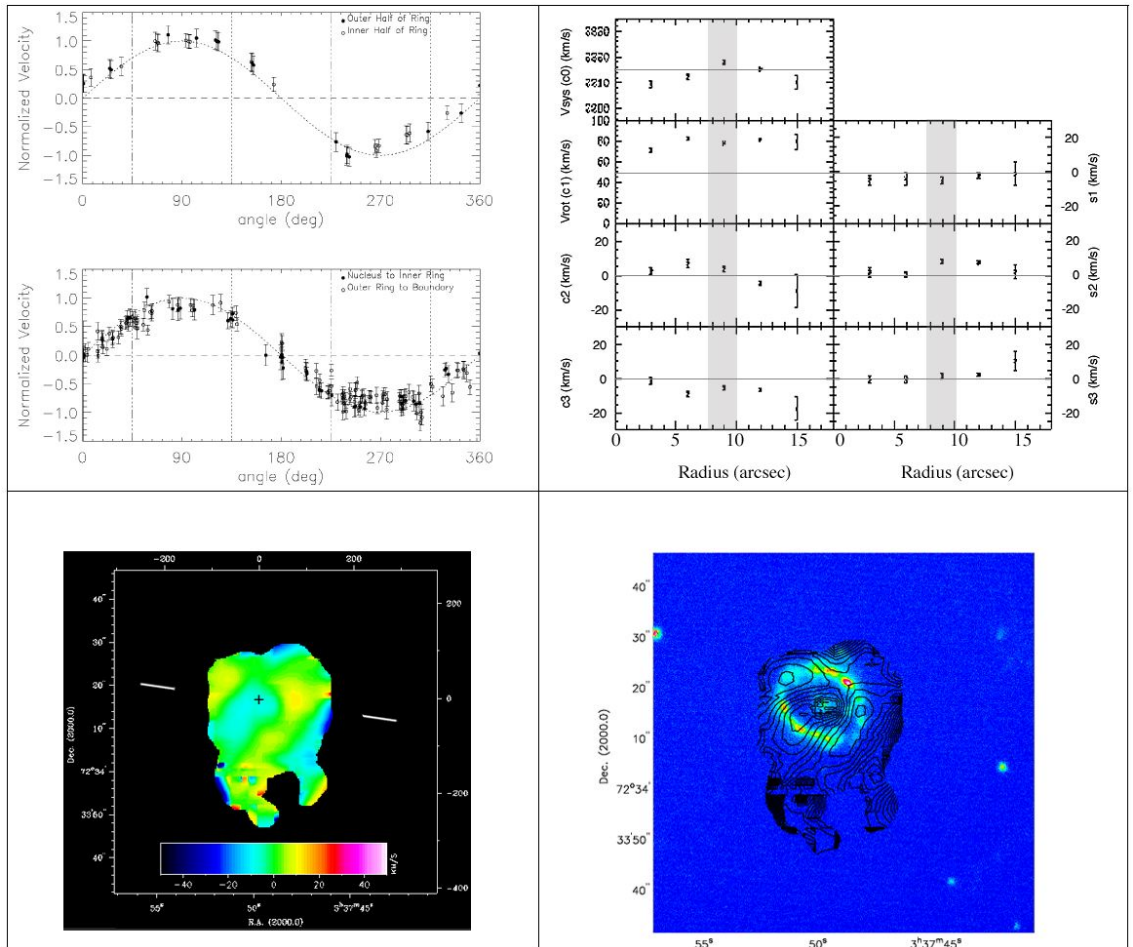


Figure 4.3: (b) NGC 1343. Continued

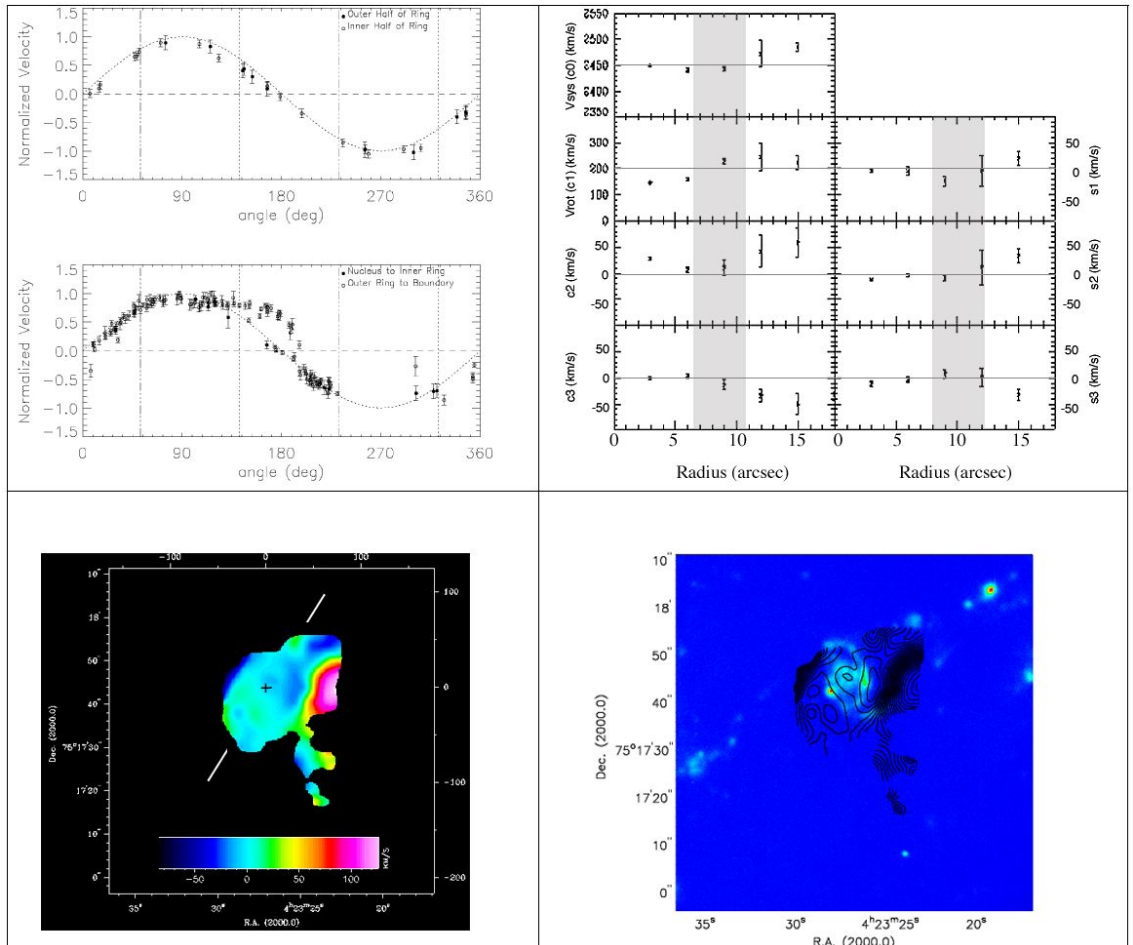


Figure 4.3: (c) NGC 1530. Continued

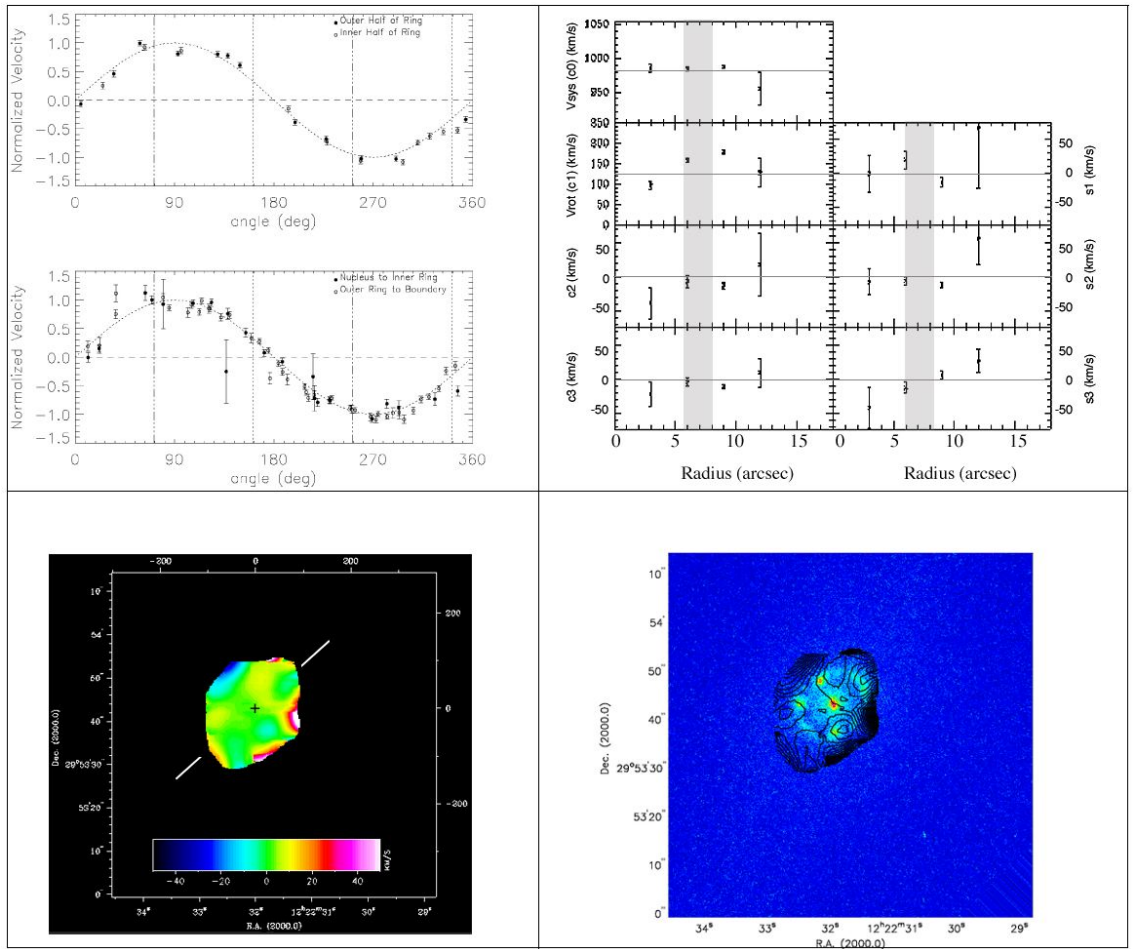


Figure 4.3: (d) NGC 4314. Continued

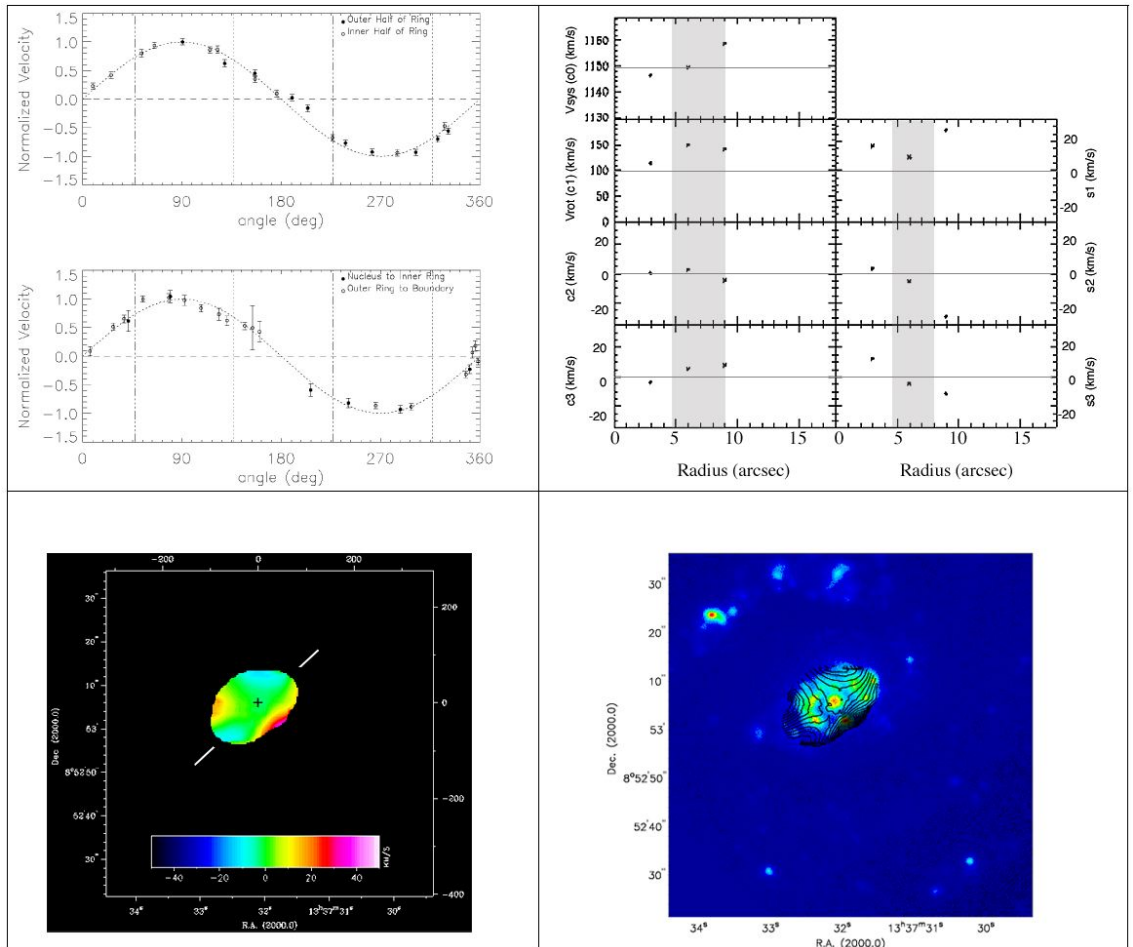


Figure 4.3: (d) NGC 5248. Continued

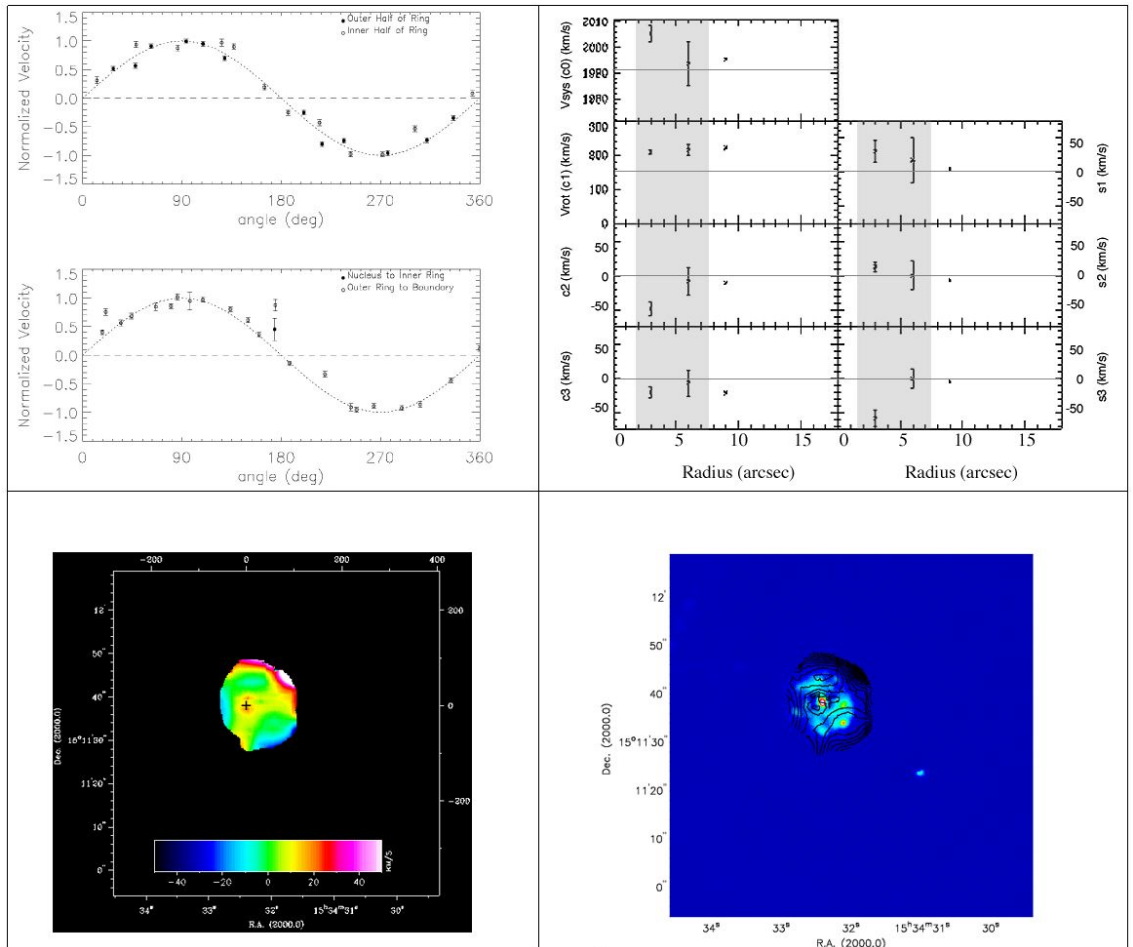


Figure 4.3: (d) NGC 5953. Continued

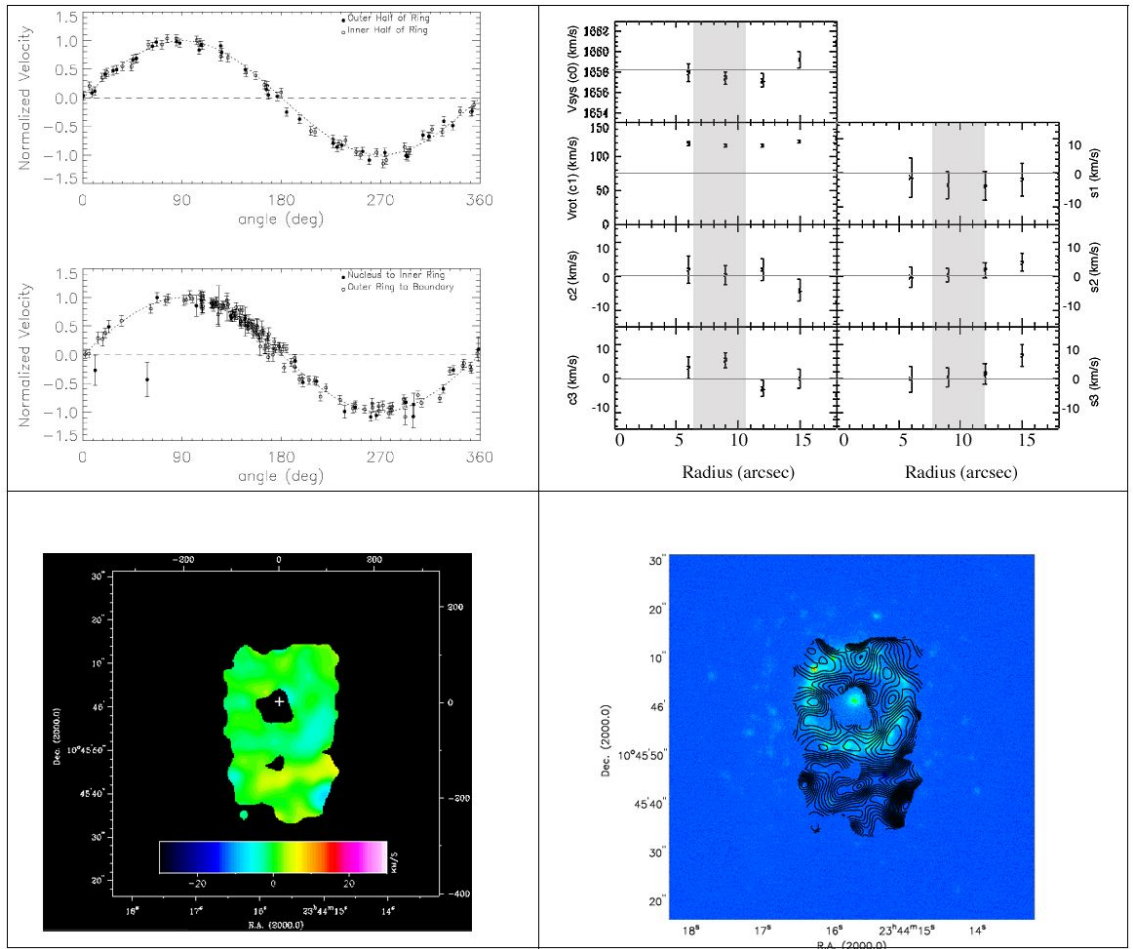


Figure 4.3: (g) NGC 7742. Continued

Radial Velocities

The VF smoothed maps in Figure 4.1 indicate that non-circular velocities may exist in the circumnuclear regions of many of the galaxies in our sub-sample. To better quantify the deviations, Figure 4.3 (upper left quadrant) plots the velocity data as a function of azimuthal position for the radii (1) ranging over each nuclear ring, (2) from the nucleus to the inner boundary of the ring, and (3) from the outer boundary of the ring to all other radii in the FOV. The inner and outer edges of the nuclear ring as seen in the $H\alpha$ image are derived using the IRAF ELLIPSE task, where consecutive concentric isophotes that match the nuclear ring photometric PA and ellipticity (as derived in Chapter 3) are plotted over the full range of the $H\alpha$ image. Boundaries were determined by choosing the isophotes that best matched the inside and outside perimeter of the nuclear ring (see the tilted ring plots in Figure 4.2 for an outline of the ring boundaries, and Table 4.1 for the ring widths). The velocity data points are plotted with respect to the systemic velocity, normalized by the rotation velocity, as a function of the ring kinematic PA. We overplot a 'model' curve for pure circular motions and indicate the bar major and minor axes to search for possible velocity transitions near those locations radially across the ring.

Uncertainties associated with the measured velocity, wavelength calibration, and position of the $H\alpha$ peak within a given fiber beam were added in quadrature. The measured uncertainties range from 0.5 km s^{-1} to 5 km s^{-1} , with uncertainties in wavelength calibration near the $H\alpha$ line at $\sim 1.5 \text{ km s}^{-1}$. To compute the uncertainties of the location of the $H\alpha$ peak within the $3''$ fibers, we use the RC to measure

the velocity gradient across a fiber, for all fibers in the array. We adopt a value of 8 km s^{-1} to be representative of a 1σ uncertainty with respect to systemic velocity, which is assumed to be at the center of a fiber. The uncertainty does vary from fiber to fiber, however, since the rotational velocity changes across the radial range of the FOV. For steeper velocity gradients, the uncertainty in the fiber center will be higher as compared to flatter gradients. The uncertainty of the $\text{H}\alpha$ emission peak is also a function of the PA, where the velocities along the major axis will contribute more to the uncertainty versus velocities along the line-of-sight (i.e, minor axis).

Within the nuclear rings, we find no cases that show strong (i.e., greater than the systematic scatter around the model curve) departures from circular motion. Non-circular motions are, however, evident near the ring outer boundary in three cases. Velocities azimuthally located between the bar major and minor axes of NGC 1530 (PA = 135° to 190° on the azimuthal plot) are the largest of the sub-sample, with deviations reaching 120 km s^{-1} . This is consistent with the results of Zurita et al. (2004) and will be discussed further in Section 4.2.2 and Section 4.5. NGC 4314 and NGC 5953 show deviations (up to 60 km s^{-1} , and 50 km s^{-1} , respectively) exterior to the outer boundary of the nuclear ring near PA = 36° and PA = 175° , respectively, although signal-to-noise is low (i.e, the number of data points sampled in these regions are low).

Residual Velocity Maps

To construct the residual velocity map of each circumnuclear region, we first build a two-dimensional model VF based on the RC and tilted ring values. We use the GIPSY task VELFI to construct the kinematic model from the RC parameters PA , i , V_{sys} , and the rotation center position. These inputs are used in conjunction with the rotational velocities for the radii at which the RC is measured. The model is subtracted from the VF to obtain the residual velocity map. The map and residual contours superimposed on the $H\alpha$ image of the nuclear ring are shown in Figure 4.3 for the sub-sample of seven rings. Again, as with the VF smoothed maps, the contiguous residual maps should only be used for general impressions, since the results may be affected by the interpolation effects. These maps, however, provide more radial information and give a better sense of patterns in the image. Any quantitative interpretation comes from the sparse residual maps, which have no interpolation of the data points.

We find that all of the nuclear rings in our sub-sample have low residual velocities (both approaching and receding) near the central ridge of the ring (averaging from $\sim 5 \text{ km s}^{-1}$ to $\sim 20 \text{ km s}^{-1}$). The nuclear rings in NGC 473 and NGC 7742 are not well resolved enough to comment on here, as their associated residuals are $\sim 5 \text{ km s}^{-1}$, which do not overcome the uncertainties. Patches of approaching and receding residual velocity peaks of $\sim 10 \text{ km s}^{-1}$ occur in the nuclear rings of NGC 1343, NGC 4314, and NGC 5953, and reach to near 20 km s^{-1} in the rings of NGC 1530 and NGC 5248. Since these values are close to the combined measurement uncer-

tainty, we can only state that the residuals seen within the nuclear rings are upper limits.

Sufficient, albeit marginal, $H\alpha$ radial coverage allows us to comment on the velocities of the barred galaxies near the ring outer edge perpendicular and parallel to the bar major axis. For NGC 4314, we see ordered velocity patterns increasing near the outer edge of the ring (both approaching and receding) close to both sides of the bar minor axis, where the bar dust lanes merge with the ring. Residuals approach 60 km s^{-1} in both directions, with a strong velocity transition zone near the ring outer boundary, where values reach 90 km s^{-1} (approaching) at the FOV edge. Although the spatial sampling is poor at the image edge, our observations do agree with those from Benedict et al. (1996; see Section 4.5 for further discussion). Residuals for NGC 5248 near the western side of the bar minor axis reach 40 km s^{-1} , with a weaker-defined, although evident, transition zone as radii approach the outer ring boundary. These results are consistent with the two-dimensional CO VF maps in Jogee et al. (2002; see Section 4.5). In both galaxies, good agreement with the literature adds confidence that, although our data are spatially sparse, the results we see at the field edges are not artificial.

The map of NGC 1530 provides us with the clearest picture of the interaction between the bar and the ring. We see large velocity excesses ($\sim 110 \text{ km s}^{-1}$) to the west of the nuclear ring, near its exterior edge. The high residuals are associated with the large scale bar present at $PA = 164^\circ$ (see Zurita et al. 2004 for a fuller discussion of the kinematics within and near the bar). The strong residuals sharply decrease to 50 km s^{-1} over a small transition zone near the ring outer boundary.

Harmonic Analysis

We apply an independent method for measuring non-circular motions of the gas in a VF distribution via higher-order velocity harmonics. The observed potential can be obtained by adding the individual harmonic terms to an unperturbed potential, where each harmonic component is considered to be small compared to the unperturbed potential. We use the method described in Schoenmakers et al. (1997) and executed in the GIPSY RESWRI task. The procedure first derives the kinematical parameters from the observed VF by fitting tilted-rings (via the same algorithm we used to create the RC - see Section 4.1 for details) to the observed VF and adjusting the kinematic parameters simultaneously (i , PA, and V_{sys}) as a function of radius. The kinematic center is fixed so as not to obscure any true lopsidedness in the kinematics, which reveal themselves in the same way as a drifting center would. We set the program to run for an order = 3, where it produces amplitudes and phases associated with the harmonic expansion of the radial VF for each of the orders along concentric radial rings. By solving the equations of motion for a potential perturbed by a single harmonic component, the line-of-sight velocity can be written as:

$$v_{los} = v_{sys} + \sum_{n=1}^k \hat{c}_n \cos(n\hat{\psi}) + \hat{s}_n \sin(n\hat{\psi}) \quad (4.2)$$

where k is the order of the fit, ψ is the azimuthal angle measured in the plane of the orbit describing the potential, and \hat{c}_n and \hat{s}_n are expressed in terms of the kinematic parameters. Schoenmakers et al. (1997) show that the line-of-sight VF also has the form:

$$v_{los} = [c_1 \cos \psi + s_{m-1} \sin(m-1)\psi + c_{m-1} \cos(m-1)\psi + s_{m+1} \sin(m+1)\psi + c_{m+1} \cos(m+1)\psi] \quad (4.3)$$

From the equation, one can see that if the potential has a perturbation of harmonic mode number m , the line-of-sight VF will contain an $m - 1$ and $m + 1$ harmonic term. In terms of the above equation, if perturbations exist in the even harmonic mode $m = 2$, for example, we would then expect to see strong effects in the odd amplitude coefficients, \hat{c}_1, \hat{s}_1 and \hat{c}_3, \hat{s}_3 . Overall, perturbations seen in $m = 1$ may represent lopsidedness in the potential, where $m = 2$ can indicate an elongation in the potential as a result from possibly a spiral density wave or a bar.

In fitting the line-of-sight VF, we chose tilted ring increments of $3''$ to ensure that the equation is not under-determined (i.e, the equation has enough data points in a given tilted ring to determine a unique solution), while properly constraining the higher order terms. Expansions of orders larger than our chosen value of 3 would most likely be negligible given our low spatial resolution. Figure 4.3 (upper right quadrant) plots the harmonic coefficient terms up to order 3. For all galaxies, the strengths of the amplitudes in the harmonic terms coincide with the velocity range seen in the azimuthal plots and residuals maps (also shown in Figure 4.3). The strongest amplitudes seen correspond to the outer radial regions of NGC 1530 and NGC 4314, where the bar begins. Conversely, we also see that the strengths of the amplitudes in the harmonic plots are low within the radial range of the nuclear rings. This is a nice consistency check to the velocity plots and residual maps, and adds validity to our interpretations, as discussed in Section 4.5.

We find some evidence of harmonic perturbations over the $\text{H}\alpha$ FOV of up to order $m = 3$ for a few of the galaxies, although the trends are again associated more with the bar location than the nuclear ring. With an $m = 1$ perturbation, the fluctuations in the systemic velocity term, \hat{c}_0 , should be comparable in magnitude to that of the \hat{c}_2 and \hat{s}_2 terms. We see this trend for NGC 1343 and NGC 1530, although the coefficient terms increase in strength near radii associated with the location of the bar. Perturbations which can be due to elongation (i.e., $m = 2$ and $m = 3$) are seen only for the outer radial regions of NGC 473, NGC 1343, and NGC 1530, where the amplitudes in the \hat{c}_2 , \hat{c}_3 , \hat{s}_2 , and \hat{s}_3 terms are strongest near the radial location of the bar. Elongation can also be denoted by a change of sign, as a function of radius, in the \hat{s}_1 and \hat{s}_3 terms. Poor sampling outside of the nuclear rings near the radial location of the bar inhibits us from noting any strong trends. We see no such patterns within the nuclear rings.

4.4.3 Velocity Dispersion

To more accurately analyze the dispersion due to random motions within an H II region, we take into account the instrumental broadening, which is the dominant contributor to the broadening of the $\text{H}\alpha$ line shape. Although we correct the dispersion maps only for instrumental broadening, we understand that the gradient of the velocity across a given fiber can also cause broadening of the $\text{H}\alpha$ line. In Section 4.2.1, we calculated the gradient to generally be 8 km s^{-1} . This is dependent on the velocity gradient and PA, and will obviously differ for each galaxy. Other

physical factors include the natural line broadening of Hydrogen, and the thermal broadening (the Doppler broadening of the emission line from an H II region), which are inconsequential when compared to our instrumental dispersion and the uncertainties associated with it. We therefore adopt the following equation to obtain the first-order intrinsic dispersion, σ_i :

$$\sigma_i = (\sigma_{obs}^2 - \sigma_{inst}^2)^{1/2} \quad (4.4)$$

where σ_{obs} is the observed measured dispersion and σ_{inst} is the instrumental dispersion ($\sigma_{inst} = 18.7 \text{ km s}^{-1}$ for the December 2003 run and $\sigma_{inst} = 25.5 \text{ km s}^{-1}$ for the April 2004 run).

We subtracted the instrumental broadening in quadrature from the given data point, and obtained a new dispersion map. In the cases where data points were unresolved, we set a lower limit of 18.8 km s^{-1} (December 2003 run) and $\sigma_{inst} = 25.6 \text{ km s}^{-1}$ (April 2004 run) for the observed dispersion before performing the subtraction. The corrected dispersion map for each galaxy in the sub-sample is shown in Figure 4.4.

The dispersion values within the nuclear rings range from $\sim 20 \text{ km s}^{-1}$, in the case of NGC 473, NGC 4314, NGC 5248, and NGC 7742, to 40 km s^{-1} - 50 km s^{-1} for NGC 1343 and NGC 1530, and NGC 5953. The lower dispersions are consistent with flat RCs near the location of the nuclear rings, which we see in Figure 4.2; the converse is true for those galaxies with higher dispersions, although the gradient flattens towards the outer half of the ring in NGC 5953. The range of dispersions is comparable with that seen in other nuclear ring studies (e.g., Rozas et al. 1998

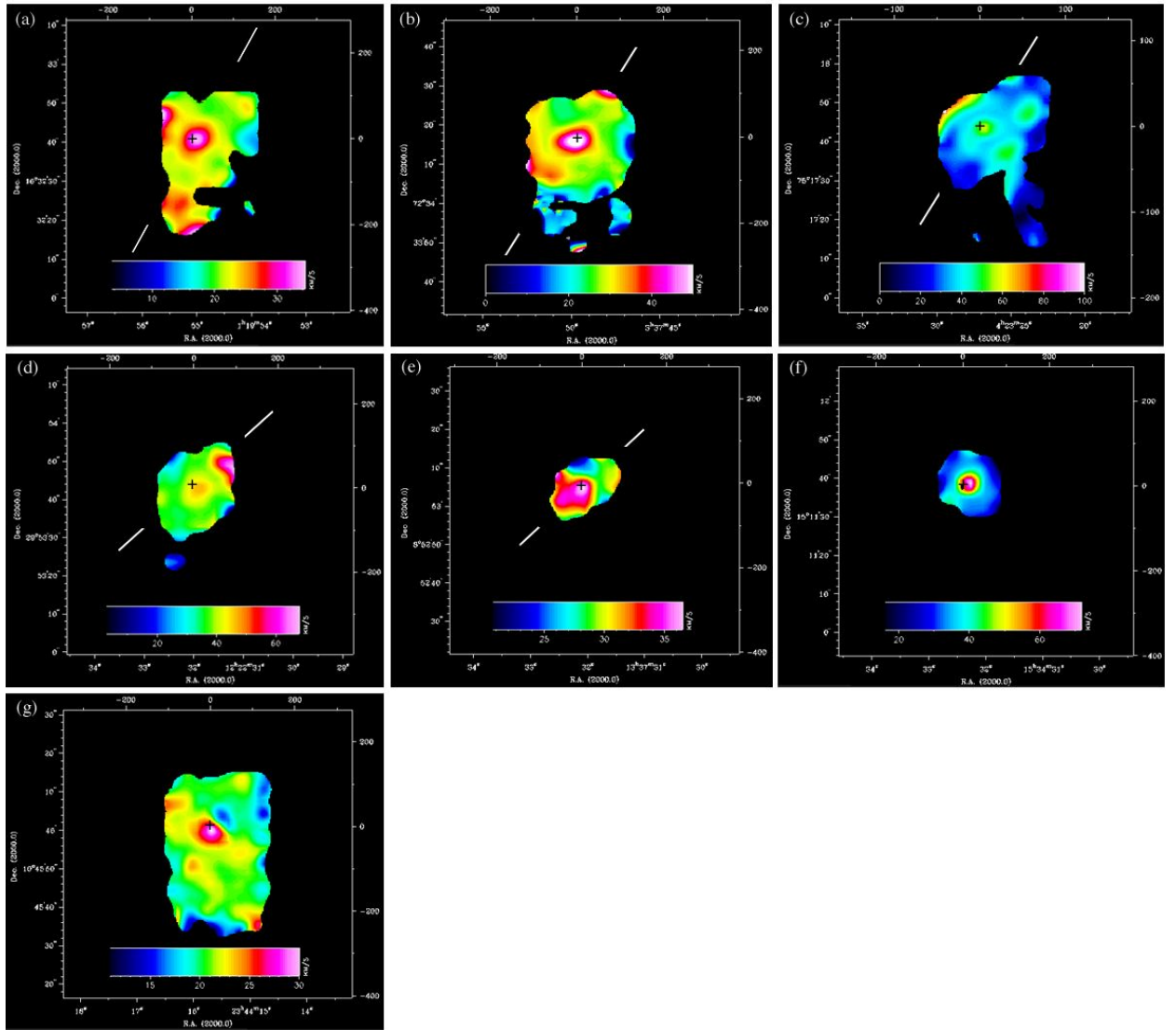


Figure 4.4: Dispersion maps of the sub-sample, corrected for instrumental broadening. Crosses and hash marks indicate the center and bar major axis, respectively. The sub-sample is (a) NGC 473, (b) NGC 1343, (c) NGC 1530, (d) NGC 4314, (e) NGC 5248, (f) NGC 5953, (g) NGC 7742.

for NGC 4321; Zurita et al. 2004 for NGC 1530). Because of our limited FOV it is difficult to elaborate on the dispersion environment outside of the nuclear rings.

4.5 Discussion

4.5.1 Non-circular Motions and Kinematics within Nuclear Rings

Variations between the disk and nuclear ring PAs, as well as the ring kinematic and photometric PAs, can be tracers of non-circular motions. In Figure 4.5, we compare the PAs of the ring kinematic and photometric major axes, the ring kinematic and disk photometric major axes, and the ring and disk photometric major axes, respectively. The plots show a general linear relationship between the various PAs, with a few exceptions, which we address later in this section. The strong agreement between the ring photometric and galaxy disk PAs is reinforced in Chapter 3 (Figure 3.2) by a similar result for a comparison of 22 nuclear rings, which includes those in this sub-sample. In the $H\alpha$ imaging study, we compare the PA and ellipticity of the rings to that of their host disk, and find an equivalent relationship between the nuclear rings and their disk for both morphological parameters. We claimed that the nuclear rings that follow this pattern are in the same plane as the disk, and are circular.

The kinematic results from Section 4.4 add more weight to the idea that nuclear rings are round since we only see small non-circular motions within in the rings. The azimuthal plots, along with the residual maps (Figure 4.3), show an upper residual limit of 20 km s^{-1} within the rings, with all but two nuclear rings containing

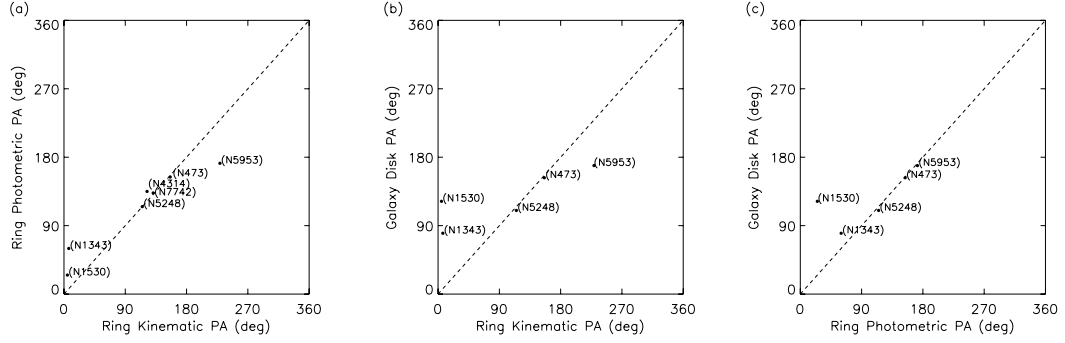


Figure 4.5: PA comparisons for (a) kinematic vs. photometric, (b) kinematic vs. disk, and (c) photometric vs. disk, respectively. The plots show a linear relationship between the various PAs, as denoted by the dashed line for $y = x$. The disk PA is undefined for NGC 4314 and NGC 7742.

deviations of most 10 km s^{-1} . Further, harmonic expansion of the VF shows no clear signs of secondary perturbations to the galactic potential within the nuclear rings, but this is not surprising as the measured deviations in the first-order residuals are already low and near the limit of the measured uncertainties. The small departures from circular motion that we see within the rings may indeed be enough to disturb the local underlying potential within the rings (as noted for NGC 4321, Knapen et al. 1995; NGC 1068, Schinnerer et al. 2000; and NGC 5383, Duval 1977, Sheth et al. 2000) but apparently not substantial enough to cause measurable distortions in the shape of the rings with any certainty.

We also show that this is the case for those nuclear rings that do not conform to the linear pattern seen in Figure 4.5. In three cases there is a noticeable difference between the kinematic PA and the respective photometric and disk PAs. NGC 1343, NGC 1530, and NGC 5953 show deviations ranging from 20° to 57° (see Table 4.2, col. 5 and also the tilted ring plots in Figure 4.2), with even larger deviations when their kinematic PA is compared to that of the disk. Such differences can indicate

that (1) the nuclear ring is not in the same plane (or oriented the same way) as the disk, or (2) the nuclear ring is not circular. For all nuclear rings in this sample, the kinematics reveal that deviations to circular motion are small, which indicates general symmetry in the potential, and thus circular rings.

As an added check, we searched for signs of lopsidedness within the nuclear ring by comparing the kinematic and photometric centers. Strong amplitudes in the \hat{c}_2 and \hat{s}_2 terms can indicate the center of the VF does not coincide with the optical center of the galaxy (e.g., Franx et al. 1994). We find no such pattern near the location of the nuclear rings in question. Indeed, after computing the difference between the kinematic and photometric center positions (see Table 4.2), we see that the center offsets agree to within the uncertainties of the photometric center measurements. We claim that these nuclear rings exhibit no clear signs of lopsidedness or elongation, and thus, no strong deviations to circular motion. The ring ellipticities (Figure 3.2b) are comparable to that of the disk, which implies the rings are in the same plane. This leads to the subsequent conclusion that these rings are circular, coplanar, but not oriented the same as the disk. For NGC 1343 and NGC 1530, the PA offset may be related to the strength of the bar, the angle at which the dust lanes intersect with the bar, or the inflow rate (which proved inconclusive in Chapter 3). Further interpretation of these possible contributors is not possible due to the limited FOV. The offset in NGC 5953 is most likely due to the interaction with the companion galaxy NGC 5954.

4.5.2 Non-circular Motions vs. Luminosity, Dispersion, and Star Formation

Nuclear rings are locations of H II regions, as can be traced by the H α line. Figure 4.6 shows the H α emission across the FOV, and confirms that the strongest emission is in the nuclear rings and active nuclei. In Chapter 3 we showed that nuclear rings are comprised of several distinct young massive star-forming H II regions, each with luminosities of order 10^{40}erg s^{-1} . We compare the luminous H II regions, as seen in H α , to the corrected dispersion maps whose values range from $\sim 20\text{ km s}^{-1}$ to $\sim 50\text{ km s}^{-1}$ (see Section 4.3; Figure 4.4), and find that the low dispersions seen throughout the rings coincide with the presence of strong H α emission and young luminous stars. Figure 4.7 plots the total luminosity in the nuclear rings versus the average dispersion and shows the low dispersion seen in our sample to be indicative of stars whose luminosities range from 10^{40}erg s^{-1} to 10^{42}erg s^{-1} . The low dispersions are also correlated spatially with the strong H α emission seen within the nuclear rings and active nuclei. We are unable to further discriminate between the individual H II regions, as dispersions are fairly uniform throughout the rings. The low dispersions are indicative of regions with cool gas (low random motions) that allow the triggering of star formation. Although our FOV is too restrictive to comment directly on the dispersions in the bar dust lanes, Zurita et al.(2004) and Allard et al.(2006) reveal that dispersions are also low, which is consistent with the idea that cool gas is continually flowing into the nuclear rings, via the dust lanes, and replenishing the gas.

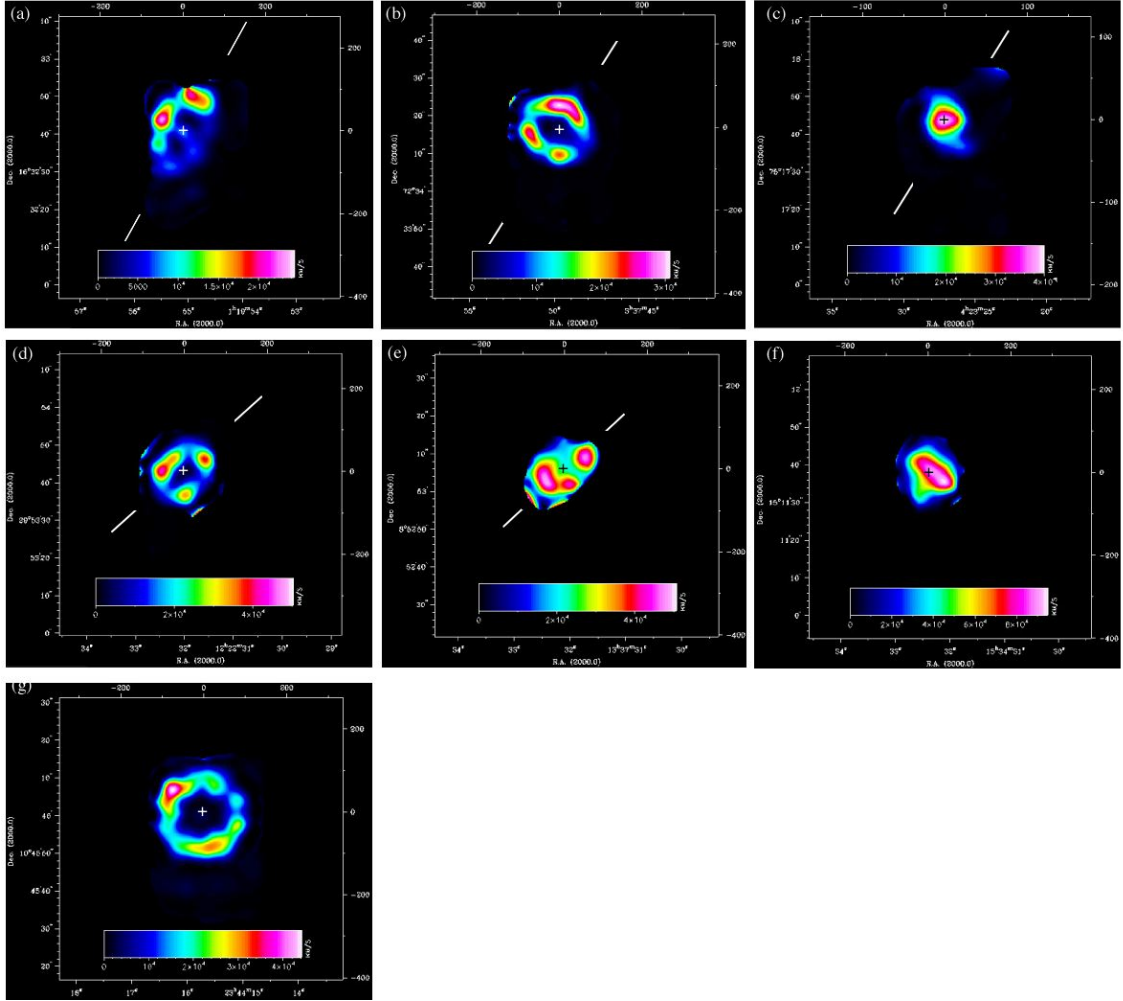


Figure 4.6: $H\alpha$ emission line maps. Crosses and hash marks indicate the center and bar major axis, respectively. The sub-sample is (a) NGC 473, (b) NGC 1343, (c) NGC 1530, (d) NGC 4314, (e) NGC 5248, (f) NGC 5953, (g) NGC 7742.

In the cases of the non-barred galaxies, NGC 5953 and NGC 7742, the dispersions are also low, with high luminosities in the nuclear rings, yet there are no strong bars apparent. For NGC 5953, González Delgado & Perez (1996) confirm the high luminosity and strong presence of high-mass star formation and state that this is probably a result of the interaction with the companion galaxy NGC 5954, which is fueling the central regions of NGC 5953. Their line ratio analysis shows

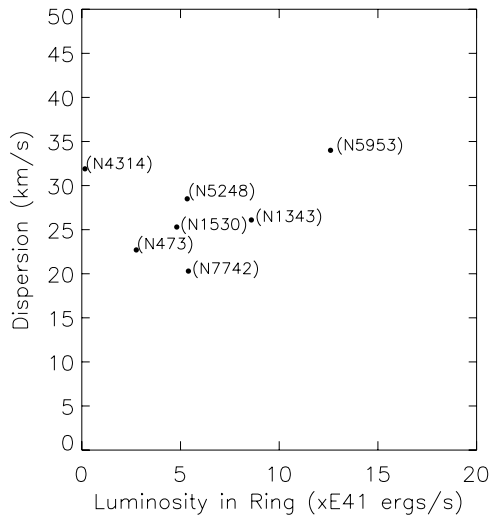


Figure 4.7: The average dispersion (corrected for instrumental broadening) within the nuclear rings is plotted against the total luminosity (see Appendix A for luminosities). No correlation exists between the small range of dispersions and the ring luminosity.

high excitation throughout the nuclear region, but even higher excitation and higher density in the south-east section of the circumnuclear region, which is ionized by a cluster of stars with an effective temperature of $\sim 42 \times 10^3$ K. This is consistent with our findings of low velocity dispersions in the same region. NGC 7742 exhibits similar low dispersions and high luminosities in the nuclear ring. As we'll see in the next chapter, NGC 7742 shows clear signs of past galaxy interaction, as indicated by opposing directional flow of the stars and gas. One scenario is that NGC 7742 cannibalized a smaller galaxy, rich in gas of low metallicity. This material was then funneled in the ring and triggered star formation.

4.5.3 Non-circular Motions, The Bar, and x_2 Orbits

Nuclear rings reside in the interface region between the x_1 and x_2 family of orbits. The x_1 elongated orbits, which support the bar, gradually transition to x_2 orbits, which lie interior to the bar and perpendicular to the bar major axis. For all of the barred galaxies in our sub-sample, we find a connection between the bar, the x_2 family of orbits, and the nuclear ring. The strongest indicator is the association between the largest velocity deviations from circular motion just near the exterior edge of the rings, and the location of the bar minor axis projected onto the rings. Our results are consistent with models and observations. The models presented by Knapen et al. (1995), Heller & Shlosman (1996), and Regan & Teuben (2003) characterize the velocity environment along the outer edge of rings at the bar major and minor axes. Simulations show that gas follows the x_1 family of orbits, and loses angular momentum as it flows radially inward, causing the gas to significantly slow, and accumulate near the transitional boundary of the x_1 and x_2 orbits. A nuclear ring is formed when a threshold amount of the phase space is occupied by the x_2 orbits.

The nuclear ring interacts with the bar via the dust lanes, which merge with the ring along its minor axis. Kinematic simulations of the gas in nuclear rings show that the strongest velocity transitions occur at the location of the nuclear ring along the bar minor axis. This is the case, observationally. NGC 4314 shows non-circular motions near the bar minor axis along the outer ring edge and extending radially outwards towards the bar. The scatter appears symmetric along the inner and outer

halves of the ring. We also find strong residual velocities near the outer edge of the ring on the west side (along the minor axis), where velocities just within the ring but near the outer edge are $\sim 20 \text{ km s}^{-1}$ and quickly increase to $\sim 90 \text{ km s}^{-1}$ just outside of the ring. Although these residuals exist near the edge of our $\text{H}\alpha$ coverage, the deviations from circular motion near the bar minor axis are consistent with the CO velocity and residual maps from Benedict et al. (1996), who state comparable values. They claim that the largest deviations from circular motion occur in two symmetrically located regions just outside of the ring and near where the dust lanes merge with the ring (i.e., where the x_1 orbits transition to the x_2 family). Based on the assumptions that the dust lanes are along the leading edge of the bar, and the spiral arms are trailing, Benedict et al. state that the residual velocities imply inflow from the dust lane to the nuclear ring.

The residual map for NGC 5248 indicates relative velocities that reach 40 km s^{-1} along the minor axis at the outer edge of the nuclear ring that are noticeably stronger than those velocities along the major axis through the ring, which average $\sim 5 \text{ km s}^{-1}$. Again, we are cautious to conclude that these residuals are directly associated with the bar, as our data are near the edge of the measured field. However, CO analysis from Jogee et al. (2002) confirms streaming motions of $25 - 40 \text{ km s}^{-1}$ along the minor axis, with the isophotes changing gradually from being oriented along the bar major axis to being perpendicular to the bar around $35''$, which does not violate our results.

Although we see no obvious residual patterns near the bar major or minor axes of the nuclear ring for NGC 1530, we note the largest residual velocities

($\sim 120 \text{ km s}^{-1}$) seen in our sub-sample between the bar major and minor axes, just exterior to the ring outer boundary, on the west side. Zurita et al. (2004) observe a nearly identical pattern in their $\text{H}\alpha$ map of the circumnuclear environment, which includes the entire bar. We find a very sharp transition at the location of the nuclear ring, where residual velocities drop to 10 km s^{-1} . This too is consistent with Zurita et al. (2004) who claim that the nuclear ring is acting as a “brake”, where it switches the direction of flow of the gas from nearly along the bar (i.e., along x_1 orbits) to nearly perpendicular (along the x_2 orbits).

4.6 Summary

Utilizing IFU spectra with high velocity resolution, we reveal systematic patterns, as seen in $\text{H}\alpha$, in and around nuclear rings. Residual velocities are low within nuclear rings, which are indicative of a non-turbulent environment. We place an upper limit on velocity deviations within nuclear rings to be 20 km s^{-1} , where star formation can flourish without the presence of strong shocks and shears within the ring. Of the barred galaxies in our sample, the outer boundary of the nuclear ring is delineated by a thin shell of increased velocity gradients, with the strongest velocity transitions existing across the outer edge of the nuclear rings, along the bar minor axis. Higher-order expansion of the VF shows trends that are seen along the ring exterior boundary, near the location of the bar. The density modes $m = 1$ to $m = 3$ are seen just outside the nuclear rings for three cases, which confirms elongation of the potential (the influence of the bar); no such perturbations are seen within any

of the nuclear rings. Although spatial information outside of the nuclear rings is limited and subject to low signal-to-noise, our results are in good agreement with those cited in the literature.

Within the nuclear rings, dispersions are comparably low and range from 20 km s^{-1} to 50 km s^{-1} . The low dispersions and residuals correlate spatially with the strongest $\text{H}\alpha$ emissions and high luminosities in the nuclear rings and those galaxies that contain active nuclei. This scenario implies that the gas is cool in the rings (of order 10^3 K) and relatively non-turbulent, which allows star formation to ignite. Literature on the nature of bars reveals that this cool gas emanates from the bar dust lanes. Thus, the dust lanes are most likely the major source of continual inflow of the cool gas into these rings, although expansion of the FOV is necessary to confirm this hypothesis. The lower dispersions also correspond to flatter RCs near the location of the nuclear rings. The fairly uniform range of dispersions seen in the rings provides no further insight into the varying total luminosities ($10^{40} \text{ erg s}^{-1}$ to $10^{42} \text{ erg s}^{-1}$) of the nuclear rings or the individual H II regions comprising them.

Kinematic analysis, combined with $\text{H}\alpha$ imaging data, indicates that nuclear rings are circular and typically in the same plane as the galaxy disk. Large offsets between the ring kinematic and photometric PAs for three cases are attributed to complex interactions with the bar or, in the case of NGC 5953, with a merging galactic system.

Chapter 5

The Physical Conditions of the Ionized Gas in the Central KiloParsec of NGC 7742

(to be submitted as a letter to the Astrophysical Journal, July 2006)

5.1 Overview

Line emission from galaxies is produced by gas heated and ionized by hot OB stars, AGN, or shocks. In H II regions, ionization is traced by Balmer lines (e.g., $H\alpha$, $H\beta$), which dominate the optical spectra as hydrogen near massive young stars is ionized. AGN activity, in particular at low-luminosities, is often characterized by Low Ionization Nuclear Emission-line Regions (LINERs, Ho et al. 1997), with strong low-ionization emissions from forbidden lines of the ions of heavy elements such as S, N and O (Heckman 1980). LINER-like emission is also observed often outside galactic nuclei, where shocks are a likely source of excitation (Filippenko 1996).

To help interpret the spectral properties of massive star forming regions and to recognize the role of the various excitation mechanisms, one can utilize diagnostic diagrams. For instance, Veilleux & Osterbrock (1987; hereafter VO87) introduced a diagnostic analysis that is independent of reddening and is based on the ratios of strong emission lines rather close in wavelength. Kewley et al. (2001a; hereafter

K01) expand upon the VO87 analysis by incorporating in their photoionization code the spectral energy distributions of young stellar clusters predicted by stellar population synthesis models (Starburst 99, Leitherer et al. 1999; PEGASE, Fioc & Rocca-Volmerange 1997). The model grids produced can discriminate reliably between galaxies hosting an AGN or a nuclear starburst, and in the case of H II regions, can constrain the metallicity of the starburst and the strength of the ionizing radiation relative to the electron density (i.e. the ionization parameter).

NGC 7742 is a face-on SA(r)b LINER galaxy, whose morphology is dominated by a prominent nuclear ring with a radius of 10 arcsec or 1.0 kpc (Mazzuca et al. 2006 - Chapter 3). The ring is lined with H II regions that emit strongly in H α (Pogge & Eskridge 1993; Crocker, Baugus & Buta 1996; Mazzuca et al. 2006 - Chapter 3) but the H α emission equivalent widths of the H II regions show no evidence for age gradients, indicating random star formation (Mazzuca et al. 2006 - Chapter 3). According to the Palomar survey (Ho et al. 1997) the nucleus of NGC 7742 is classified as a T2/L2 intermediate type, meaning that in the central 150pc the emission is characterized by low-ionization lines but also that some star formation may be on-going. The galaxy is classified as non-barred, but from *HST* imaging Wakamatsu et al. (1996) show that a weak central oval is present, while Laine et al. (2002) find two distinct weak bars, with deprojected semi-major axes 1.2 and 6.8 arcsec (corresponding to 130 and 730 pc), respectively.

The galaxy is not obviously interacting at the moment, but may well form a pair with NGC 7743, which is 50 arcmin (320 kpc) away but within 50 km s⁻¹ in radial velocity. De Zeeuw et al. (2002, hereafter deZ02) show that the gas

is counterrotating with respect to the stars within the entire field of the SAURON observations (see also Falcón-Barroso et al. 2006 and Sil’chenko & Moiseev 2006). This indicates a recent merging or acquisition event.

The presence in NGC 7442 of a circumnuclear starbursting ring, and of a nucleus presenting a superposition of H II-regions and AGN emission-line features, makes this object particularly attractive for integral-field spectroscopy. Using the model-based diagnostic diagrams of VO87 & K01, we aim to delineate the gas conditions in the nucleus and the nuclear ring. We describe the data sets used for this study and the basic methods applied to reduce and combine these data in Section 5.2. The results of our analysis are discussed in Section 5.3, which is followed by a discussion/conclusion section.

5.2 Observations and Data Reduction

In this study we combined data from two integral-field units (IFUs), DensePak (Barden & Wade 1988) on the WIYN telescope (a joint facility of the University of Wisconsin-Madison, Indiana University, Yale University, and National Optical Astronomy Observatories) and SAURON (Bacon et al. 2001) on the William Herschel Telescope. The combined dataset provides us with the key emission lines, $H\beta$ λ 4861, [O III] $\lambda\lambda$ 4959, 5007, [O I] λ 6300, [N II] $\lambda\lambda$ 6548, 6583, $H\alpha$ λ 6563, and [S II] $\lambda\lambda$ 6716, 6731, which are necessary to produce the diagnostic diagrams of VO87 and to constrain the gas density. The wavelength range of SAURON (4830 - 5330Å; data are from Falcón-Barroso et al. 2006) covers the $H\beta$ λ 4861 Balmer line and

the forbidden line doublet [O III] $\lambda\lambda 4959, 5007$, whereas the **DensePak** data (6085 - 7010Å; data from L. M. Mazzuca et al., in prep.) provides the other lines.

Although both instruments are IFUs with similar fields of view (33×41 and 30×45 arcsec for **SAURON** and **DensePak**, respectively) the designs are very different. **SAURON** is a fully sampled lenslet array, whereas **DensePak** consists of 89 functional fibers (2.812 arcsec diameter) bonded into a 7×13 staggered rectangle with center-to-center fiber spacings of 3.75 and 3.25 arcsec, horizontally and vertically. Both instruments record sky spectra simultaneously with the object spectra, allowing optimal sky subtraction. For NGC 7742, **SAURON** was configured in low-resolution mode, which results in a spectral resolution of 3.6 Å and a dispersion of 105 km s^{-1} . The **SAURON** measurements used in this work were presented by Falcón-Barroso et al. (2006). **DensePak** used the 860 lmm^{-1} grating centered around $\text{H}\alpha$, which yields a spectral resolution of 0.97 Å or 44 km s^{-1} .

To combine the two datasets, the **DensePak** spectra were analysed using the procedure of Sarzi et al. (2006), in order to separate the stellar absorption and gas emission contribution to the observed spectra. The resulting emission-line measurements from each of the three **DensePak** pointings were then merged on a common grid with spatial sampling matching that of the **SAURON** data (i.e. 0.8×0.8 arcsec). To describe the stellar continuum we have used linear combinations of single stellar population (SSP) models based on the MILES library of Sanchez-Blazquez et al. (2006). These templates are particularly suited to match the **DensePak** data, owing to their high spectral resolution of $\sigma\sim 2.2\text{Å}$ or $\sim 42\text{km s}^{-1}$ (R. F. Peletier, private communication). This is sufficient to match very well the absorption fea-

tures in the **DensePak** spectra, such as the prominent line around 6494\AA , which is due to Calcium and Iron. Given the limited number of absorption lines in the $\text{H}\alpha + [\text{N II}]$ regions, we have used only a restricted number of SSP templates adopting a Salpeter initial mass function, ages of $t = 0.1, 0.3, 1.0, 3.0, 10$ Gyr, and metallicities of $Z = 0.5, 1.0, 1.5 Z_{\odot}$. Such an accurate description of the stellar continuum is crucial to correctly estimate the $\text{H}\alpha$ and $[\text{S II}]$ line fluxes towards the center of NGC 7742, where the strength of the gas emission relative to the stellar continuum (and corresponding absorption features) decreases very sharply. In measuring the gas emission, a Gaussian profile was adopted for the $[\text{O I}]$, $[\text{N II}]$, $\text{H}\alpha$, and $[\text{S II}]$ lines, where the forbidden lines were further assumed to share the same kinematics.

Once the emission-line fluxes were measured, the **DensePak** integrated-flux field was fitted for each of the three pointings taken during the run to derive the position of the galaxy center. The pointings were then shifted to a common central position, adjusted to the same continuum flux level, which varied for each pointing, and then merged on a regular grid matching the sampling of the **SAURON** data. The same process was then used to merge the emission-line fluxes.

5.3 Results

Figure 5.1 shows the reconstructed images for the distribution of the $\text{H}\alpha$ and $[\text{N II}] \lambda 6583$ emission as measured with **DensePak**, together with similar maps for the $\text{H}\beta$ and $[\text{O III}] \lambda 5007$ fluxes obtained with **SAURON**. Despite the different designs of these two IFUs and the considerably coarser spatial sampling of **DensePak**, the

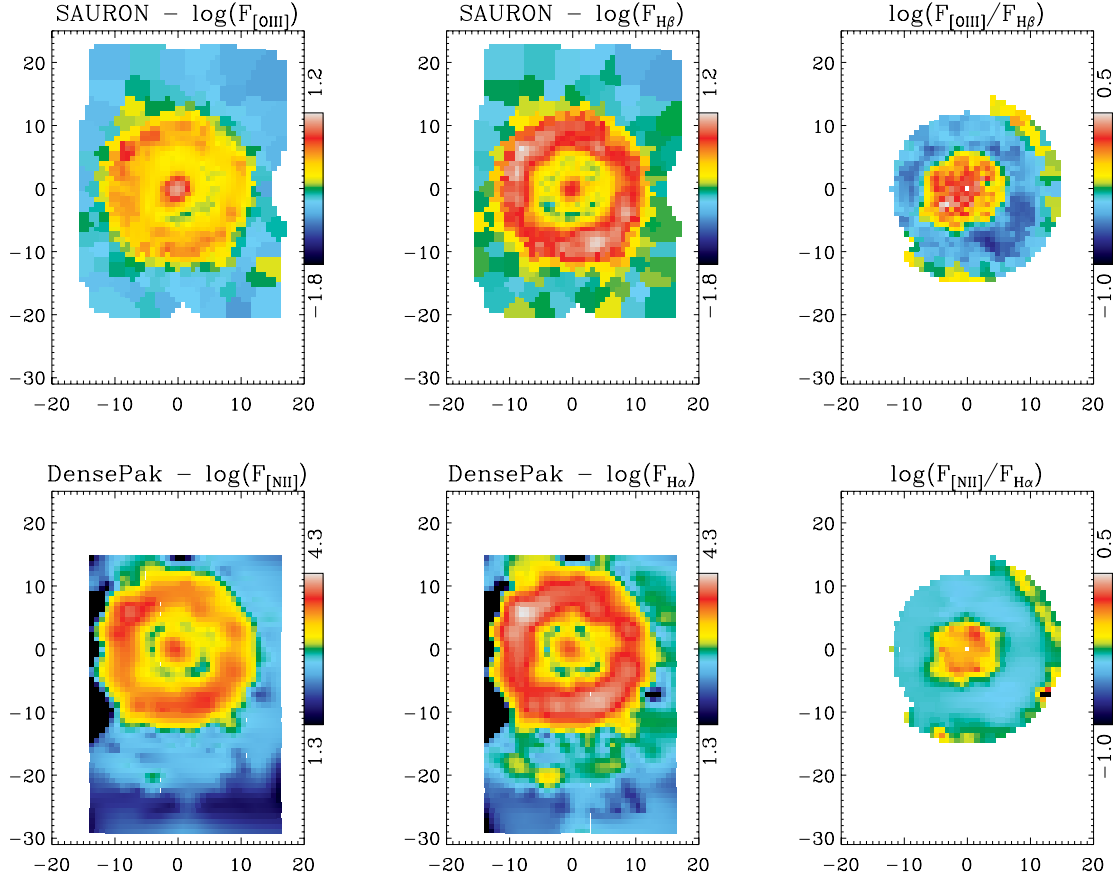


Figure 5.1: SAURON and DensePak maps for the $[\text{O III}]$ and $\text{H}\beta$ emission (top left and middle panels) and for the $[\text{N II}]$ and $\text{H}\alpha$ emission (lower left and middle panels), together with maps over a restricted common area (to avoid regions where the DensePak coverage is poor) for the $[\text{O III}] \lambda 5007 / \text{H}\beta$ and $[\text{N II}] \lambda 6583 / \text{H}\alpha$ line ratios (right panels). Axes are labelled with offsets in RA and DEC, in arcsec.

overall morphology of the recombination and forbidden lines agree very well. The rightmost panels of Fig. 5.1 show maps for the $[\text{N II}] \lambda 6583 / \text{H}\alpha$ and $[\text{O III}] \lambda 5007 / \text{H}\beta$ line ratios, which will be used to construct the corresponding VO87 diagnostic diagram separating star formation from other sources of ionization. Only a restricted area of NGC 7742 has been mapped in this way, due to the different centerings of the DensePak and SAURON fields, and to avoid regions where the DensePak coverage is poor. These maps already highlight a minimum in the value of these ratios in

the nuclear ring, indicative of star formation, with stronger $[\text{N II}] \lambda 6583/\text{H}\alpha$ and $[\text{O III}] \lambda 5007/\text{H}\beta$ not only towards the center but also outside the ring.

In the following we will constrain the gas density using the ratio of the $[\text{S II}]$ doublet lines (§ 5.3.1) and present $[\text{N II}]/\text{H}\alpha$ vs. $[\text{O III}]/\text{H}\beta$ and $[\text{N II}]/[\text{S II}]$ vs. $[\text{O III}]/\text{H}\beta$ diagnostic diagrams to constrain the role of the various ionizing mechanisms in different regions of NGC 7742 as well as the metallicity of the starburst in the circumnuclear regions (§ 5.3.2).

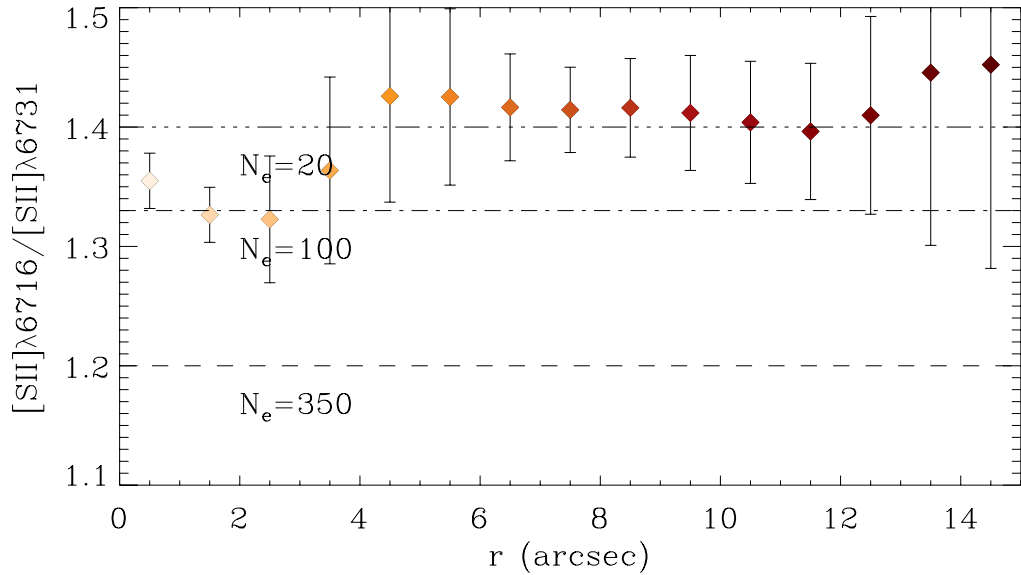


Figure 5.2: Radial variation of the $[\text{S II}] \lambda\lambda 6716, 6731$ line ratio, which is a tracer of the electron density N_e . The points show average values of the $[\text{S II}]$ lines ratio at a different radii with error bars indicating the azimuthal variation in this measurement. The horizontal lines indicate the $[\text{S II}]$ line ratio corresponding to specific values of N_e , assuming gas temperature of $T = 10^4 K$.

5.3.1 Gas Density

The relative strength of the lines in the $[\text{S II}]$ doublet is a strong function of the gas electron density N_e , only depending weakly on the gas temperature. The

observed line ratio can therefore be used to estimate N_e , although for low and high values of N_e , the [S II] $\lambda 6716$ /[S II] $\lambda 6731$ ratio saturates to values of ~ 1.4 and ~ 0.8 , respectively (Osterbrock 1989). Figure 5.2 shows, as a function of galactic radius, the ratio of the [S II] lines within the region of NGC 7742 considered for the emission-line diagnostic analysis (see Fig 5.1). The ratios of the [S II] lines indicate that the ring is predominantly populated by clouds of very low electronic density: on average $N_e = 20 \text{ cm}^{-3}$ within 8 and 12 arcsec from the center. Such low values for N_e are typical of extragalactic H II regions, where $N_e < 100 \text{ cm}^{-3}$ (Dopita et al. 2000), but considerably smaller than observed in the central regions of starbursting galaxies, where the typical value is $N_e \sim 350 \text{ cm}^{-3}$ within 1 kpc (K01). N_e increases towards the center of NGC 7742, although only to $N_e \sim 100 \text{ cm}^{-3}$

Following this result, we will adopt a gas density of $N_e = 10 \text{ cm}^{-3}$ for the photoionization MAPPINGS III (Kewley et al. 2001) models that will be used in the next section to interpret our data in the circumnuclear ring regions.

5.3.2 Excitation Mechanisms

Among the reddening-insensitive diagnostic diagrams introduced by VO87, the [O I] $\lambda 6300$ /H α vs. [O III] $\lambda 5007$ /H β diagnostic is the best suited to separate OB star excitation from other excitation sources, since the [O I] emission originates in partially ionized regions arising only in the presence of a hard ionizing spectrum. Unfortunately in NGC 7742 the weak [O I] emission is detected only in the circumnuclear ring, where the equivalent width of the emission lines is the largest. Fur-

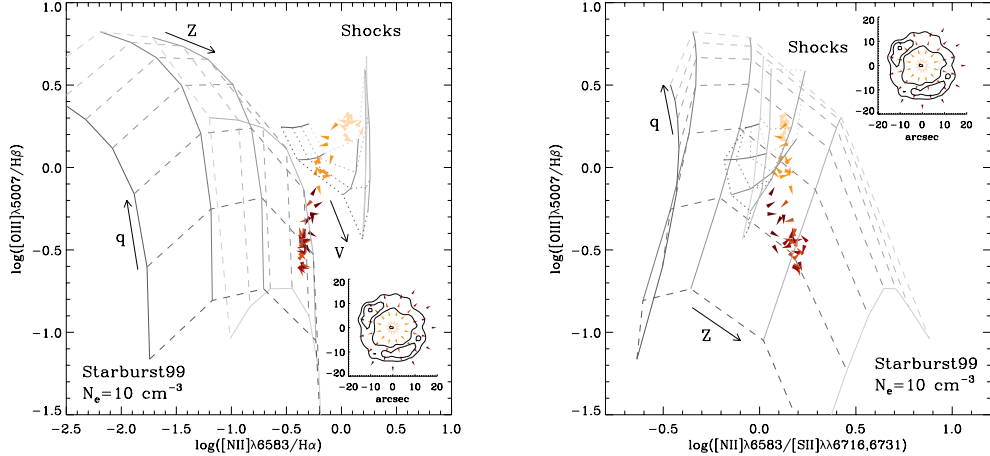


Figure 5.3: Diagnostic diagrams of $[O III] \lambda 5007/H\beta$ vs. $[N II] \lambda 6583/H\alpha$ (left) and $[O III] \lambda 5007/H\beta$ vs. $[N II] \lambda 6583/[S II] \lambda\lambda 6716, 6731$ (right). Data from both SAURON and DensePak observations are shown by the filled triangles, and were extracted in coronal sections at different distances from the center and at different position angles. In both panels the inset shows the location of these extractions in the galactic frame, with the contours showing the $H\alpha$ circumnuclear ring. The symbols are color-coded from lighter to darker tones for increasing radii and oriented according to the position angle of coronal sections apertures. In each panel the prediction of MAPPINGS III starburst or shock models are shown by the grid of solid and dashed lines or of solid and dotted lines, respectively. For the starburst models, which assume a gas density of $N_e \sim 10 \text{ cm}^{-3}$, solid lines of increasingly lighter shades of grey show models of constant metallicity equal to $Z = 0.05, 0.2, 0.4, 1.0, 2.0 Z_\odot$, whereas the dashed lines show models with progressively larger values for the ionization parameter $q = 5e6, 1e7, 2e7, 4e7, 8e7, 1.5e8, 3e8 \text{ cm s}^{-1}$. Similarly, for the shock models, the grey solid lines show models with increasing shock velocity $V_s = 150, 200, 300, 500, 750, 1000 \text{ km s}^{-1}$, and the dotted lines models with magnetic parameter $b = 0.5, 1.0, 2.0, 4.0$.

thermore, Dopita et al. (2000) showed that the models cannot distinguish precisely between ionization by hot stars and other sources of ionization using the $[O I]/H\alpha$ and, to some extent, the $[S II]/H\alpha$ diagnostics, as these ratios can be affected by weak shocks from supernovae.

The left panel of Figure 5.3 thus shows the location of our data in the $[N II]/H\alpha$ vs. $[O III]/H\beta$ diagnostic diagram, together with the predictions of MAPPINGS III

models for H II regions in an instantaneous starburst or for clouds excited by shocks.¹

The starburst models use a spectral energy distribution obtained from Starburst99 (Leitherer et al. 1999) and assume a range of metallicity Z for both stars and gas in the starburst and different values of the ionization parameter q , defined as the ratio of the ionizing photon flux to local number density of hydrogen atoms at the illuminated edge of the gas cloud. The shock models assume a range of values for the shock velocity V_s and for the magnetic parameter b . For a thorough description of these models see Dopita et al. (2000) and Allen, Dopita & Tsvetanov (1998).

The [N II]/H α vs. [O III]/H β diagram (see Fig. 3) clearly separates the emission arising in the circumnuclear ring (red and orange triangles) from emitting regions both outside (brown) and inside the ring (yellow). The line emission from the ring region is consistent with the predictions of the starburst models, whereas the position of the data points measured outside the ring suggest that shocks may play a role in this region, particularly near the inner edge of the ring. As far as the nuclear regions are concerned, however, it is important to keep in mind that models for photoionization by an AGN can predict line ratios very similar to those shown for the shock models (Allen et al. 1998), so that excitation by a central engine cannot be excluded.

Although the [N II]/H α vs. [O III]/H β diagnostic diagram is useful to show the role of different excitation mechanisms in different galactic regions, it cannot generally be used to derive the physical condition of the H II regions, except in the

¹Both sets of models were obtained from the MAPPINGS III portal at <http://www.ifa.hawaii.edu/~kewley/Mappings/>

very low metallicity regime. The models in fact fold around themselves, so that any given location in the diagnostic diagram occupied by starburst models with $Z > 0.2Z_{\odot}$ could correspond either to an H II region of low metallicity and low ionization parameter or to an H II region with considerably larger values of Z and q . In the combined wavelength range of the **DensePak** and **SAURON** observations the best diagnostic to constrain the metallicity of the ring starburst is the $[\text{N II}]/[\text{S II}]$ ratio. Rubin, Ford & Whitmore (1984) were the first to demonstrate the utility of this line ratio, which serves well to estimate metallicities from slightly sub-solar to super-solar values (Kewley et al. 2002). The right panel of Figure 5.3 shows the location of our data in the $[\text{N II}]/[\text{S II}]$ vs. $[\text{O III}]/\text{H}\beta$ diagnostic diagram, which unequivocally demonstrates that the circumnuclear ring is predominantly populated by H II regions with near-solar metallicity. Having learned from the $[\text{N II}]/\text{H}\alpha$ vs. $[\text{O III}]/\text{H}\beta$ diagram that, both inside and outside the ring, sources other than OB stars may contribute to the gas excitation, we note that the regions outside the ring (brown symbols) seem to approach the shock-model grid from a different direction than the point inside the ring (orange symbols). This suggests that if indeed shocks are contributing to heating and/or ionizing the gas, they may occur under different conditions at the opposite edges of the ring.

5.4 Discussion and Conclusions

We have combined two integral-field spectroscopic data sets to study the role of various ionizing mechanisms in powering the gas emission in the central kpc of

NGC 7742. Our spatially resolved emission-line diagnostic analysis reveals a sharp transition between regions powered by hot OB stars in the circumnuclear ring to LINER-like emission both inside and outside the ring. Comparison with models for shock-ionization indicates that shocks can contribute to the gas excitation in these regions, in particular outside the ring. Toward the center, photoionization by a central AGN could also be important. The ratio of the [S II] doublet lines indicates low electron density, $N_e < 100 \text{ cm}^{-3}$, in the ring regions, where comparison with MAPPINGS III photoionization models shows that the gas and stars have approximately solar metallicity.

NGC 7742 shows clear signs of past galaxy interaction, as indicated by opposing directional flow of the gas and stars. Although NGC 7743 accompanies NGC 7742 and is sufficiently massive to have provided the metal-rich gaseous material observed in the nuclear ring, the large distance between the two galaxies and the morphologically pristine characteristics of both objects rule out a recent interaction. This leads us to consider an alternative scenario, whereby NGC7742 cannibalized a smaller galaxy, rich in gas of low metallicity. This material was then funneled in the ring where star formation proceeded long enough for the metallicity of the starburst to increase to its present value. Falc3n-Barroso et al. estimate a mass for the ionised-gas in NGC7742 of few $10^6 M_\odot$, most of which is found in the ring. To reach an oxygen mass fraction of 1%, corresponding to solar metallicity, it would take just tens Myr to have enough supernovae injecting enriched material in the ring, assuming a Salpeter (1955) initial mass function and a star formation rate of few $M_\odot \text{ yr}^{-1}$ (as shown in Chapter 3). Considering that gas moving at $\sim 100 \text{ km s}^{-1}$

would travel around the ring in $\sim 60\text{Myr}$, if it takes a few dynamical timescales for the gas to cross the ring, the circumnuclear starburst of NGC 7742 could have easily reached solar metallicities. More constraints on the gas dynamics are needed to construct a detailed chemo-dynamical model, which is necessary to verify this scenario. Alternatively, deeper spectroscopic data could be used to constrain the metallicity of the gas outside the ring, which according to the previous picture should have a very low metallicity.

Chapter 6

Summary & Conclusions

This thesis set out to answer the questions posed in Section 1.6, which acted as guides to gaining a fuller, more statistically based, understanding of the physical nature of nuclear rings and their influence on the local galactic environment. We approached the analysis by using photometric and kinematic observational techniques to better characterize the morphology and distribution of the H II regions that comprise a nuclear ring, while relating the presence of massive star formation within the rings to the chemical composition, velocity, and random motions within, and just outside, the rings. We can now answer the questions that acted as the framework for this thesis:

Question set #1: What is the distribution of massive young stars in the nuclear and circumnuclear regions? How do the photometric morphologies of nuclear and circumnuclear H α distribution compare to the Hubble type and presence or absence of a bar in the host galaxy? Are our results consistent with previous observations that nuclear rings preferentially appear in barred spiral galaxies? Is there a possible link between nuclear rings and the presence of starburst galaxies and active galactic nuclei?

Answer: Of the 73 galaxies that we analyzed, we find the following:

- 60% have relatively strongly peaked nuclear H α emission, with half of the

sample containing a more diffuse, patchy circumnuclear emission, where we defined the radial limit of the circumnuclear region to at a 2 kpc radius.

- Within the circumnuclear environment, we detect 22 nuclear rings. The histograms in Figures 2.2 and 2.3 confirm an $H\alpha$ emission peak near types Sb and Sbc.
- Late-type galaxies have a patchy circumnuclear appearance in $H\alpha$, and nuclear rings occur primarily in early types, where their existence strongly correlates to spiral types Sa-Sbc.
- When comparing the morphological classifications for barred versus non-barred galaxies, $\sim 70\%$ of non-barred and $\sim 60\%$ of the barred galaxies has strong nuclear $H\alpha$ emission, with percentages for both barred and non-barred galaxies mirroring each other, with respect to either weak or no noticeable nuclear $H\alpha$ emission.
- The bar distribution in the galaxies in the different classes of circumnuclear emission is similar to that of nuclear distribution. Approximately half of the barred and non-barred galaxies have a patchy circumnuclear $H\alpha$ morphology.
- Nuclear rings are predominantly hosted by barred galaxies, which adds more credence to the fact that bar fuel nuclear rings, although we see that bars do not influence the relative strength of the nuclear $H\alpha$ peak, nor other aspects of the circumnuclear $H\alpha$ morphology.
- Nuclear rings prefer to co-habitat with AGN - $\sim 60\%$ of the nuclear ring galax-

ies in our sample have an AGN. This connection is partly due to AGN and rings are most common in early-type galaxies, but also most likely to be through the availability and recent inflow of gas, which fuels both the massive star formation in the ring and nuclear activity.

Question set #2: What are the statistics for size, morphology, and luminosity of nuclear rings and the individual star-forming clusters that define the HII regions within the rings? How do these properties relate to the morphology of their hosts? Is there a relationship between the position angles and ellipticities of the rings and those of their host galaxies? What are the dynamical time scales of nuclear rings? Is there an age gradient between the H II regions defining the ring, and if so, how do the distributions relate to the location of the bar and its dust lanes that intersect with the ring, as well as the morphology of the ring or its host galaxy?

Answer: Of the 22 nuclear rings identified in Chapter 2, we find the following:

- Typical sizes of nuclear rings are of the order 1 kpc; our sample contained rings of size from 0.2 kpc to 1.7 kpc.
- Morphological comparison (ellipticity and PA) of the nuclear rings to that of their host galaxies shows that, in all but one case, the rings match the shape of their respective disk. We thus conclude that the rings are in the same plane as the disk, and circular.
- When age dating the identified H II regions that form the nuclear ring, 11 of the rings in our sample exhibit a well-defined age distribution pattern, but not necessarily throughout the entire ring. This can be due to a combination of

bar-induced dynamics and gravitational instabilities that are occurring on an intermittent basis.

- Of those 11 nuclear rings, NGC 1343, NGC 1530, and NGC 4321, contain bipolar age gradients, where the ages increased from each of the contact points (i.e., where the bar dust lanes merge with the nuclear ring).
- The SFR calculated within the nuclear rings yields no clues to a possible connection between the rate of inflow and the appearance (or type of) age gradient.
- In two-thirds of the galaxies in this sample, there is a correlation between the location of the bar contact points to the youngest H II regions in the nuclear ring.

Question set #3: Are noncircular motions present within the nuclear rings?

Is there a relation between the enhanced star formation seen in nuclear rings and the level of velocity residuals and dispersions within the rings? Are the velocity transitions across the ring and the ring boundaries stronger in the presence of a bar? If so, how do they relate to the location of the bar major and minor axes? Do the photometrically-determined nuclear ring parameters differ from those of the kinematic data? If so, what are the possible causes?

Answer: From the sample analyzed in Chapter 2, we chose a subset of 10 nuclear rings and find the following:

- Low residual velocities (of roughly 20 km s^{-1}) within the sample of seven nu-

clear rings imply that strong non-circular motions are *not* present.

- Within the nuclear rings, dispersions are comparably *low* and range from 20 km s^{-1} to 50 km s^{-1} .
- The low dispersions and residuals correlate spatially with the strongest H α emissions and high luminosities in the nuclear rings and those galaxies that contain active nuclei. This implies that the gas is cool in the rings (of order 10^3 K) and relatively non-turbulent, which allows star formation to trigger.
- Literature on the nature of bars reveals that this cool gas emanates from the bar dust lanes. Thus, the dust lanes are most likely the major source of continual inflow of the cool gas into these rings.
- The lower dispersions also correspond to flatter RCs near the location of the nuclear rings.
- Of the barred galaxies in our sample, the outer boundary of the nuclear ring is delineated by a thin shell of increased velocity gradients, with the strongest velocity transitions existing across the outer edge of the nuclear rings, along the bar minor axis.
- Expansion of the VF shows trends that are seen along the ring exterior boundary, near the location of the bar. Higher-order perturbations seen just outside the nuclear rings for three cases, confirm elongation of the potential (due to the influence of the bar); no such perturbations are seen within any of the nuclear rings.

- Kinematically, nuclear rings are circular and typically in the same plane as the galaxy disk. Large offsets between the ring kinematic and photometric PAs for three cases are attributed to complex interactions with the bar or, in the case of NGC 5953, with a merging galactic system.

Question set #4: Can we distinguish between different environments in a circumnuclear region that is known to be a composite of an AGN/LINER and a nuclear ring? How is the environment inside the nuclear ring characterized? Can the optical lines constrain the local gas density and metallicity within the ring? What are the ionization sources inside and outside of the ring?

Answer: We analyzed NGC 7742, which is part of all samples discussed in this thesis, and find that:

- Using [O I] $\lambda 6300$, [N II] $\lambda\lambda 6548, 6583$, H α $\lambda 6563$, [S II] $\lambda\lambda 6716, 6731$, combined with H β $\lambda 4861$ and [O III] $\lambda\lambda 4959, 5007$ (from another instrument), reveals a sharp transition between regions powered by hot OB stars in the nuclear ring to LINER-like emission both inside and outside the ring.
- The ratio of the [S II] doublet lines indicates low electron density, $N_e < 100 \text{ cm}^{-3}$, in the the nuclear ring, with the gas and stars having approximately solar metallicity.

- Comparison with models for shock-ionization indicates that shocks can contribute to the gas excitation in the circumnuclear regions outside the ring.
- In the case of NGC 7742 the line ratio analysis paints a picture whereby the galaxy cannibalized a smaller galaxy, rich in gas of low metallicity. The material was then funneled in the ring where star formation proceeded long enough for the metallicity within the ring to increase to its present value.

Chapter 7

Future Considerations

While optical imaging has proven to be an effective method for analysis of nuclear rings, the results presented in this thesis are clearly subject to the typically dusty environments of nuclear rings. Many rings appear to be incomplete, and are most likely obscured from the observer by dust along the line of sight. Mid-IR observations with such telescopes as the *Spitzer Space Telescope* may reveal star formation in portions of the rings that are obscured at visible wavelengths, or even find yet undiscovered nuclear rings, which are overshadowed by very active nuclei or dust. Regan et al. (2004) show such feats are possible from analysis of the large scale ring ($r \sim 6$ kpc) in NGC 7331. The ring is partially seen in $H\alpha$ (and not seen at all in other optical wavelengths such as the V -band), where heavy dust emission conceals the ring; however, the ring is fully revealed at $5.8 \mu\text{m}$, $8 \mu\text{m}$, and $24\mu\text{m}$.

The mid-IR range has the further advantage of tracing the emission from polycyclic aromatic hydrocarbons (PAHs) around the ring in highly obscured regions. PAHs are known to be a reliable signature for very hot young stars, whose radiation heat the non-thermal dust grains (Contursi, A. et al 2002). Complementing the data in this thesis with that from the mid to far-IR wavelengths may provide more accurate information on the distribution and mass of gas and dust within nuclear rings, and better constrain the star formation, morphology, and mass inflow rates,

as well as possibly provide a lower age limit.

Kinematically, our data has very high velocity resolution, yet suffers from poor spatial sampling as a result of the technique implemented. This yielded less than desirable results in some cases. Ideally, full spatial coverage, as provided by an IFU lenslet array vs. a fiber bundle configuration, combined with very high velocity resolution should provide better resolved RCs and maps of the velocity gradients, and better constraints on the derived kinematic parameters within the central kiloparsecs of galaxies.

The results from our line ratio analysis hold the most promise for near-future work. By utilizing key emission lines ($H\alpha$, $[N II]$, and $[O III]$) and combining those with lines outside of our wavelength range ($H\beta$ and $[O I]$), we are able to constrain the electron density and metallicity of the ionized gas, and the ionization parameter within and near a nuclear ring. By observing the rest of the rings in the wavelengths of interest and implementing the same method as described in Chapter 5, we can present a fuller picture of the physical conditions in and around nuclear rings.

Appendix A

Individual H II Region Parameters for the Galaxies

For each ring in the sample we present tables that contain each H II region as identified by `SEXTRACTOR` (col. 1), integrated flux (col. 2), luminosity (col. 3), EW (col. 4) and $\log(\text{EW})$ (col. 5). Column 6 indicates if the *I*-band flux needed to be modified in order to compensate for unrealistic values (i.e., negative flux values or marginally positive flux values – see Section 3.4.2). In the cases where the *I*-band flux generated from `SEXTRACTOR` was not modified, a value of ‘0’ is recorded; otherwise a value of ‘1’ is recorded. Since `SEXTRACTOR` detects all H II regions in the supplied image, extraneous H II regions as well as the nucleus were included in the identification process. These superfluous detections are not included in the tables, but are instead noted in the captions for completeness sake.

H II region	Integrated Flux (10^{-13} erg s $^{-1}$ cm $^{-2}$)	Luminosity (10^{39} erg s $^{-1}$)	EW (Å)	log(EW) (Å)	Flux Correction
(1)	(2)	(3)	(4)	(5)	(6)
1	3.38	5.63	258	2.41	0
2	0.98	1.63	229	2.36	1
3	0.56	0.93	84	1.92	1
5	1.74	2.91	485	2.69	1
7	4.98	8.30	536	2.73	0
8	0.52	0.86	81	1.91	1
9	0.7	1.17	143	2.15	1
10	6.20	10.3	3341	3.52	1
11	0.51	0.85	4	0.56	0
12	0.86	1.44	146	2.16	0
13	0.66	1.10	128	2.11	1
14	0.98	1.63	142	2.15	0
18	3.36	5.61	365	2.56	0
19	2.62	4.36	650	2.81	0
20	1.12	1.87	284	2.45	1
21	0.87	1.45	114	2.06	1
22	0.54	0.91	53	1.72	1
23	0.72	1.20	133	2.12	1
24	0.90	1.51	222	2.35	1
25	1.02	1.71	157	2.20	0
26	3.54	5.90	1620	3.21	1

Table A.1: NGC 278 - 20 H II regions detected associated with the ring. H II regions # 4, 6, and 11 comprise the nucleus; H II regions # 15, 16, and 17 are extraneous to the ring.

H II region	Integrated Flux (10^{-13} erg s $^{-1}$ cm $^{-2}$)	Luminosity (10^{39} erg s $^{-1}$)	EW (\AA)	log(EW) (\AA)	Flux Correction
(1)	(2)	(3)	(4)	(5)	(6)
1	0.33	3.49	216	2.33	1
4	4.01	42.6	9343	3.97	1
5	1.42	15	1643	3.22	0
6	3.34	35.5	1409	3.15	0
7	1.88	20	2660	3.42	0
8	0.62	6.57	608	2.78	1
9	0.35	3.73	222	2.35	1
10	0.37	3.93	262	2.42	1
11	1.03	10.9	942	2.97	0
12	1.15	12.3	1812	3.26	1
13	0.42	4.44	389	2.59	1
14	0.22	2.37	122	2.09	1
15	1.32	14.1	647	2.81	0
16	0.11	1.20	41	1.62	1
17	1.13	12	1722	3.24	1
18	0.60	6.37	647	2.81	1
19	0.32	3.37	200	2.30	1
20	1.60	17	2241	3.35	0
21	2.08	22.1	2622	3.42	0
22	0.83	8.85	1138	3.06	1
25	1.55	16.5	1261	3.10	0
26	0.17	1.83	70	1.85	1
28	0.32	3.36	192	2.28	1
29	0.10	1.05	25	1.41	1
30	0.22	2.32	120	2.08	1
32	0.19	2.02	78	1.89	1
33	0.26	2.79	107	2.03	1

Table A.2: NGC 473 - 27 H II regions detected associated with the ring. H II regions # 23 and 24 comprise the nucleus; H II regions # 2, 3, 27, and 31 are extraneous to the ring.

H II region	Integrated Flux (10^{-13} erg s $^{-1}$ cm $^{-2}$)	Luminosity (10^{39} erg s $^{-1}$)	EW (Å)	log(EW) (Å)	Flux Correction
(1)	(2)	(3)	(4)	(5)	(6)
1	26.3	96.4	179	2.25	0
3	13.3	48.9	88	1.95	0
4	3.87	14.2	189	2.28	0
5	2.26	8.28	374	2.57	0
6	8.49	31.1	26	1.42	0
7	1.00	3.66	130	2.12	0
8	2.00	7.33	221	2.34	0
9	0.84	3.08	77	1.88	0
10	0.86	3.14	368	2.57	0
12	11.4	41.8	148	2.17	0
13	5.89	21.6	87	1.94	0

Table A.3: NGC 613 - 12 H II regions detected. H II regions # 2 and 11 are extraneous to the ring.

H II region	Integrated Flux (10^{-13} erg s $^{-1}$ cm $^{-2}$)	Luminosity (10^{39} erg s $^{-1}$)	EW (Å)	log(EW) (Å)	Flux Correction
(1)	(2)	(3)	(4)	(5)	(6)
1	1.34	5.69	107	2.03	0
2	1.34	5.67	56	1.75	0
3	0.21	0.88	47	1.67	1
4	0.05	0.23	7	0.85	1
5	0.40	1.71	118	2.07	1
6	0.16	0.67	33	1.52	1
7	0.15	0.63	25	1.39	1
8	0.18	0.75	37	1.57	1
10	0.70	2.95	240	2.38	1
11	0.51	2.17	155	2.19	1
12	0.45	1.91	158	2.20	1
13	0.39	1.64	56	1.74	0

Table A.4: NGC 1300 - 12 H II regions detected associated with the ring. H II region # 9 is the nucleus.

H II region	Integrated Flux (10^{-13} erg s $^{-1}$ cm $^{-2}$)	Luminosity (10^{39} erg s $^{-1}$)	EW (Å)	log(EW) (Å)	Flux Correction
(1)	(2)	(3)	(4)	(5)	(6)
1	8.24	85.8	5364	3.73	1
2	10.2	106	744	2.87	0
3	4.73	49.2	330	2.52	0
4	2.14	22.3	247	2.39	0
5	3.88	40.4	650	2.81	0
6	1.36	14.2	396	2.60	1
7	1.44	15	400	2.60	1
8	18.9	196	5845	3.77	0
9	0.36	3.79	33	1.52	1
10	0.65	6.73	80	1.91	1
11	1.37	14.3	401	2.60	1
12	3.95	41.1	737	2.87	0
16	2.55	26.5	968	2.99	1
17	4.61	48	373	2.57	0
18	3.22	33.6	1340	3.13	1
19	4.12	42.9	1339	3.13	0
20	0.72	7.53	117	2.07	1
21	4.84	50.4	2513	3.40	1
22	3.77	39.3	479	2.68	0
23	1.52	15.8	305	2.48	1

Table A.5: NGC 1343 - 20 H II regions detected associated with the ring. H II regions # 13 and 14 comprise the nucleus; H II region # 15 is extraneous to the ring.

H II region	Integrated Flux (10^{-13} erg s $^{-1}$ cm $^{-2}$)	Luminosity (10^{39} erg s $^{-1}$)	EW (\AA)	log(EW) (\AA)	Flux Correction
(1)	(2)	(3)	(4)	(5)	(6)
1	6.79	109	1895	3.28	0
2	13.4	215	630	2.80	0
3	1.46	23.4	243	2.38	0
4	1.05	16.8	232	2.37	0
7	0.52	8.32	66	1.82	0
11	0.52	8.31	854	2.93	1
14	1.84	29.5	274	2.44	0
15	0.98	15.8	1951	3.29	1
17	1.55	24.8	3123	3.49	1

Table A.6: NGC 1530 - 9 H II regions detected associated with the ring. H II regions # 8, 9, 10, 12, 13, and 16 comprise the nucleus; H II regions # 5 and 6 are extraneous to the ring.

H II region	Integrated Flux (10^{-13} erg s $^{-1}$ cm $^{-2}$)	Luminosity (10^{39} erg s $^{-1}$)	EW (\AA)	log(EW) (\AA)	Flux Correction
(1)	(2)	(3)	(4)	(5)	(6)
2	25.7	71.1	99	2.00	0
3	17.8	49.2	112	2.05	0
4	1.33	3.67	367	2.57	0
5	6.82	18.9	624	2.80	0
6	1.35	3.74	74	1.87	0
7	9.61	26.6	1676	3.22	0
8	1.14	3.14	106	2.03	0

Table A.7: NGC 4303 - 7 H II regions detected associated with the ring. H II region # 1 comprises the nucleus.

H II region	Integrated Flux (10^{-13} erg s $^{-1}$ cm $^{-2}$)	Luminosity (10^{39} erg s $^{-1}$)	EW (\AA)	log(EW) (\AA)	Flux Correction
(1)	(2)	(3)	(4)	(5)	(6)
1	3.32	3.74	529	2.72	0
2	3.78	4.25	2607	3.42	0
3	0.39	0.44	111	2.05	0
4	0.23	0.26	148	2.17	0
5	2.13	2.40	375	2.57	0
7	2.82	3.18	1801	3.26	0
8	0.12	0.14	344	2.54	0
9	0.54	0.61	211	2.32	0
10	0.42	0.48	1088	3.04	0
11	0.46	0.52	1288	3.11	0

Table A.8: NGC 4313 - 10 H II regions detected associated with the ring. H II region # 6 comprises the nucleus.

H II region	Integrated Flux (10^{-13} erg s $^{-1}$ cm $^{-2}$)	Luminosity (10^{39} erg s $^{-1}$)	EW (\AA)	log(EW) (\AA)	Flux Correction
(1)	(2)	(3)	(4)	(5)	(6)
2	27.8	171	1106	3.04	0
3	4.08	25.2	259	2.41	0
4	1.23	7.58	206	2.31	0
5	0.92	5.68	1277	3.11	1
6	1.82	11.2	6790	3.83	1
7	6.18	38.1	121	2.08	0
8	2.88	17.8	222	2.35	0
9	1.06	6.53	49	1.69	0
10	3.76	23.2	6378	3.80	0
11	1.87	11.5	2275	3.36	0
12	4.93	30.4	485	2.69	0
13	2.03	12.5	539	2.73	0
14	7.44	45.9	191	2.28	0
15	14	86.1	965	2.98	0
16	0.57	3.52	78	1.89	0
17	1.86	11.5	153	2.19	0
18	1.51	9.33	3125	3.49	1
19	0.88	5.40	1145	3.06	1
20	1.82	11.2	179	2.25	0

Table A.9: NGC 5248 - 19 H II regions detected associated with the ring. H II region # 1 comprises the nucleus.

H II region	Integrated Flux (10^{-13} erg s $^{-1}$ cm $^{-2}$)	Luminosity (10^{39} erg s $^{-1}$)	EW (Å)	log(EW) (Å)	Flux Correction
(1)	(2)	(3)	(4)	(5)	(6)
3	2.28	48.6	1164	3.07	0
4	0.27	5.76	163	2.21	0
5	2.13	45.4	7961	3.90	1
6	2.19	46.7	248	2.40	0
7	3.87	82.5	556	2.74	0
8	0.21	4.48	170	2.23	1
9	0.70	15	1516	3.18	1
10	0.16	3.53	109	2.04	1
11	0.30	6.32	479	2.68	1
12	0.17	3.58	111	2.04	1
13	0.22	4.78	226	2.35	1
14	0.62	13.3	1218	3.09	1
15	1.11	23.6	3084	3.49	1
17	4.09	87.2	211	2.32	0
18	3.52	75	1426	3.15	0
19	1.53	32.6	1310	3.12	0
21	0.24	5.10	182	2.26	1
22	0.39	8.38	455	2.66	0

Table A.10: NGC 5728 - 18 H II regions detected associated with the ring. H II regions # 1 and 2 comprise the nucleus; H II regions # 16 and 20 are extraneous to the ring.

H II region	Integrated Flux (10^{-13} erg s $^{-1}$ cm $^{-2}$)	Luminosity (10^{39} erg s $^{-1}$)	EW (\AA)	log(EW) (\AA)	Flux Correction
(1)	(2)	(3)	(4)	(5)	(6)
1	2.39	58.5	77	1.88	0
2	2.63	64.3	189	2.28	0
3	0.40	9.80	97	1.99	0
4	0.67	16.3	2870	3.46	1
5	0.41	10	177	2.25	0
6	0.38	9.37	154	2.19	0
7	0.25	6.20	199	2.30	0
8	3.27	79.9	87	1.94	0
9	1.75	42.7	132	2.12	0

Table A.11: NGC 5905 - 9 H II regions detected associated with the ring. No nuclear or extraneous H II regions detected.

H II region	Integrated Flux (10^{-13} erg s $^{-1}$ cm $^{-2}$)	Luminosity (10^{39} erg s $^{-1}$)	EW (\AA)	log(EW) (\AA)	Flux Correction
(1)	(2)	(3)	(4)	(5)	(6)
2	3.84	249	15	1.17	0
3	3.82	248	16	1.21	0
4	0.93	60.2	29	1.46	0

Table A.12: NGC 5945 - 3 H II regions detected associated with the ring. H II region # 1 comprises the nucleus.

H II region	Integrated Flux (10^{-13} erg s $^{-1}$ cm $^{-2}$)	Luminosity (10^{39} erg s $^{-1}$)	EW (Å)	log(EW) (Å)	Flux Correction
(1)	(2)	(3)	(4)	(5)	(6)
2	11.6	152	152	2.18	0
3	9.84	128	390	2.59	0
4	24.9	324	541	2.73	0
5	2.24	29.2	652	2.81	1
6	1.22	15.9	247	2.39	1
7	6.38	83.2	614	2.79	0
8	2.56	33.3	591	2.77	0
9	5.41	70.5	2162	3.33	1
10	4.35	56.7	784	2.89	0
11	2.19	28.5	94	1.97	0
12	3.22	42	1013	3.01	1
13	0.43	5.57	30	1.48	1
14	0.74	9.67	88	1.94	1
15	2.01	26.1	4	0.61	0
16	0.45	5.82	4	0.55	0
17	2.57	33.5	130	2.12	0
18	1.86	24.3	50	1.70	0
19	3.25	42.4	154	2.19	0
20	3.63	47.4	1374	3.14	1
21	7.02	91.5	866	2.94	0
22	0.33	4.30	23	1.37	1
23	0.46	5.99	48	1.68	1

Table A.13: NGC 5953 - 22 H II regions detected associated with the ring. H II region # 1 comprises the nucleus.

H II region	Integrated Flux (10^{-13} erg s $^{-1}$ cm $^{-2}$)	Luminosity (10^{39} erg s $^{-1}$)	EW (Å)	log(EW) (Å)	Flux Correction
(1)	(2)	(3)	(4)	(5)	(6)
3	38.6	17.2	3686	3.57	0
4	7.12	3.17	804	2.91	1
5	1.08	0.48	45	1.65	1
6	2.28	1.01	151	2.18	1
7	1.55	0.69	52	1.71	1
8	1.90	0.84	67	1.83	1
9	3.43	1.53	224	2.35	1
10	2.08	0.93	98	1.99	1
11	4.07	1.81	307	2.49	1
12	0.94	0.42	26	1.42	1
13	10.7	4.76	1715	3.23	1
14	2.60	1.16	214	2.33	1
15	2.64	1.18	120	2.08	1
16	1.13	0.50	40	1.60	1
17	0.55	0.25	12	1.08	1
18	0.59	0.26	13	1.11	1
19	1.00	0.45	31	1.49	1
20	10.5	4.66	796	2.90	0
21	14.8	6.59	1123	3.05	0
22	12.3	5.46	2072	3.32	1
23	4.66	2.08	304	2.48	1
24	0.87	0.39	22	1.34	1
25	2.64	1.18	190	2.28	1
26	1.32	0.59	70	1.85	1
27	9.70	4.32	1271	3.10	1
28	1.22	0.54	37	1.57	1
29	0.95	0.42	21	1.32	1
30	5.72	2.55	431	2.63	1
31	2.87	1.28	148	2.17	1
32	2.32	1.03	92	1.96	1
33	6.78	3.02	808	2.91	1
34	2.18	0.97	132	2.12	1
35	3.92	1.75	323	2.51	1
36	11.8	5.26	1774	3.25	1
37	33	14.7	6628	3.82	1

Table A.14: NGC 6503 - 84 H II regions detected associated with the ring. H II regions # 39, 44, and 45 comprise the nucleus; H II regions # 1, 2, and 86 are extraneous to the ring.

H II region	Integrated Flux (10^{-13} erg s $^{-1}$ cm $^{-2}$)	Luminosity (10^{39} erg s $^{-1}$)	EW (Å)	log(EW) (Å)	Flux Correction
(1)	(2)	(3)	(4)	(5)	(6)
38	5.41	2.41	584	2.77	1
40	5.55	2.47	570	2.76	1
41	9.64	4.29	1331	3.12	1
42	7.17	3.19	661	2.82	1
43	2.88	1.28	240	2.38	1
46	9.87	4.39	1363	3.13	1
47	1.36	0.61	51	1.71	1
48	1.30	0.58	49	1.69	1
49	3.55	1.58	299	2.48	1
50	1.85	0.82	66	1.82	0
51	1.19	0.53	40	1.60	1
52	3.29	1.47	278	2.44	1
53	3.95	1.76	337	2.53	1
54	2.51	1.12	191	2.28	1
55	2.97	1.32	129	2.11	1
56	2.92	1.30	172	2.24	1
57	10.3	4.57	1594	3.20	1
58	6.08	2.71	657	2.82	1
59	7.01	3.12	682	2.83	1
60	1.16	0.51	44	1.64	1
61	2.40	1.07	150	2.18	1
62	2.72	1.21	16	1.19	0
63	20.8	9.27	2839	3.45	0
64	0.75	0.34	19	1.28	1
65	1.17	0.52	47	1.67	1
66	8.01	3.57	1106	3.04	1
67	0.62	0.28	14	1.13	1
68	1.49	0.66	65	1.81	1
69	37.2	16.6	7731	3.89	1
70	1.54	0.69	51	1.71	1
71	2.34	1.04	110	2.04	1
72	1.57	0.70	71	1.85	1
73	1.49	0.66	49	1.69	1
74	1.69	0.75	60	1.78	1
75	2.83	1.26	174	2.24	1
76	1.65	0.74	75	1.87	1
77	0.36	0.16	10	1.00	1

Table A.17: NGC 6503 - continued.

H II region	Integrated Flux (10^{-13} erg s $^{-1}$ cm $^{-2}$)	Luminosity (10^{39} erg s $^{-1}$)	EW (\AA)	log(EW) (\AA)	Flux Correction
(1)	(2)	(3)	(4)	(5)	(6)
78	1.80	0.80	78	1.89	1
79	2.94	1.31	236	2.37	1
80	3.84	1.71	312	2.49	1
81	3.86	1.72	219	2.34	0
82	1.16	0.52	62	1.79	1
83	1.38	0.61	81	1.91	1
84	4.53	2.02	483	2.68	1
85	1.27	0.57	45	1.65	1
87	2.03	0.90	117	2.07	1
88	4.13	1.84	356	2.55	1
89	2.45	1.09	106	2.03	1
90	1.14	0.51	35	1.55	1

Table A.17: NGC 6503 - continued.

H II region	Integrated Flux (10^{-13} erg s $^{-1}$ cm $^{-2}$)	Luminosity (10^{39} erg s $^{-1}$)	EW (Å)	log(EW) (Å)	Flux Correction
(1)	(2)	(3)	(4)	(5)	(6)
2	7.63	53	58	1.77	0
3	0.60	4.15	120	2.08	1
4	2.30	16	810	2.91	1
5	0.87	6.08	95	1.98	0
6	8.92	62	3034	3.48	0
7	1.36	9.45	154	2.19	0
8	2.30	16	103	2.01	0
9	1.38	9.60	37	1.56	0

Table A.18: NGC 6951 - 8 H II regions detected associated with the ring. H II region # 1 comprises the nucleus.

H II region	Integrated Flux (10^{-13} erg s $^{-1}$ cm $^{-2}$)	Luminosity (10^{39} erg s $^{-1}$)	EW (Å)	log(EW) (Å)	Flux Correction
(1)	(2)	(3)	(4)	(5)	(6)
2	1.70	5.20	88	1.94	0
3	1.06	3.25	542	2.73	1
6	0.43	1.32	118	2.07	1
8	0.65	1.99	224	2.35	1
9	0.73	2.23	306	2.49	1
10	0.50	1.54	153	2.18	1
11	1.84	5.64	987	2.99	1
12	0.79	2.43	263	2.42	1
13	0.61	1.86	216	2.33	1
14	10.3	31.5	56	1.74	0
15	0.40	1.23	105	2.02	1
16	0.26	0.80	42	1.62	1
17	0.76	2.32	262	2.42	0
18	0.21	0.64	33	1.52	1
19	0.52	1.59	143	2.16	1
20	0.64	1.95	137	2.14	0
21	0.62	1.90	189	2.28	1
22	0.23	0.71	48	1.68	1
23	1.06	3.25	478	2.68	1
24	0.77	2.37	246	2.39	1
25	0.31	0.94	63	1.80	1
26	1.19	3.64	477	2.68	1

Table A.19: NGC 7217 - 22 H II regions detected associated with the ring. H II regions # 1 and 4 comprise the nucleus; H II regions # 5 and 7 are extraneous to the ring.

H II region	Integrated Flux (10^{-13} erg s $^{-1}$ cm $^{-2}$)	Luminosity (10^{39} erg s $^{-1}$)	EW (Å)	log(EW) (Å)	Flux Correction
(1)	(2)	(3)	(4)	(5)	(6)
1	0.49	6.77	56	1.75	0
2	1.11	15.2	1054	3.02	1
3	0.24	3.27	71	1.85	1
4	0.65	8.96	65	1.81	0
5	0.91	12.4	685	2.84	1
6	0.31	4.30	86	1.94	1
9	2.21	30.2	582	2.77	0
10	3.38	46.2	234	2.37	0
11	1.30	17.8	43	1.63	0
12	0.95	13	244	2.39	0
13	0.39	5.31	49	1.69	0

Table A.20: IC 1438 - 11 H II regions detected associated with the ring. H II regions # 7 and 8 comprise the nucleus.

H II region	Integrated Flux (10^{-13} erg s $^{-1}$ cm $^{-2}$)	Luminosity (10^{39} erg s $^{-1}$)	EW (Å)	log(EW) (Å)	Flux Correction
(1)	(2)	(3)	(4)	(5)	(6)
1	0.49	12	446	2.65	0
2	0.25	6.11	234	2.37	1
3	0.35	8.46	410	2.61	1
4	0.41	10	439	2.64	1
5	0.16	3.85	93	1.97	1
6	0.77	18.9	915	2.96	1
7	0.44	10.7	343	2.54	1
8	0.48	11.7	374	2.57	1
9	1.43	35	3371	3.53	1
14	0.17	4.26	73	1.86	1
15	0.31	7.49	203	2.31	1
16	0.12	3.04	74	1.87	1
17	0.21	5.18	199	2.30	1
18	0.38	9.42	302	2.48	1
19	0.30	7.45	146	2.17	0
20	0.25	6.08	217	2.34	0
21	0.14	3.38	92	1.96	1
22	0.80	19.6	1009	3.00	1

Table A.21: NGC 7570 - 18 H II regions detected associated with the ring. H II regions # 10, 11, 12, and 13 comprise the nucleus.

H II region	Integrated Flux (10^{-13} erg s $^{-1}$ cm $^{-2}$)	Luminosity (10^{39} erg s $^{-1}$)	EW (Å)	log(EW) (Å)	Flux Correction
(1)	(2)	(3)	(4)	(5)	(6)
1	3.14	42.6	1516	3.18	0
2	1.53	20.7	684	2.84	0
3	1.38	18.8	436	2.64	0
4	0.75	10.2	1259	3.10	0
5	0.30	4.13	320	2.51	0
6	0.52	7.02	1643	3.22	1
7	0.18	2.48	304	2.48	1
8	0.31	4.24	526	2.72	0
10	0.5	6.80	1478	3.17	1
11	0.84	11.4	2556	3.41	0
12	0.40	5.40	643	2.81	0
13	0.31	4.19	694	2.84	1
14	1.20	16.4	4475	3.65	1
15	0.10	1.41	100	2.00	1
17	2.98	40.6	1840	3.26	0
18	0.95	13	2904	3.46	0
19	3.42	46.5	20204	4.31	1
20	0.63	8.57	316	2.50	0
21	0.83	11.3	102	2.01	0
22	0.64	8.71	2039	3.31	1
23	2.06	28	1135	3.06	0
24	0.20	2.76	413	2.62	1
25	0.56	7.64	1146	3.06	0
26	0.50	6.83	1523	3.18	1
29	0.29	3.93	519	2.71	1
30	0.69	9.32	1100	3.04	0
32	0.27	3.64	575	2.76	1
33	0.45	6.08	1323	3.12	1
34	3.28	44.6	23884	4.38	1
35	0.59	8.08	1756	3.24	1

Table A.22: NGC 7716 - 30 H II regions detected associated with the ring. H II region # 16 comprises the nucleus; H II regions # 9, 27, 28, and 31 are extraneous to the ring.

H II region	Integrated Flux (10^{-13} erg s $^{-1}$ cm $^{-2}$)	Luminosity (10^{39} erg s $^{-1}$)	EW (Å)	log(EW) (Å)	Flux Correction
(1)	(2)	(3)	(4)	(5)	(6)
1	1.70	10	254	2.41	0
2	6.64	39.2	352	2.55	0
3	6.59	38.9	484	2.68	0
4	3.61	21.3	524	2.72	0
5	1.08	6.37	284	2.45	1
6	1.84	10.9	496	2.70	0
7	0.88	5.19	236	2.37	1
8	12.4	73.2	2057	3.31	0
9	0.61	3.59	129	2.11	1
10	1.84	10.9	696	2.84	1
11	0.81	4.80	151	2.18	1
12	2.28	13.5	1003	3.00	1
13	0.99	5.82	347	2.54	1
14	5.07	29.9	674	2.83	0
15	1.45	8.54	507	2.70	1
16	0.70	4.15	191	2.28	1
17	0.39	2.30	55	1.74	1
19	3.09	18.2	464	2.67	0
20	1.68	9.90	575	2.76	0
21	5.59	32.9	3721	3.57	1
22	1.05	6.21	317	2.50	1
23	2.55	15	254	2.40	0
24	2.51	14.8	274	2.44	0
25	1.63	9.59	626	2.80	1
26	0.27	1.59	27	1.43	1
27	2.83	16.7	677	2.83	0
28	1.14	6.75	342	2.53	1
29	0.94	5.54	244	2.39	1
30	1.17	6.88	234	2.37	1
31	2.76	16.3	1300	3.11	1
32	0.42	2.47	84	1.92	1
33	0.58	3.45	122	2.09	1
34	2.00	11.8	811	2.91	1
35	0.54	3.19	116	2.06	1

Table A.23: NGC 7742 - 38 H II regions detected associated with the ring. H II region # 18 comprises the nucleus.

H II region	Integrated Flux (10^{-13} erg s $^{-1}$ cm $^{-2}$)	Luminosity (10^{39} erg s $^{-1}$)	EW (Å)	log(EW) (Å)	Flux Correction
(1)	(2)	(3)	(4)	(5)	(6)
36	5.52	32.6	3043	3.48	1
37	1.22	7.19	390	2.59	1
38	0.38	2.25	68	1.83	1
39	4.75	28	2633	3.42	1

Table A.23: NGC 7742 continued.

Appendix B

Discussion of Rings with No Gradient

Rings not discussed in Section 3.6 are described below. Comments are based on the plots and images seen in the Figure 3.5 panels.

B.1 NGC 613

(Figure 3.5c): There exists a small partial nuclear ring containing 11 individual star-forming H II regions with a strong nucleus. A fairly flat distribution in the $\log(\text{EW})$ appears around the entire ring with ages averaging no less than 10 Myrs. The galactic bar is located at $\text{PA} = 110^\circ$ along its major axis. Although a gradient is not defined, one of the contact points (at 200°) coincides within 5° to the youngest hotspot ($\text{PA} = 205^\circ$) in its respective hemisphere.

B.2 NGC 1300

(Figure 3.5d): Twelve H II regions form a small complete ring in $\text{H}\alpha$ although there is no clear pattern in EWs.

B.3 NGC 4303

(Figure 3.5g): Only seven H II regions define the small ring. The ring is observed to be three-quarters complete in $\text{H}\alpha$ with bipolar age maxima at $\text{PA} = 114^\circ$

and 304° . There are no obvious age gradients in between the maxima, but the latter are offset by less than 25° from the bar contact points (100° and 280°).

B.4 NGC 5248

(Figure 3.5j): Nineteen H II regions define the full, elliptically shaped ring. The youngest H II region is located 4° away from one of the bar contact points (PA = 47°).

B.5 NGC 5905

(Figure 3.5l): The ring is small but complete in H α . It consists of nine H II regions and is relatively flat with respect to age (except for one H II region). There appears to be no correlation in age with respect to the bar contact points.

B.6 NGC 5945

(Figure 3.5m): Only three H II regions define this patchy ring, which contains low EW values (all less than 1.5 in the log). Buta & Crocker (1993) indicate a nuclear ring, but our images do not have enough resolution to confirm this.

B.7 NGC 5953

(Figure 3.5n): The non-barred galaxy has a nuclear ring that appears complete with 23 H II regions. Although we know of no bar to directly fuel the ring, it is well formed and resolved both azimuthally and radially.

B.8 NGC 6503

(Figure 3.5o): The elliptically shaped ring contains 84 resolved H II regions in this unbarred spiral. No gradients are evident.

B.9 NGC 7716

(Figure 3.5t): Thirty H II regions form a complete ring in this barred galaxy. No gradients or correlations to the bar are observed.

B.10 NGC 7742

(Figure 3.5u): The circular and well resolved ring contains 38 H II regions. No gradients are observed.

BIBLIOGRAPHY

- Allard, E. L., Peletier, R. F., & Knapen, J. H. 2005, *ApJ*, 633, L25
- Allard, E. L., Knapen, J. H., Peletier, R. F., & Sarzi, M. 2006, submitted to *MNRAS*
- Arsenault, R. 1989, *A&A*, 217, 66
- Athanassoula, E. 1992, *MNRAS*, 259, 345
- Athanassoula, E. 1994, in *Mass-Transfer Induced Activity in Galaxies*, Ed. I. Shlosman, (Cambridge: Cambridge University Press), 143
- Athanassoula, E. 2002, *ASP Conf. Ser. 275: Disks of Galaxies: Kinematics, Dynamics and Perturbations*, 275, 141
- Barth, A. J., Ho, L. C., Filippenko, A. V., & Sargent, W. L. 1995, *AJ*, 110, 1009
- Benedict, G. F., Higdon, J. L., Tollestrup, E. V., Hahn, J. M., & Harvey, P. M. 1992, *AJ*, 103, 757
- Benedict, G. F., et al. 1993, *AJ*, 105, 1369
- Benedict, G. F., Howell, D. A., Jørgensen, I., Kenney, J. D. P., & Smith, B. J. 2002, *AJ*, 123, 1411
- Bertin, E., Arnouts, S. 1996, *A&A*, S117, 393
- Blackman, C. P. 1981, *MNRAS*, 195, 451
- Binney, J., & Tremaine, S. 1987, Princeton, NJ, Princeton University Press, 1987, 747
- Böker T., Calzetti D., Sparks W., et al., 1999, *ApJS*, 124, 95
- Bottama, R. 1989, *A&A*, 221, 236
- Bottama, R., & Gerritsen, J. P. E. 1997, *MNRAS*, 290, 585
- Burbidge, E. M., & Burbidge, G. R. 1960, *ApJ*, 132, 30
- Buta, R. 1986, *ApJS*, 61, 609

- Buta, R., van Driel, W., Braine, J., Combes, F., Wakamatsu, K., Sofue, Y., & Tomita, A. 1995, ApJ, 450, 593
- Buta, R., & Combes, F. 1996, Fundamentals of Cosmic Physics, 17, 95
- Buta, R., Alpert, A. J., Cobb, M. L., Crocker, D. A., & Purcell, G. B. 1998, AJ, 116, 1142
- Buta, R., & Block, D. L. 2001, ApJ, 550, 243
- Buta, R., & Crocker, D. A. 1993, AJ, 105, 1344
- Buta, R. & Crocker, D. A. 1993, AJ, 105, 1344
- Buta, R., Vasylyev, S., Salo, H., & Laurikainen, E. 2005, AJ, 130, 506
- Byrd, G., Rautiainen, P., Salo, H., Buta, R., & Crocher, D. A. 1994, AJ, 108, 476
- Chengalur, J. N., Salpeter, E. E., & Terzian, Y. 1994, AJ, 107, 1984
- Combes, F., & Gerin, M. 1985, A&A, 150, 327
- Combes, F. 2001, in: Advanced Lectures on the Starburst-AGN, Eds. I. Aretxaga, D. Kunth, & R. Mújica (Singapore: World Scientific), 223
- Combes, F., et al. 2004, A&A, 414, 857
- Contopoulos, G., & Papayannopoulos, T. 1980, A&A, 92, 33
- Davies, R. I., Tacconi, L. J., Genzel, R. 2004, ApJ, 602, 148
- Díaz-Santos, T., Alonso-Herrero, A., Coline, L., Ryder, S. D., Knapen J. H. 2006, submitted to ApJ
- de Vaucouleurs, G. 1963, ApJS, 8, 31
- de Vaucouleurs, G., & Freeman, K. C. 1972, Vistas in Astronomy, 14, 163
- de Vaucouleurs G., de Vaucouleurs A., Corwin J. R., Buta R. J., Paturel G., Fouque P., *Third Reference Catalogue of Bright Galaxies*, 1991, New York: Springer-Verlag (RC3)

- de Zeeuw, P. T., et al. 2002, MNRAS, 329, 513
- Dressel, L. L. 1988, ApJ, 329, L69
- Elmegreen, B. G. 1994, ApJ, 425, L73
- Elmegreen, B. G. 1997, Revista Mexicana de Astronomia y Astrofisica Conference Series, 6, 165
- Eskridge, P. B., et al. 2002, ApJS, 143, 73
- Evans, N. J., II, & Lada, E. A. 1991, IAU Symp. 147: Fragmentation of Molecular Clouds and Star Formation, 147, 293
- Ferrarese, L., & Ford, H. 2005, Space Science Reviews, 116, 523
- Friedli, D., & Benz, W. 1993, A&A, 268, 65
- Flores, H., Hammer, F., Elbaz, D., Cesarsky, C. J., Liang, Y. C., Fadda, D., & Gruel, N. 2004, A&A, 415, 885
- García-Burillo, S., Combes, F., Schinnerer, E., Boone, F., & Hunt, L. K. 2005, A&A, 441, 1011
- Genzel, R., Weitzel, L., Tacconi-Garman, L. E., Blietz, M., Cameron, M., Krabbe, A., Lutz, D., & Sternberg, A. 1995, ApJ, 444, 129
- Heckman, T. M., Gonzalez-Delgado, R., Leitherer, C., Meurer, G. R., Krolik, J., Wilson, A. S., Koratkar, A., & Kinney, A. 1997, ApJ, 482, 114
- Helfer, T. T., Thornley, M. D., Regan, M. W., Wong, T., Sheth, K., Vogel, S. N., Blitz, L., & Bock, D. C.-J. 2003, ApJS, 145, 259
- Heller, C. H., & Shlosman, I. 1994, ApJ, 424, 84
- Heller, C. H., & Shlosman, I. 1996, ApJ, 471, 143
- Hernández-Toledo, H. M., Fuentes-Carrera, I., Rosado, M., Cruz-González, I., Franco-Balderas, A., & Dultzin-Hacyan, D. 2003, A&A, 412, 669
- Ho, L. C., Filippenko, A. V., & Sargent, W. L. W. 1997, ApJ, 487, 579
- Hubble, E. P. *The Realm of the Nebulae*, (New Haven: Yale University Press). Exposition of Hubble Sequence, 1936

- Hummel, E., van der Hulst, J. M., & Keel, W. C. 1987, *A&A*, 172, 32
- Jogee, S., Shlosman, I., Laine, S., Englmaier, P., Knapen, J. H., Scoville, N., & Wilson, C. D. 2002, *ApJ*, 575, 156
- Jogee, S., Scoville, N., & Kenney, J. D. P. 2005, *ApJ*, 630, 837
- Kenney, J. D. P., Wilson, C. D., Scoville, N. Z., Devereux, N. A., & Young, J. S. 1992, *ApJ*, 395, L79
- Kenney, J. D. P., Carlstrom, J. E., & Young, J. S. 1993, *ApJ*, 418, 687
- Kennicutt, R. C. 1998, *ARA&A*, 36, 189
- Kennicutt, R. C., Lee, J. C., Akiyama, S., Funes, J. G., & Sakai, S. 2005, *AIP Conf. Proc. 783: The Evolution of Starbursts*, 783, 3
- Knapen, J. H., Beckman, J. E., Shlosman, I., Peletier, R. F., Heller, C. H., & de Jong, R. S. 1995a, *ApJ*, 443, L73
- Knapen, J. H., Beckman, J. E., Heller, C. H., Shlosman, I., & de Jong, R. S. 1995b, *ApJ*, 454, 623
- Knapen, J. H., Laine, S., & Relaño, M. 1999, *Ap&SS*, 269, 605
- Knapen, J. H., Shlosman, I., & Peletier, R. F. 2000, *ApJ*, 529, 93
- Knapen, J. H., deJong, R. S., Stedman, S., & Bramich, D. M. 2003, *MNRAS*, 344, 527(Erratum 2004, *MNRAS*, 346, 333)
- Knapen, J. H., Stedman, S., Bramich, D. M., Folkes, S. L., & Bradley, T. R. 2004a, *A&A*, 426, 1135
- Knapen, J. H., Whyte, L. F., de Blok, W. J. G., & van der Hulst, J. M. 2004b, *A&A*, 423, 481
- Knapen, J. H. 2004, *Astrophys. Sp. Sc. Library*, 319, 189
- Knapen, J. H. 2005a, *AIP Conf. Proc. 783: The Evolution of Starbursts*, 783, 171
- Knapen, J. H. 2005b, *A&A*, 429, 141
- Knapen, J. H., Mazzuca, L. M., Böker, T., Shlosman, I., Colina, L., Combes, F., Axon, D. J. 2006, *A&A*, 448, 489

- Kormendy, J. 1979, ApJ, 227, 714
- Kormendy, J., & Kennicutt, R. C. 2004, ARA&A, 42, 603
- Kornreich, D. A., Haynes, M. P., & Lovelace, R. V. E. 1998, AJ, 116, 2154
- Leitherer, C., et al. 1999, ApJS, 123, 3
- Martinet, L. 1995, Fundamentals of Cosmic Physics, 15, 341
- Martinet, L., & Friedli, D. 1997, A&A, 323, 363
- Mazzuca, L. M., Knapen, J. H., Veilleux, S., Regan, M. 2006a, submitted ApJ
- Mazzuca, L. M., Sarzi, M., Knapen, J. H., Veilleux, S., Swaters, R. W. 2006b, submitted ApJL
- Merrifield, M. R., & Kuijken, K. 1994, ApJ, 432, 575
- Norman, C. A., Sellwood, J. A., & Hasan, H. 1996, ApJ, 462, 114
- Moiseev, A. V., Valdés, J. R., & Chavushyan, V. H. 2004, A&A, 421, 433
- Morgan, W. W. 1958, PASP, 70, 364
- Oke, J., 1990 AJ 99,5
- Osmer, P. S., Smith, M. G., & Weedman, D. W. 1974, ApJ, 192, 279
- Osterbrock, D. E. *Astrophysics of Gaseous Nebulae and Active Galactic Nuclei*, University Science Books, 1989
- Ostriker, E. C., Stone, J. M., & Gammie, C. F. 2001, ApJ, 546, 980
- Peterson, C. J., Thonnard, N., Rubin, V. C., & Ford, W. K., Jr. 1976, ApJ, 208, 662
- Peterson, C. J., Roberts, M. S., Rubin, V. C., & Ford, W. K. 1978, ApJ, 226, 770

- Phillips, A. C., Illingworth, G. D., MacKenty, J. W., & Franx, M. 1996, *AJ*, 111, 1566
- Piner, B. G., Stone, J. M., & Teuben, P. J. 1995, *ApJ*, 449, 508
- Pogge, R. W. 1989a, *ApJ*, 345, 730
- Pogge, R. W. 1989b, *ApJS*, 71, 433
- Regan, M. W., Teuben, P. J., Vogel, S. N., & van der Hulst, T. 1996, *AJ*, 112, 2549
- Regan, M. W., Vogel, S. N., & Teuben, P. J. 1997, *ApJ*, 482, L143
- Regan, M. W., Sheth, K., & Vogel, S. N. 1999, *ApJ*, 526, 97
- Regan, M. W., & Teuben, P. 2003, *ApJ*, 582, 723
- Rix, H., & Zaritsky, D. 1995, *ApJ*, 447, 82
- Rubin, V. C., Peterson, C. J., & Ford, W. K., Jr. 1975, *ApJ*, 199, 39
- Rubin, V. C. 1980, *ApJ*, 238, 808
- Rubin, V. C., Kenney, J. D. P., & Young, J. S. 1997, *AJ*, 113, 1250
- Ryder, S. D., Knapen, J. H., & Takamiya, M. 2001, *MNRAS*, 323, 663
- Sakamoto, K., Okumura, S. K., Ishizuki, S., & Scoville, N. Z. 1999, *ApJ*, 525, 691
- Salpeter, E. E. 1955, *ApJ*, 121, 161
- Schwarz, M. P. 1981, *ApJ*, 247, 77
- Schommer, R. A., Caldwell, N., Wilson, A. S., Baldwin, J. A., Phillips, M. M., Williams, T. B., & Turtle, A. J. 1988, *ApJ*, 324, 154
- Semelin, B., & Combes, F. 2000, *A&A*, 360, 1096
- Sersic, J. L. 1958, *The Observatory*, 78, 123
- Sharp, R. G., Parry, I. R., Ryder, S. D., Knapen, J. H., & Mazzuca, L. M. 2004, *Astronomische Nachrichten*, 325, 108

- Shen, J., & Sellwood, J. A. 2004, *ApJ*, 604, 614
- Sheth, K., Regan, M. W., Vogel, S. N., & Teuben, P. J. 2000, *ApJ*, 532, 221
- Sheth, K., Vogel, S. N., Regan, M. W., Thornley, M. D., & Teuben, P. J. 2005, *ApJ*, 632, 217
- Shlosman, I., Frank, J., & Begelman, M. C. 1989, *Nature*, 338, 45
- Shlosman, I., Begelman, M. C., & Frank, J. 1990, *Nature*, 345, 679
- Shlosman, I. 2005, in: *The Evolution of Starbursts*, Eds. S. Hüttemeister & E. Manthey (Melville: AIP), 223
- Shostak, G. S., Willis, A. G., & Crane, P. C. 1981, *A&A*, 96, 393
- Simkin, S. M., Su, H. J., & Schwarz, M. P. 1980, *ApJ*, 237, 404
- Smith, D. A., Herter, T., Haynes, M. P., & Neff, S. G. 1999, *ApJ*, 510, 669
- Storchi-Bergmann, T., Wilson, A. S., & Baldwin, J. A. 1996, *ApJ*, 460, 252
- Tully, R. B. 1988, Cambridge and New York, Cambridge University Press
- van Moorsel, G. A., & Wells, D. C. 1985, *AJ*, 90, 1038
- Verdes-Montenegro, L., Bosma, A., & Athanassoula, E. 1995, *A&A*, 300, 65
- Weedman, D. W., Feldman, F. R., Balzano, V. A., Ramsey, L. W., Sramek, R. A., & Wu, C.-C. 1981, *ApJ*, 248, 105
- Zurita, A., Relaño, M., Beckman, J. E., & Knapen, J. H. 2004, *A&A*, 413, 73